Electronic Fine Structure and Recombination Dynamics in Single InAs Quantum Dots

von

Diplom-Physiker

Robert Seguin

aus Berlin

von der Fakultät II - Mathematik und Naturwissenschaften
der Technischen Universität Berlin

zur Erlangung des akademischen Grades

Doktor der Naturwissenschaften

– Dr. rer. nat. –

genehmigte Dissertation

Promotionsausschuss:

Vorsitzender: Prof. Dr. Thomas Möller
Berichter/Gutachter: Prof. Dr. Dieter Bimberg
Berichter/Gutachter: Priv. Doz. Dr. Axel Hoffmann

Tag der wissenschaftlichen Aussprache: 28.01.2008

Berlin 2008

D 83

Abstract

The electronic structure of semiconductor quantum dots (QDs) is essentially governed by quantum mechanics and differs significantly from the one of bulk semiconductors. This opens possibilities for novel applications based on single QDs like single-photon emitters for quantum cryptography or qubit registers for quantum computing. These aims can only be achieved through a profound understanding and control of the QDs' electronic properties. These properties strongly depend on the structural parameters of the QDs, such as size, composition, shape, and symmetry. In principle, this allows precise engineering of the electronic characteristics by targeted manipulation of the QDs structure.

In the work at hand single InAs/GaAs quantum dots are examined via cathodoluminescence spectroscopy. Isolation of spectra of single QDs from an ensemble is achieved either by appropriate growth of QD samples with low densities or through the application of near-field shadow masks applied on top of the sample surface.

The charge carriers confined in the QDs form excitonic complexes, such as neutral and charged excitons and biexcitons, which result in spectrally sharp emission lines upon decay. The lines of different complexes occur at varying energies due to the diverse Coulomb interaction terms between the constituting charge carriers resulting in complex single-QD spectra that frequently consist of up to ten emission lines. A thorough analysis of the spectra, however, leads to an unambiguous assignment of the lines to the decay of specific excitonic complexes.

A special aspect of the Coulomb interaction, the exchange interaction, gives rise to a fine structure in the initial and final states of an excitonic decay. This leads to a fine structure in the emission spectra that again is unique for every excitonic complex. One complex can thus show a number of emission lines with different polarization characteristics. The exchange interaction is discussed in great detail in this work. Theoretical considerations help to qualitatively understand the complicated emission spectra emerging from the fine structure. Systematic investigation of spectra of different complexes reveals similarities that originate from the same underlying physical processes thus generating a deep understanding of the exchange interaction between charge carriers in QDs.

The structural properties of the QDs have a decisive influence on their electronic structure and fine structure. Here, QDs of different sizes are investigated and the influence on the electronic properties is monitored. Additionally, the structure is modified *ex situ* by a thermal annealing process. The changes of the spectra under different annealing temperatures are traced. Thus, a possibility for targeted engineering of QDs for applications is demonstrated.

Finally, recombination dynamics of different excitonic complexes are examined by performing time-resolved cathodoluminescence spectroscopy. The fine structure of the complexes turns out to have a decisive influence on the dynamics via the number of possible decay channels for a specific complex. Together with different electron-hole wave-function overlap this leads to different decay rates of the different complexes.

In the end, this work represents an important step towards a profound understanding of the electronic structure of single InAs QDs and thus provides invaluable information for optimization of innovative single-QD-based applications such as single photon emitters, memory devices, and qubit registers.

Zusammenfassung

Die elektronische Struktur von Halbleiter-Quantenpunkten (QPen) wird wesentlich durch die Quantenmechanik bestimmt und unterscheidet sich deutlich von derjenigen von Volumenhalbleitern. Dies ermöglicht, QPe in neuartigen Bauelementen, wie Einzelphotonenemitter für die Quantenkryptographie oder Qubit-Register für Quantencomputer, zum Einsatz zu bringen. Dieses Ziel erfordert jedoch tiefgehendes Verständnis und Kontrolle ihrer elektronischen Eigenschaften. Diese Eigenschaften hängen stark von den strukturellen Parametern der QPe, wie Größe, Materialzusammensetzung, Form und Symmetrie ab. Im Prinzip ist es dadurch möglich, ihre elektronische Struktur durch gezielte Manipulation der Struktur zu bestimmen.

In der vorliegenden Arbeit werden einzelne InAs/GaAs QPe mittles Kathodolumineszenzspektroskopie untersucht. Die Isolation einzelner Spektren aus einem Ensemble von QPen erfolgt entweder durch geeignetes Wachstum von Proben mit geringer QP-Dichte oder durch das Aufbringen von Nahfeld-Schattenmasken auf die Probenoberfläche.

Die in den QPen eingeschlossenen Ladungsträger bilden exzitonische Komplexe wie neutrale und geladene Exzitonen und Biexzitonen, die bei ihrem Zerfall zu spektral scharfen Emissionslinien führen. Die Linien verschiedener Komplexe treten wegen der unterschiedlichen Coulomb-Wechselwirkungsterme zwischen den Ladungsträgern bei unterschiedlichen Energien auf. Ein Einzel-QP-Spektrum kann so aus bis zu zehn Emissionslinien bestehen. Mit Hilfe einer detaillierten Analyse der Spektren kann man jedoch jede dieser Linie zweifelsfrei dem Zerfall eines spezifischen exzitonischen Komplexes zuordnen.

Ein besonderer Aspekt der Coulomb-Wechselwirkung, die Austauschwechselwirkung, ruft eine Feinstruktur der Ausgangs- und Endzustände der exzitonischen Zerfälle hervor. Dies führt zu einer Feinstruktur der Emissionsspektren die wiederum für jeden Komplex einzigartig ist. Ein Komplex kann daher mehrere Emissionslinien mit unterschiedlichen Polarisationseigenschaften besitzen. Die Austauschwechselwirkung wird in dieser Arbeit detailliert diskutiert. Theoretische Erwägungen führen zu einem qualitativen Verständnis der durch die Feinstruktur hervorgerufenen komplizierten Spektren. Systematische Untersuchungen von Spektren verschiedener Komplexe enthüllen Gemeinsamkeiten, die von denselben physikalischen Prozessen herrühren. So wird ein detailliertes Verständnis der Austauschwechselwirkung zwischen Ladungsträgern in QPen erreicht.

Die Struktureigenschaften der QPe haben entscheidenden Einfluss auf ihre elektronische Struktur und Feinstruktur. Es werden QPe verschiedener Größen untersucht und der Einfluss auf die elektronischen Eigenschaften beobachtet. Darüber hinaus wird

die Struktur *ex situ* durch thermisches Erhitzen modifiziert. Die Veränderungen der Spektren bei verschiedenen Ausheiztemperaturen werden verfolgt. Somit wird eine Möglichkeit des gezielten Designs von QPen für Anwendungen demonstriert.

Zusätzlich wird die Rekombinationsdynamik verschiedener exzitonischer Komplexe mittels zeitaufgelöster Kathodolumineszenzspektroskopie untersucht. Es stellt sich heraus, dass die Feinstruktur der Komplexe über die Anzahl der möglichen Rekombinationskanäle entscheidenden Einfluss auf die Dynamik ihres Zerfalls hat. Zusammen mit dem unterschiedlich großen Elektron-Loch-Wellenfunktionsüberlapp führt dies zu unterschiedlichen Zerfallsraten für verschiedene Komplexe.

Diese Arbeit stellt einen wichtigen Schritt in Richtung eines tiefgreifenden Verständnisses der elektronischen Struktur einzelner InAs QPe dar. Sie liefert somit wichtige Erkenntnisse für die Optimierung innovativer einzel-QP-basierter Anwendungen wie Einzelphotonenemitter, Speicherzellen und Qubit-Register.

Parts of this work have been published in the following articles:

1. *Size-tunable exchange interaction in InAs/GaAs quantum dots*
   U. W. Pohl, A. Schliwa, R. Seguin, S. Rodt, K. Pötschke, D. Bimberg.
   in *Advances in Solid State Physics* **46** (Ed. R. Haug) (2007).

2. *Size-dependent binding energies and fine-structure splitting of excitonic complexes in single InAs/GaAs quantum dots.*
   S. Rodt, R. Seguin, A. Schliwa, F. Guffarth, K. Pötschke, U.W. Pohl, D. Bimberg.
   Proceedings of the 14th International Conference on Luminescence (July 25-29 2005, Bejing, China),
   Journal of Luminescence **122/123**, 735 (2007).

3. *Control of fine-structure splitting and excitonic binding energies in selected individual InAs/GaAs quantum dots.*
   R. Seguin, A. Schliwa, T. D. Germann, S. Rodt, M. Winkelnkemper, K. Pötschke, A. Strittmatter, U. W. Pohl, T. Hammerschmidt, P. Kratzer, D. Bimberg.
   Applied Physics Letters **89**, 263109 (2006).

4. *Ex-situ control of fine-structure splitting and excitonic binding energies in single InAs/GaAs quantum dots.*
   R. Seguin, A. Schliwa, T. D. Germann, S. Rodt, K. Pötschke, U. W. Pohl, D. Bimberg.
   Proceedings of the 28th International Conference on the Physics of Semiconductors (July 24-28 2006, Vienna, Austria);
   AIP Conference Proceedings **893**, 919 (2006).

5. *Systematic Size-dependence of anisotropic exchange interaction in InAs/GaAs quantum dots.*
   R. Seguin, A. Schliwa, S. Rodt, K. Pötschke, U. W. Pohl, D. Bimberg.
   Proceedings of the 14th International Symposium Nanostructures: Physics and Technology (June 26-30 2006, St. Petersburg, Russia), 121 (2006).

6. *Size-dependence of anisotropic exchange interaction in InAs/GaAs quantum dots.*
   R. Seguin, A. Schliwa, S. Rodt, K. Pötschke, U. W. Pohl, D. Bimberg.
   Proceedings of the 4th International Conference on Semiconductor Quantum Dots (May 1-5 2006, Chamonix-Mont Blanc, France),
   physica status solidi (b) **243**, 3937 (2006).

7. *Control of structural and excitonic properties of self-organized InAs/GaAs quantum dots.*
   U. W. Pohl, R. Seguin, S. Rodt, A. Schliwa, K. Pötschke, D. Bimberg.
   Proceedings of the 14th International Winterschool on New Developments in Solid State Physics (Feb 13-17 2006, Mauterndorf, Austria),
   Physica E **35**, 285 (2006).

8. *Quantum-dot size dependence of exciton fine-structure splitting.*
   R. Seguin, A. Schliwa, S. Rodt, K. Pötschke, U.W. Pohl, D. Bimberg.
   Proceedings of the 12th International Conference on Modulated Semiconductor Structures (July 10-15 2005, Albuquerque, USA),
   Physica E **32**, 101 (2006).

9. *Size-dependent fine-structure splitting in self-organized InAs/GaAs quantum dots.*
   R. Seguin, A. Schliwa, S. Rodt, K. Pötschke, U.W. Pohl, D. Bimberg.
   Physical Review Letters **95**, 257401 (2005).

Table of Contents

Chapter 1

Introduction

1.1 Quantum Dots: A Historical Synopsis

Few areas in physics have experienced a comparable boost in research activity like modern semiconductor physics driven by electronic, photonic and opto-electronic applications. Within this field, semiconductor quantum dots (QDs) [1, 2, 3] have been the subject of one of the most active research areas in the last decade.

This activity has originally been initiated by the understanding that nano structures enable us to modify the electronic properties of a material without changing its composition by merely designing its structure. Additionally, the first quantum structure, the quantum well (QW) where one dimension has a spatial extent below the De-Broglie-wavelength of the charge carriers, did not only show properties *different* from the bulk material. They turned out to be *superior* to bulk material for application in laser devices. In 1976 C. Henry and R. Dingle applied for a patent that replaced bulk double heterostructures in lasers with QW structures [4]. This way, the threshold current density could be drastically reduced. The patent represented the advent of nano technology in semiconductor physics.

The ultimate nano structure, the QD, possesses confinement in all three directions. It is therefore also called *artificial atom*. Continuing in the spirit of Henry and Dingle injection laser structures using QDs as active material were produced in 1994 [5] and, in 1999, the first QD-based laser with a lower threshold current density than QW lasers ($26~A/cm^2$ at room temperature) was demonstrated [6].

While photonic devices that use billions of QDs as active material such as lasers and optical amplifiers [7] have achieved a considerable level of development, new device concepts making use of a few or even single QDs such as memory cells [8], single photon emitters [9, 10, 11] or qubits[1] for quantum computers [12] have emerged. In order to

---

[1]quantum bit: a unit of quantum information

develop and optimize the structures for such applications a new field in fundamental research has appeared: single-QD spectroscopy. The experimental standards needed for single-QD spectroscopy are very high; isolating the QDs' emission from a larger ensemble requires high spatial and spectral resolution. 1994 and 1995 the first observations of sharp emission lines from QDs were reported [13, 14]. This was not single-QD spectroscopy in today's understanding since the lines from many QDs were present in the spectra. However, it proved the predicted similarity between the electronic structure of a QD and of an atom: the delta-function-like density of states. In 1996 the group of L. Samuelson presented the first isolated spectrum of a single InP/InGaP [15] leading the way to modern single-QD spectroscopy. Since then the electronic structure of QDs has been explored step-by-step. Today, the experimental setups are extremely sophisticated so that different excitonic complexes, their dynamics and even their fine structure can be investigated.

1.2   State of the Art

QDs from a variety of different material systems have been measured spectroscopically on a single-dot level: (In,Ga)As/(Al,Ga)As (e.g. [16]), InP/(Al,Ga,In)P (e.g. [15]), (Cd,Zn)Se/Zn(S)Se (e.g. [17]), and more recently (In,Ga)N/(Al,Ga)N (e.g. [18]). By far the most thoroughly investigated system is the arsenic-based one. Since the QDs provide three-dimensional confinement, charge carriers inside a QD are spatially close and couple via Coulomb interaction to form so-called excitonic complexes. A large variety of such complexes and their decay has been observed ranging from simple excitons (one electron and one hole) to excitonic molecules or biexcitons (two electrons, two holes) and their charged siblings. Due to the Coulomb energy of the different complexes their ground-state transition energy varies by a few meV from complex to complex. This leads to complicated QD spectra consisting of up to ten emission lines.

In 2000, for example, V. Türck and coworkers reported on emission from excitons and biexcitons in CdSe QDs [17]. S. Rodt and coworkers showed in 2005 that the energy of all excitonic complexes varies with QD size even if the QDs are self-similar and originate from one sample [16]. It is therefore essential to perform systematic series of measurements in order to acquire a thorough understanding of the underlying physics that governs the optical and electronic properties of QDs. In 2007 R. Warburton's group observed excitons in InGaAs QDs with charge states ranging from six extra electrons to six extra holes [19].

In 1996 D. Gammon and coworkers found a fine structure in the emission lines from GaAs/AlGaAs QDs [20]. By measuring in orthogonal polarization directions they

discovered that some of the "single" lines really consist of a polarized doublet stemming from some not further specified anisotropy of the QDs. In 1999 and in a later more comprehensive study in 2002 M. Bayer's group presented a consistent explanation along with a systematic study of this fine structure [21, 22] in InGaAs/GaAs QDs. They showed that the fine structure originates from the electron-hole exchange interaction and is only visible for certain excitonic complexes depending on their spin structure and the symmetry given by the confinement. Still, the QD parameters influencing the magnitude of the exchange splitting remained in the dark.

O. Benson and coworkers realized in 2000 that the exchange splitting of QD excitons has enormous technological relevance [23]. It is the key parameter for the generation of entangled photon pairs from QDs. They suggested a QD-based entangled-photon-pair emitter that can be used for quantum key distribution in quantum cryptography. Existing systems use attenuated laser pulses in order to produce single photons. Such systems have two major drawbacks [24]:

1. The probability of generating more than one photon per pulse is greater than zero; this follows from Poisson's statistics that gives the probability P of finding n photons in a pulse for a mean photon number $\bar{n}$:

$$P(n, \bar{n}) = \frac{e^{-\bar{n}} \bar{n}^n}{n!} \tag{1.1}$$

   For a mean of 0.1 photons per pulse, the chance of generating more than one photon in a pulse is still 0.5 %. The secrecy of the protocols explicitly demands *single* photons since multiple-photon pulses allow so-called photon-number-splitting attacks.

2. Due to the strong attenuation of the laser intensity needed to keep the probability for multi-photon pulses low, the vast majority of the pulses are empty, thus significantly reducing data transfer rates and range of the quantum cryptographical system [25].

A QD inherently represents a true single-photon source. It can only emit one photon at a time, because after the decay of an exciton the QD is empty and needs to recapture an exciton before being able to emit a new photon.

Following O. Benson's discovery the exciton fine-structure splitting has been the subject of numerous publications for example [26, 27, 28, 29] just to name a few. For a recent review of the progress of QD-based quantum light sources such as photon-pair and single photon emitters see [30].

The first reports on time-resolved spectroscopic measurements on self-assembled InGaAs/GaAs QDs were given in 1994 and carrier lifetimes of 880 ps were found

[31]. However, similar to time integrated spectroscopy, the information gained on the properties of *single* QDs was limited since a large number of QDs was probed simultaneously and thus only an *average* lifetime was measured.

1996 it was U. Bockelmann and coworkers who succeeded in measuring resonances of single GaAs/AlGaAs QDs time-resolved [32]. Despite of their rather large spectral resolution of 2 meV they were able to determine lifetimes between 170-290 ps. One step further was made in 1999 and 2000 when different lines originating from *the same* QD were measured and the corresponding lifetimes determined (see [33] for CdSe QDs, [34] for InP QDs, and [35] for InGaAs QDs). This paved the way to analyses of the dynamics of different excitonic complexes in self-assembled QDs (for (In,Ga)As QDs see [36, 37, 38, 39, 40]).

1.3   Aim of this Work

Successful application of single QDs in novel devices, such as, e.g., single photon emitters, commands a thorough understanding and control of their electronic (fine) structure. The work at hand contributes to this understanding by performing cathodoluminescence spectroscopy on single InAs/GaAs QDs in combination with theoretical considerations to explain the spectra.

An in-depth analysis of the single-QD spectra is performed to identify different excitonic complexes. The Coulomb interaction between the constituting charge carriers leads to a complicated electronic structure. One special aspect, the exchange interaction, gives rise to the exciton fine-structure splitting and is extensively discussed. Furthermore, the present concepts are expanded to comprehend the fine structure of higher excitonic complexes.

The possibility of targeted engineering of excitonic transitions and exchange energies *in situ*, by variation of growth parameters, and *ex situ*, by a thermal annealing process is presented. A large number of QDs are thus probed to develop a perception of the complex interrelation between structural end electronic properties.

The work is complemented by time-resolved measurements of the various excitonic complexes to shed light onto their decay dynamics. We attempt to establish a connection of the fine structure to the dynamic behavior and thus draw an unprecedentedly detailed picture of the QDs' electronic properties.

The work is divided into six chapters in the following way:
After the introduction in chapter 1 the second chapter explains the fundamental concepts and the theoretical background that are prerequisite to fully appreciate and understand the experimental findings. Special attention is given to the expected fine

structure of the excitonic complexes as predicted by the theory of exchange interaction.

The third chapter describes the experimental setup. After an introduction to cathodoluminescence spectroscopy, the epitaxial growth of the analyzed samples and the resulting sample structure is described. An extra section describes the challenges of single-QD spectroscopy and names several techniques to isolate spectra of single QDs.

Chapter 4 gives the experimental results and therefore constitutes the main part of this work. A detailed description on how to identify the emission of the various excitonic complexes and thus to decode the complicated spectrum of a single QD is given. Structural and electronic properties of the QDs are compared. The electronic fine structure and its impact on recombination dynamics is analyzed. Furthermore, the QD structure is manipulated via thermal annealing and the impact on the QD spectra is monitored.

The fifth chapter summarizes the experimental findings and gives a conclusion. The work is concluded by a brief outlook on possible subsequent experiments in chapter 6.

Chapter 2

Fundamental Concepts and Theoretical Background

This chapter outlines the most important theoretical concepts that are necessary to correctly interpret the experimental results. After a general introduction of the notion of quantum dots (QDs) and their structural and optical properties, special attention will be given to their electronic structure. Different aspects of Coulomb interaction between charge carriers that lead to the formation of excitonic complexes in QDs will be discussed. The central part of this chapter is an analysis of the exchange interaction that evokes an electronic fine structure of these complexes. After shortly discussing the influence of external electric fields on the energy spectra of QDs the chapter concludes with a section on recombination dynamics of charge carriers in QDs.

2.1 Zero-Dimensional Semiconductor Structures – Quantum Dots

Modern epitaxial techniques of semiconductor growth such as metal-organic chemical vapor deposition (MOCVD) or molecular beam epitaxy (MBE) allow a precision in deposition down to a single sheet of atoms, a so-called monolayer. This, in principle, leads the way to engineering of modern devices on the nano-scale. In heteroepitaxial processes, semiconductors of different band gap can be grown on top of each other in so-called heterostructures. This concept has revolutionized the semiconductor industry and ultimately led to a vast variety of modern semiconductor devices (lasers, transistors, diodes, LEDs[1], SOAs[2], . . .). In 2000 the Nobel Prize in physics was awarded to Zh. I. Alferov and H. Kroemer for the development of such heterostructures honoring

---

[1]light emitting diodes
[2]semiconductor optical amplifiers

this technological breakthrough.

A sheet of semiconductor material with a band gap E_g^1 embedded in a different semiconductor with a band gap E_g^2 with $E_g^2 > E_g^1$ represents a potential well for charge carriers with an extension that can be much smaller than their *De-Broglie* wavelength in the respective semiconductor. Then the charge carriers are not represented by *Bloch* waves that extend over the entire semiconductor crystal any more: They are spatially confined in the potential well. If the mobility of charge carriers is limited in this way, quantum mechanical effects start to govern the electronic properties of the semiconductor structure. Such quantum structures are denoted quantum wells, for one-dimensional confinement, quantum wires for two-dimensional confinement or **quantum dots**, for **three-dimensional** confinement.

2.1.1   Structural Properties

Self-organized growth of QDs is a unique phenomenon allowing the generation of three-dimensional confinement without the necessity of pre-patterning the sample. If a semiconductor is grown on top of a crystalline substrate it strives to adapt the crystal structure given by the substrate. If the lattice constants of the two crystals are not identical the system is strained in order to match the crystals on top of each other, preferably without dislocations (pseudomorphic growth). Under certain growth conditions the strain energy is reduced through the formation of nanometer-sized islands on top of the substrate. These island constitute the QDs. Details of the growth of QDs and a more detailed view on the samples examined in this work will be given in Sec. 3.2.

Modern imaging techniques such as plan-view and cross-section transmission electron microscopy (TEM) and scanning tunneling microscopy (STM) provide a good idea of the QDs' appearance (see Fig. 2.1 for sample images). The lateral size of InAs/GaAs QDs is in between a few nanometers and a few ten nanometers. Depending on the growth conditions the shape can be lens-like or pyramidal with the edges of the base area aligned along the crystal directions [100] and [010]. The QD density is typically between 10^{10} and 10^{11} per cm^2. A high density is favorable for devices that require high gain such as SOAs and lasers. Single-photon emitters, on the other hand, require a low QD density. Recently, InAs/GaAs QD densities below 10^9 cm^{-2} have been realized [9, 10, 37] even for In-rich QDs emitting near the technological important wavelength of 1300 nm [42, 43, 44].

Usually the position where the QDs form during growth cannot be prearranged or even predicted; it is absolutely random. But for devices based on single QDs the position is essential. This triggered active research with the aim to grow QDs in regular
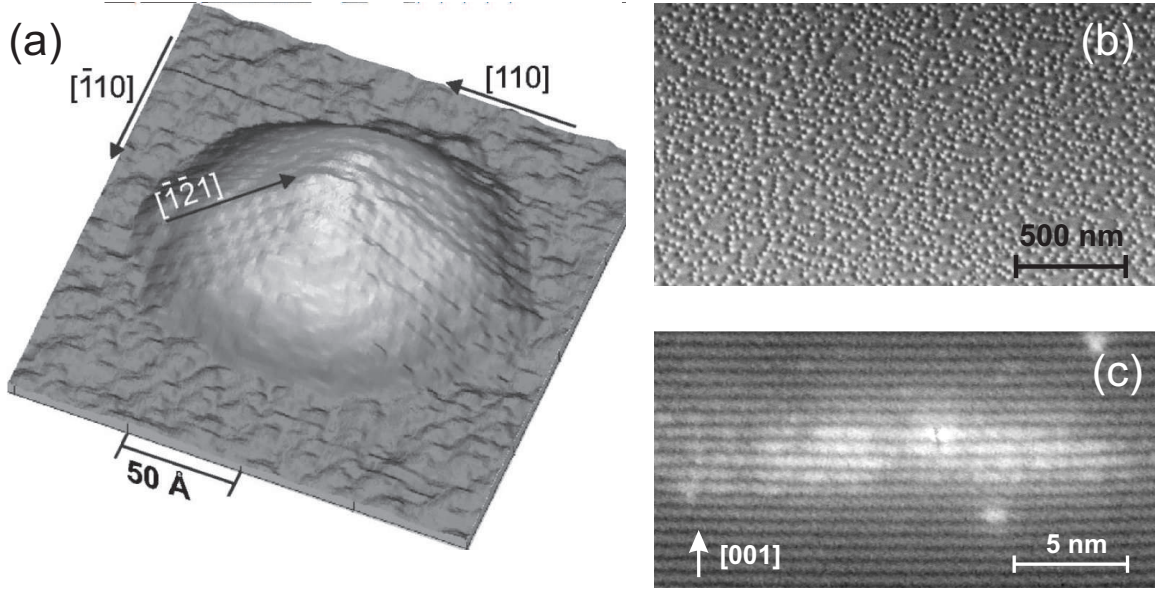
Figure 2.1: Structural images of InAs QDs: (a) Example of an STM image of an uncapped QD (from Ref. [41]). (b) Example of a plan-view TEM image of an uncapped sample with a QD density of $6.3 \cdot 10^{10}$ cm^2 (courtesy of MPI Halle). (c) Example of a cross-section STM image of an uncapped QD (courtesy of A. Lenz, AG Dähne, TU Berlin).

patterns via lithography [45, 46, 47] and other methods (e.g. atomic force patterning [48], ion beam implantation [49]).

2.1.2   Optical and Electronic Properties

The density of states (DOS) of quantum structures is significantly altered with respect to the bulk case. Figure 2.2 shows the effect on the DOS when the dimensionality of the confinement is increased successively [1].

While in all other cases the DOS stays continuous, QDs show a delta-function-like DOS. This is noteworthy because in thermal equilibrium the average occupation of the states with charge carriers is the product of the DOS and the Fermi distribution. For QDs it is therefore not affected by temperature despite the smearing out of the Fermi distribution. In principal, this makes QD-based devices very temperature stable. Indeed, QD-based lasers with a characteristic temperature T_0 of 150 K up to an operating temperature of 45 °C have been demonstrated [50]. Another consequence is, that when electrons and holes in a QD recombine, discrete transition energies are expected, much like in an atom. Hence, QDs are sometimes denoted "artificial atoms" in the dielectric cage of the surrounding semiconductor matrix.

Figure 2.3 shows a simplified band diagram of a QD in one dimension neglecting strain and wetting layer states. The band discontinuity between the two semiconductor
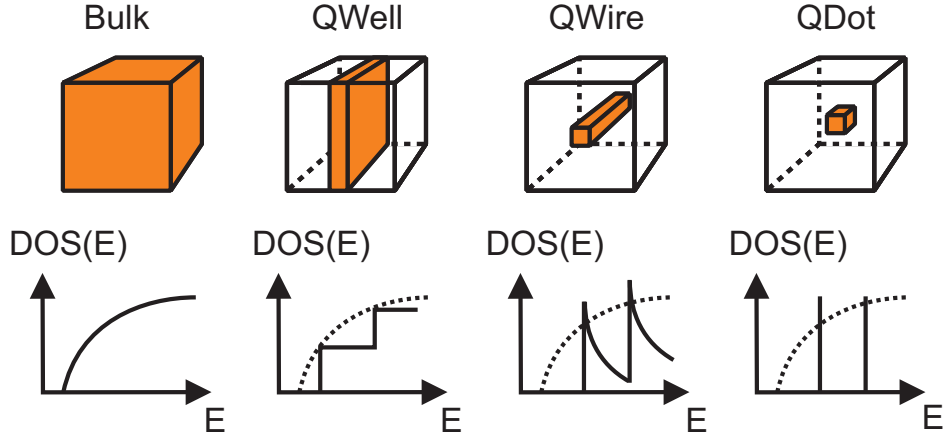
Figure 2.2: Density of states (DOS) for bulk semiconductors, quantum wells, quantum wires, and quantum dots. For quantum dots the DOS is discrete while all other structures have a continuous DOS.

materials leads to attractive potential wells for electrons in the conduction band and holes in the valence band. Such a configuration is called type-I QD. Type-II QDs, by contrast, form an attractive potential only for one charge carrier type and a repulsive potential for the other. Type-III QDs are similar to type II with the additional condition, that the conduction and valence band discontinuity is larger than the actual band
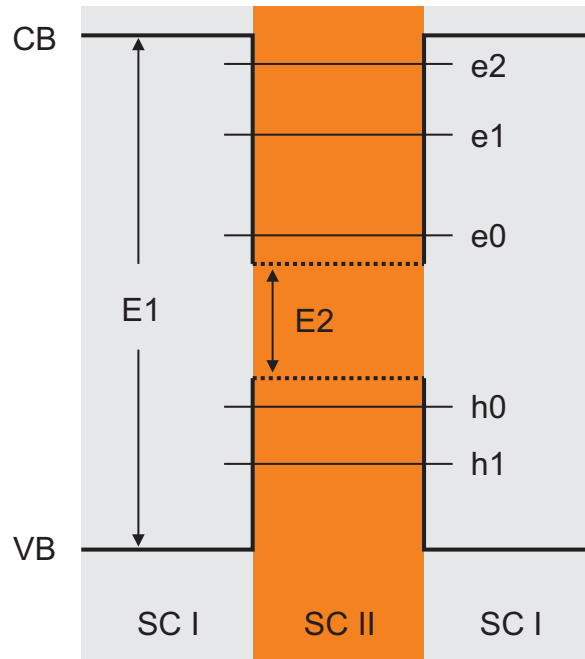

Figure 2.3: One-dimensional scheme of the band diagram of a quantum dot. CB: conduction band; VB: valence band; E1: band gap of semiconductor 1 (SC1); E2: band gap of semiconductor 2 (SC2); e0/h0: electron/hole ground state; e1,e2/h1: electron/hole excited states.

gap of the matrix material. The type of QDs formed solely depends on the band gap and band offset of the two semiconductors[3] and is therefore a function of the materials used. The material combination examined in this work [In(Ga)As/GaAs] always results in type-I structures similar to Fig. 2.3.

Just like electrons in atoms, electrons in QDs have ground states and excited states. The electronic structure, however, differs significantly. The energetic distance between ground and excited states is not only a function of the respective (effective) masses but is strongly governed by the specific form of the confinement potential and therefore QD morphology.

From Fig. 2.3 it is evident, that the QD ground state transition $e_0 \rightarrow h_0$ is larger in energy than the band gap of the QD material. The difference between the two is called quantization energy and strongly depends on the size of the QD and the effective masses of the charge carriers. The difference between delocalized states of electrons and holes in the surroundings of the QD (the surrounding matrix or the wetting layer) and e0 (h0) is called electron (hole) ground-state localization energy.

As indicated before, the electronic structure of QDs is strongly governed by their structural properties. In detail, these are:

QD size: The smaller the size of the QD, the larger the confinement energy. Consequently, the transition energy between electron and hole ground states is largest for small QDs. This effect is called *quantum size effect* [1]. Depending on the effective masses, very small QDs may have no bound state at all when the ground state is "pushed" into the wetting layer or bulk continuum.

Composition: The material of the QD can be composed of elemental or binary, ternary or even quaternary compound semiconductors. The exact composition determines the band gap energy of the QD material and therefore the transition energy. As a secondary effect, the confinement energy is altered when the band gap is modified and therefore the height of the potential well changes.

Shape: Different shapes of the QDs, such as lens-shaped, pyramidal, truncated pyramidal, different aspect ratios etc. lead to different mutual positions and overlap of the electron and hole wave functions, directly influencing the Coulomb energy between them and thus the emission spectrum (see Sec. 2.2).

Strain: The different lattice constants of matrix and QD material lead to complicated strain fields inside and outside the QDs. In zinc-blende crystals *hydrostatic strain* strongly influences the energy of both valence and conduction band and therefore

---

[3]A secondary effect determining the type of QDs is the strain in the system since it influences both, band gap and band offset.

the band gap. *Biaxial strain* additionally lifts the degeneracy of the highest valence bands (heavy-hole and light-hole) at the Γ-point and *shear strain* leads to piezoelectric fields [51] and thus a reduction of symmetry.

Symmetry: The degree of degeneracy of the electronic states depends on the symmetry of the confining potential. In general, lower symmetry can lead to a splitting of previously degenerate states, thus influencing the transition energy and polarization characteristics and number of transition lines. This aspect will be a pivot point in this work and be addressed in detail in Sec. 2.2.2 and Chap. 4.

The complex relation between these structural parameters of the QDs and their optical properties features the possibility of targeted tailoring of QDs for specific applications. The spectra of two QDs that differ in one or more of these parameters will generally be different. Moreover, no two QDs even in one sample will be exactly alike. In conventional photoluminescence, a large number of structurally different QDs will thus be probed simultaneously. A typical QD density is on the order of 10^{10} QDs per cm^2. If the exciting laser beam is focused to 0.5 mm^2, light from no less than 50 million QDs is detected at the same time. Since all these QDs differ slightly in their
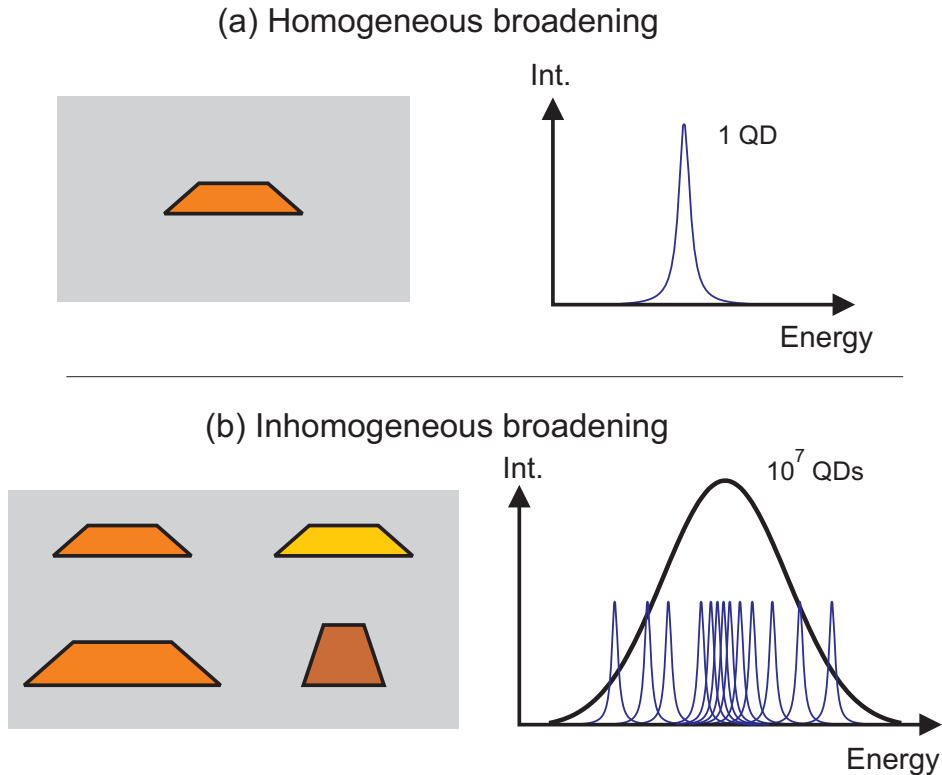

Figure 2.4: Broadening mechanisms. (a) The line of a single QD is homogeneously broadened due to the finite phase relaxation time (see Sec. 2.4). (b) Lines of simultaneously detected QDs superimpose to give the inhomogeneously broadened ensemble peak.

geometry, their spectra superimpose to give a broad ensemble peak. This mechanism is called inhomogeneous broadening (compare to homogeneous broadening, Sec. 2.4) and is explained schematically in Fig. 2.4.

The inhomogeneous broadening mechanism obscures the spectra of individual QDs. It takes great effort to isolate single-QD spectra (see Sec. 3.3) in order to analyze their electronic structure which is the main aim of this work.

2.2   Few-Particle States in Quantum Dots – Coulomb Interaction

The fundamental excitation in a semiconductor is represented in the single-particle picture by lifting one electron from the filled valence band into the empty conduction band. Instead of regarding the electron valence band with one electron missing it is much simpler to treat it as a hole band filled with one hole. The holes form new quasiparticles with charge and spin opposite to the ones of the removed electron. The N-particle system of N electrons in their first excited state is now considered as a two-particle system consisting of the conduction band electron and the valence band hole. It is described by the Hamiltonian

$$\mathcal{H} = \mathcal{H}_e + \mathcal{H}_h,$$ (2.1)

where $\mathcal{H}_{e/h}$ are the single-particle Hamiltonians of electron and hole.

However, due to the electron-electron interaction or, to stay in the hole picture, electron-hole interaction electrons and holes cannot be described independently. They form a new quasiparticle: the *exciton*. Its energy is determined by the Hamiltonian

$$\mathcal{H}_{\mathrm{X}} = \mathcal{H}_e + \mathcal{H}_h + \mathcal{H}_{coul}.$$ (2.2)

In bulk semiconductors, the attractive Coulomb interaction between electron and hole leads to a lowering of the total energy of an exciton with respect to the total energy of a free electron plus a free hole: the *exciton binding energy*. It is given in the effective mass or parabolic approximation by (see e.g. [52])

$$E_{\mathrm{X}}(n, \mathbf{K}) = E_g - R_y \frac{\mu}{\epsilon^2} \frac{1}{n^2} + \frac{\hbar \mathbf{K}^2}{2M}$$ (2.3)

with

$$n \quad - \quad \text{principal quantum number}$$
$$\mathbf{K} \quad - \quad \text{exciton wave vector} = \mathbf{k}_e + \mathbf{k}_h$$

$$
\begin{aligned}
E_g \quad &- \quad \text{band gap} \\
R_y \quad &= \quad 13.6\text{eV} - \text{Rydberg constant} \\
\mu \quad &- \quad \text{reduced mass with } \frac{1}{\mu} = \frac{1}{m_{\text{eff}}^e} + \frac{1}{m_{\text{eff}}^h} \\
\epsilon \quad &- \quad \text{static dielectric constant} \\
\hbar \quad &= \quad 6.582 \cdot 10^{-16}\text{eV} \cdot \text{s} - \text{Planck's constant} \\
M \quad &- \quad \text{exciton translational mass} = m_{\text{eff}}^e + m_{\text{eff}}^h
\end{aligned}
$$

The effective masses m_{eff}^i are determined by the curvature of the respective energy band and are given by

$$
m_{\text{eff}}^i = \hbar^2 \left(\frac{\partial^2 E_i}{\partial k^2} \right)^{-1}. \tag{2.4}
$$

The different energy levels of the exciton form a Rydberg series similar to the hydrogen atom with an *effective* Rydberg constant modified by the reduced mass of the exciton and the dielectric constant of the material. Note that this description is valid only for weakly bound (or Wannier) excitons where the exciton Bohr radius, given by

$$
a_B^X = a_B^H \frac{\epsilon}{\mu}, \tag{2.5}
$$

with $a_B^H = 5.29\ 10^{-11}$m $\quad - \quad$ hydrogen Bohr radius

is larger than the nearest-neighbor unit cells and hence the Coulomb interaction is strongly screened by the valence and core electrons. Wannier excitons can be found in most semiconductors (e.g. a_B^X(GaAs) $\approx$ 12 nm[4], lattice constant = 0.6 nm). Strongly bound (or Frenkel) excitons exist in very ionic compounds and do not play a role in this work.

In absorption experiments at low temperatures the energy lowering of the exciton with respect to the band edge is visualized by a series of sharp resonances just below the band gap of the semiconductor.

In QDs the analog to the bulk exciton exists. Here, the exciton binding energy is not accessible by optical spectroscopy since, in contrast to bulk material, no "free" electron-hole-pairs exist due to the QD confinement. The Coulomb interaction is enhanced with respect to the bulk case due to the close proximity and compression of electron and hole wave functions. Indeed, calculations for InAs/GaAs QDs predict an exciton binding energy between 11 and 26 meV [54], thus surpassing the GaAs bulk exciton binding energy of 4.9 meV by a factor of two to five. Nevertheless, in InAs/GaAs QDs the localization energy still surpasses the exciton binding energy by an order of magnitude.

---

[4]with ϵ(GaAs)=12.5, m_{eff}^e(GaAs)=0.065 m_0, and m_{eff}^{hh}(GaAs)=0.48 m_0 [53].

This defines the strong confinement regime where the few-particle characteristics are predominantly governed by the confinement potential.

An interesting consequence of the confinement is the possibility that "anti-binding" complexes, i.e. complexes with a negative binding energy, exist (see following section). In bulk material such complexes would immediately dissociate into their components.

2.2.1   Excitonic Complexes

Apart from the exciton (X) which is composed of one electron-hole pair, a QD can also be occupied by higher excitonic complexes consisting of a number of electrons and holes. Charged excitons, also called trions (X^+, X^-), or biexcitons (XX) can be formed consisting of three and four single charge carriers, respectively. It is possible that one electron-hole pair from one of these complexes recombines, leaving the QD occupied by a new excitonic complex. This is similar to radioactive cascades of atoms. A biexciton, for example, can decay by conversion of one electron-hole pair into a photon and leaving behind the other electron-hole pair forming a single exciton. The biexcitonic resonance in the spectrum of a single QD will be observed at an energy that differs from the exciton energy by the *biexciton binding energy*. This is due to the additional Coulomb interaction between all charge carriers of the biexciton. As mentioned before, no free electrons and holes exist in a QD due their close proximity. Therefore, the binding energy of an excitonic complex in a QD is defined relative to the exciton.

The following discussion is initially limited to the strongest and most important part of the Coulomb interaction called *direct* or *mean-field* Coulomb interaction. Correlation and exchange will be discussed further below.

Let C_{ij} be the Coulomb interaction between two charge carriers i and j (with $i, j = e$ for electrons and h for holes) given by

$$C_{ij} = \int \int \frac{q_i q_j}{4\pi\epsilon_r\epsilon_0} \frac{|\Psi_i(\mathbf{r}_1)|^2 |\Psi_j(\mathbf{r}_2)|^2}{|\mathbf{r}_1 - \mathbf{r}_2|} d\mathbf{r}_1 d\mathbf{r}_2. \tag{2.6}$$
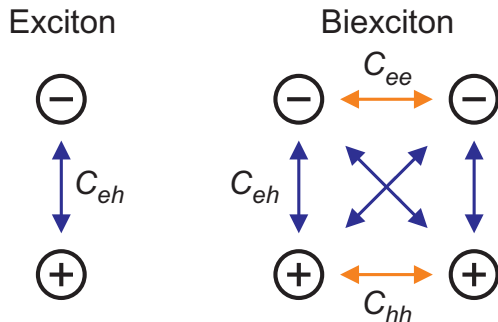

Figure 2.5: Coulomb interaction scheme for an exciton (left) and a biexciton (right). C_{ij} denote the Coulomb interaction between electrons (e) and holes (h). Blue (orange) arrows indicate attractive (repulsive) interaction.

material	$m_{\text{eff}}^e [m_0]$	$m_{\text{eff}}^{hh} [m_0]$	$m_{\text{eff}}^{lh} [m_0]$
GaAs	0.065	0.48	0.087
InAs	0.023	0.41	0.025

Table 2.1: Effective masses for electrons (m_{eff}^e), heavy holes (m_{eff}^{hh}), and light holes (m_{eff}^{lh}) for InAs and GaAs (taken from Ref. [53]).

In the single particle picture the exciton energy is then given by

$$E(\text{X}) = E(e) + E(h) + C_{eh}. \tag{2.7}$$

The biexciton energy is given by

$$E(\text{XX}) = 2E(e) + 2E(h) + C_{ee} + 4C_{eh} + C_{hh}. \tag{2.8}$$

This situation is visualized in Fig. 2.5. The biexciton binding energy can be conceived as the energy that can be gained when two excitons form a biexciton. Here it is defined to be positive when E(XX)< 2 E(X). Consequently,

$$E_{bind}^{\text{XX}} = 2E(\text{X}) - E(\text{XX}) = -C_{ee} - 2C_{eh} - C_{hh}. \tag{2.9}$$

Analogously, the binding energies of the trions are given by

$$E_{bind}^{\text{X}^+} = [E(\text{X}) + E(h)] - E(\text{X}^+) = -C_{hh} - C_{eh} \tag{2.10}$$

$$E_{bind}^{\text{X}^-} = [E(\text{X}) + E(e)] - E(\text{X}^-) = -C_{ee} - C_{eh}. \tag{2.11}$$

Note, that C_{ee} and C_{hh} denote repulsive interaction, i.e. C_{ee}, $C_{hh} > 0$, and C_{eh} attractive interaction, i.e. $C_{eh} < 0$. The question of whether the binding energy is positive or negative, i.e. whether the complex is *binding* or *anti-binding*, is therefore a question of the magnitude of the attractive and repulsive Coulomb interaction terms.

For InAs/GaAs QDs a general rule for the energetic position of X, X^+, X^-, and XX can be deduced. Since the effective electron mass in these systems is much smaller than the effective hole masses (see Tab. 2.1), the hole wave functions are stronger confined to the QDs than the electron wave functions, i.e. the spatial extent of holes is smaller than that of electrons. Together with Eq. 2.6 this implies that

$$C_{ee} < C_{hh} \tag{2.12}$$

and, provided that electron and hole centers of mass are not too far away from each other[5],

$$C_{ee} < |C_{eh}| < C_{hh}. \tag{2.13}$$

---

[5]Realistically, electron and hole centers of mass are not identical. In InAs QDs, however, they are usually close enough that Eq. 2.13 holds. In Nitride-based QDs, e.g. InGaN/GaN or GaN/AlN, large electric fields are present [55] that strongly separate electrons and holes. Then, the energetic ordering of the excitonic complexes differs strongly from Fig. 2.6 [56].
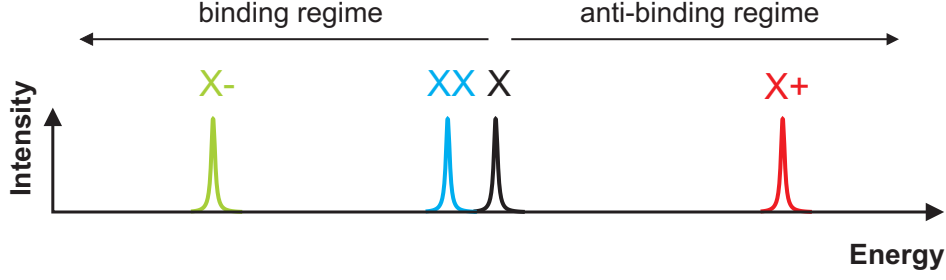
Figure 2.6: Relative energetic position of excitonic complexes of a QD satisfying Eq. 2.14. A binding biexciton (i.e. $E_{bind}^{\mathrm{XX}} > 0$) is shown as an example. Equation (2.14) would principally also allow an antibinding biexciton (i.e. $E_{bind}^{\mathrm{XX}} < 0$).

Equations 2.9 - 2.11 and 2.13 lead to

$$0 < E_{bind}^{\mathrm{X}^-} > E_{bind}^{\mathrm{XX}} > E_{bind}^{\mathrm{X}^+} < 0. \qquad (2.14)$$

The question whether the biexciton is binding or anti-binding can not be answered by this simple picture and needs to be analyzed in further detail (see below). A model spectrum satisfying Eq. 2.14 is given in Fig. 2.6.

Although this picture is helpful when discussing the spectral position of the excitonic complexes qualitatively, it is insufficient for a quantitative analysis. We have disregarded, for example, that the presence of additional charge carriers alters their wave functions, thus influencing the original Coulomb interaction terms, and quantum mechanical effects such as correlation and exchange.

More realistic models are needed in order to quantitatively compare them to the experiment and thus gain further insight into the physical processes occurring in QDs by exploiting the symbiosis between theory and experiment: On the one hand the experiment helps to increase the accuracy of the models and unveils parts where the model does not accurately describe reality. In this way, new relations between a physical source and an observed effect can be established. An accurate theory, on the other hand, is able to make predictions and thus guide the experiment to the discovery of new effects or optimize device performance via adapted growth conditions.

Eight-band $\mathbf{k}\cdot\mathbf{p}$ theory in conjunction with the configuration interaction method [54, 57, 58, 59] has proven to be a powerful tool to analyze the optical spectra of single QDs. Single particle wave functions are determined with eight-band $\mathbf{k}\cdot\mathbf{p}$ theory taking into account size, shape, and composition of the QD, strain fields, band mixing, and first- [51] and second-order [60, 61] piezoelectricity. Then, in order to determine the few-particle states, the few-particle Hamiltonian is expanded into a basis consisting of anti-symmetrized products[6] of the single-particle wave functions including both,

---

[6]to account for the fact that electrons and holes are fermions

ground and excited states using the configuration interaction method. The ground state of the many-particle wave functions is then composed not only of the single-particle ground states but also has non-zero components in the single-particle excited states. This effect is called correlation.[7] It is important to have a large basis of single-particle states in order to limit the error made by working with an incomplete basis.

Correlation is important when the binding energies of excitonic complexes in QDs are to be modeled quantitatively. For example, correlation effects are stronger for the biexciton than for the exciton since the few-particle wave functions will differ more significantly from the single-particle wave functions due to the higher number of charge carriers involved. That means that the biexciton total energy is reduced with respect to the exciton energy. Consequently, correlation leads to an increase of the biexciton binding energy. For a more elaborate discussion of correlation see Ref. [58].

2.2.2 Exchange Interaction

So far we have neglected that electrons and holes are fermions, i.e. they have half-integer spin and therefore obey the Pauli principle. This fact gives rise to an additional part of the Coulomb interaction called exchange interaction. It will be discussed in some detail in this section as it is decisive for this work.

In the case of two identical particles an exchange of coordinates leads to an identical situation. This means that if for two particles a and b $\Psi_{12} = \psi_a^1 \otimes \psi_b^2$ is an eigenfunction of $\mathcal{H}$, so is $\Psi_{21} = \psi_a^2 \otimes \psi_b^1$ with $|\Psi_{12}|^2 = |\Psi_{21}|^2$ and both solutions having the same eigenvalue. One speaks of *exchange degeneracy*. This can be realized through $\Psi_{12} = \Psi_{21}$ (Bosons) or $\Psi_{12} = -\Psi_{21}$ (Fermions). Consequently, if we take the fermionic character of the participating particles into account the solutions have to be antisymmetric. In this antisymmetric basis the interaction term $\mathcal{H}_{coul}$ (Eq. 2.2) contains terms of the form

$$< \psi_a^1 \psi_b^2 | \mathcal{H}_{coul} | \psi_a^2 \psi_b^1 > . \tag{2.15}$$

These terms are well-known from quantum mechanics and atomic physics and are called *exchange terms* or *exchange integrals*. Since this exchange interaction arises

---

[7]The term "correlation" is a bit misleading. It does account for the quantum mechanical Coulomb correlation that describes the gain in energy if electrons and holes in a plasma arrange in a way to minimize Coulomb interaction between each other rather than be distributed evenly, i.e. their spatial coordinates are correlated. However, it also includes self-consistency of the wave functions in the Hartree sense, that accounts for their deformation due to the presence of other charge carriers in their vicinity. This effect is fundamentally different from quantum mechanical correlation. In this work the term correlation always signifies the deviation of the wave function shape from the single-particle wave functions thus including self-consistency *and* quantum mechanical correlation.

when including spin (via the precondition of anti-symmetrized basis functions) it can be considered as a spin-spin interaction between the participating particles.

The ground state of the exciton can have different spin configurations of the participating electron and hole. For zinc-blende materials such as GaAs or InAs the exciton is eight-fold degenerate at the Γ point, i.e. $K = 0$. This results from the two possible spin configurations $|s, s_z\rangle = |\frac{1}{2}, \pm\frac{1}{2}\rangle$ of the electron and four possible configurations of the hole $|j, j_z\rangle = |\frac{3}{2}, \pm\frac{3}{2}\rangle$ [heavy holes (hh)] and $|\frac{3}{2}, \pm\frac{1}{2}\rangle$ [light holes (lh)]. The split-off holes with states $|\frac{1}{2}, \pm\frac{1}{2}\rangle$ are at a different energy due to the spin-orbit coupling.

In QDs the degeneracy is lower. The biaxial strain present in QD structures leads to a lifting of the valence band degeneracy even at the Γ-point. In InAs/GaAs QDs the energetic difference between the uppermost hh-band and the lh-band can approach 200 meV [58]. This means that QD excitons are predominantly hh-like with the according effective mass and spin (see Sec. 2.2.3). Unless stated otherwise, "hole" will henceforth always mean "heavy hole". The resulting four-fold degeneracy of the exciton ground state can be split by the exchange interaction (see Sec. 2.2.3).

The magnitude of the exchange interaction depends on a number of different parameters that are hard to access or, in fact, partly unknown. It is hence difficult to be evaluated quantitatively[8]. Symmetry considerations from group theory, however, result in qualitative results, that help to interpret and understand the luminescence spectra. The effective exchange Hamiltonian for C_{2v} symmetry reads [62]

$$\mathcal{H}^{ex} = \underbrace{2\Delta_0 J_z S_z}_{\mathcal{H}_0^{ex}} + \underbrace{\Delta_1(J_x S_x - J_y S_y)}_{\mathcal{H}_1^{ex}} + \underbrace{\Delta_2(J_x S_x + J_y S_y)}_{\mathcal{H}_2^{ex}}, \qquad (2.16)$$

where $\mathbf{S} = (S_x, S_y, S_z)$ and $\mathbf{J} = (J_x, J_y, J_z)$ are the total spin operators for the participating electrons and holes[9] and the Δ_i are constants. We will use capital letters for spin operators consisting of more than one particle. For the exciton $\mathbf{S}$ and $\mathbf{J}$ are the single particle spin operators $\mathbf{s}$ of the electron and $\mathbf{j}$ of the hole. For more complex particles, however, $\mathbf{S}$ and $\mathbf{J}$ can consist of more than one single particle spin operator.

While this Hamiltonian qualitatively describes the splitting of foremost degenerate energy states due to exchange interaction, a quantitative prediction is not possible, since the Δ_i are simply parameters without physical meaning.

---

[8]When calculating the exchange interaction quantitatively it is commonly separated into two parts: *short-range* interaction, i.e. the contribution of the exchange integral *inside* the Wigner-Seitz cell and *long-range* interaction, i.e. the contribution of the exchange integral *outside* the Wigner-Seitz cell. This separation, however, has merely technical reasons and will therefore be neglected in the following qualitative analysis since there is no way to distinguish between the two in the experiment.

[9]$\mathbf{J}$ actually denotes the hole pseudospin, a mathematical concept introduced to simplify the notation (see App. A).

2.2.3   Exciton Fine Structure

The hh-exciton ground state in QDs is fourfold (spin-)degenerate since both, electron and (heavy) hole, have two different possible spin configurations (spin up or spin down). The exchange Hamiltonian (Eq. 2.16) for the exciton in the basis $|F_z\rangle$ where F_z is the projection of the total exciton spin $\mathbf{F} = \mathbf{s} + \mathbf{j}$ reads

$$
\mathcal{H}^{ex} = \frac{1}{2}
\begin{pmatrix}
\Delta_0 & \Delta_1 & 0 & 0 \\
\Delta_1 & \Delta_0 & 0 & 0 \\
0 & 0 & -\Delta_0 & \Delta_2 \\
0 & 0 & \Delta_2 & -\Delta_0
\end{pmatrix}
\tag{2.17}
$$

where the rows and columns correspond to $|-1\rangle$, $|+1\rangle$, $|-2\rangle$, and $|+2\rangle$. The derivation of this more convenient matrix form of $\mathcal{H}^{ex}$ from (2.16) is carried out in detail in App. A.

This Hamiltonian lifts the fourfold degeneracy of the exciton ground state. It is split by $\mathcal{H}_0^{ex}$ of Eq. 2.16 or the diagonal terms in Eq. 2.17 into two doublets: the so-called *bright* doublet consisting of the states $|\pm 1\rangle$ and the *dark* doublet consisting of $|\pm 2\rangle$. The denotation is owed to the fact that the bright states couple to the photonic field (i.e. can decay or be created via the emission or absorption of a photon with spin ± 1), while the dark states do not[10]. $\mathcal{H}_1^{ex}$ ($\mathcal{H}_2^{ex}$) leads to a mixing of the bright (dark) states, leading to a complete removal of any degeneracy and leaving the two bright (dark) states $|-1\rangle \pm |1\rangle$ ($|-2\rangle \pm |2\rangle$)[11]. H_1^{ex} is called the anisotropic exchange term because Δ_1 is non-zero only if the confining potential shows some anisotropy in the growth plane (C_{2v} symmetry or lower). The complete exciton energy scheme for the QD ground state exciton is depicted in Fig. 2.7.

Since the radiative decay of the dark excitons (i.e. excitons occupying the dark states) is forbidden due to the spin selection rule, only Δ_1 is experimentally accessible in optical spectroscopy. When a magnetic field $\mathbf{B}$ is applied, however, dark and bright states intermix, forming excitons whose decay into a photon is partially allowed. Interpolation to $\mathbf{B}=0$ then yields Δ_0 and Δ_2 [22]. In this work, no magnetic field will be applied; hence we will concentrate on the bright excitons.

In the single-QD spectra the manifestation of Δ_1, also called (bright) exciton fine-structure splitting (FSS) is twofold:

On the one hand the exciton can occupy one of the two bright states and decay

---

[10]The binding energies discussed in Sec. 2.2.1 and measured in Sec. 4.2.1 are always given with respect to the center of the two exciton bright states and are thus systematically overestimated by $\Delta_0/2$.

[11]The normalization factor will be omitted throughout this work for simplicity. To be exact, the bright and dark states should read $\frac{1}{\sqrt{2}} (|-1\rangle \pm |1\rangle)$ and $\frac{1}{\sqrt{2}} (|-2\rangle \pm |2\rangle)$, respectively.
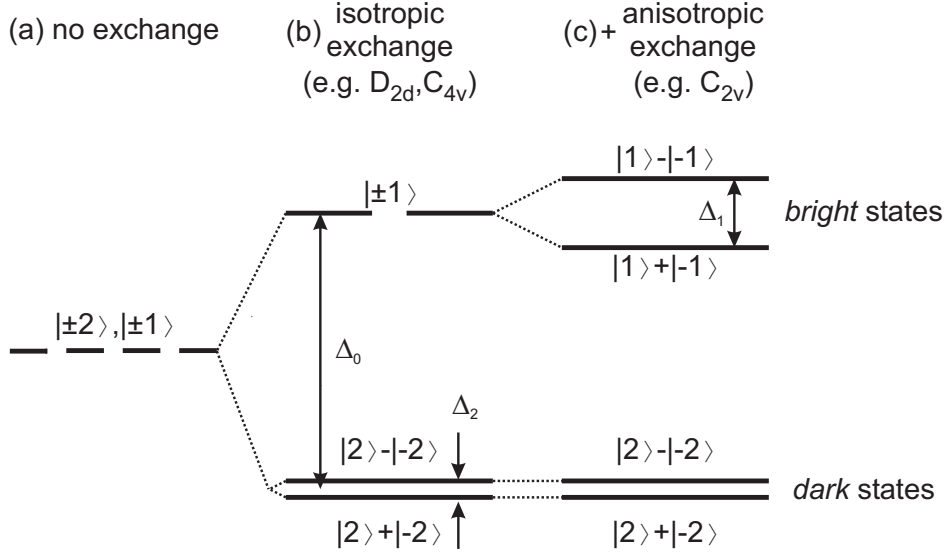
Figure 2.7: Energy scheme for the lowest energy heavy hole exciton states in QDs: (a) without exchange interaction, (b) with exchange interaction for, e.g., D_{2d} or C_{4v} symmetry, (c) with exchange interaction for, e.g., C_{2v} symmetry. The number of dashes gives the degree of degeneracy. The numbers denote the exciton spin projection $|F_z\rangle$. The Δ_i correspond to the constants in Eqs. 2.16 and 2.17.

into a photon leaving behind an empty QD. The corresponding transition lines in the spectrum are energetically separated by the FSS. Moreover, since the bright states are a superposition of the states $|-1\rangle$ and $|1\rangle$, the light emitted from a decay of these states is a superposition of circularly polarized photons, i.e. it is linearly polarized. The polarization directions are parallel and perpendicular to the anisotropy axes of the confining potential.

On the other hand the biexciton also has two different decay paths. The biexciton ground state is fully degenerate. In fact, since both, the two electrons and the two holes, occupy closed shells the Pauli principle commands that there is only one possible state: $|F_z\rangle = |0\rangle$. However, the final state of the transition leads to different resonances in the spectrum. The biexciton can decay into either of the two exciton bright states. Consequently, analogously to the exciton, the biexciton will also display two linearly polarized lines in the spectrum, separated in energy by the FSS (Fig. 2.8).

As mentioned before, the FSS is a measure of the anisotropy of the confining potential. This leads to the question of the physical sources of this anisotropy. Three sources have been discussed in the literature: (a) a structural elongation of the QD, (b) piezoelectricity resulting from shear strain [51, 54], and (c) atomistic symmetry anisotropy [63, 64] taking into account atomistic differences in the QDs' interfaces. A discussion of these possible origins of anisotropy will be given in Chap. 4.

The FSS has attracted a lot of attention in the literature in recent years (for
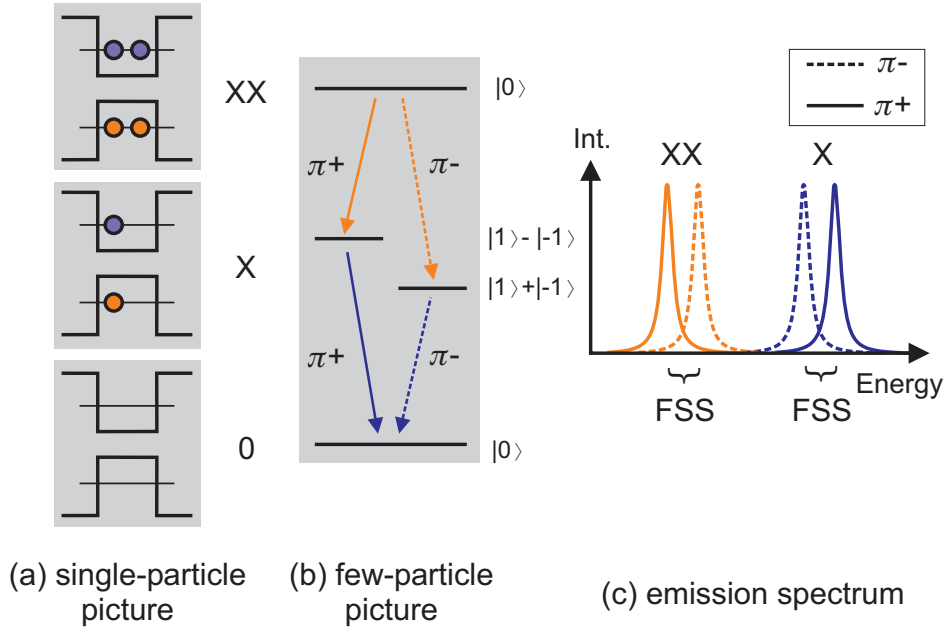
Figure 2.8: Transition scheme for the XX → X → 0 cascade and manifestation of the exchange interaction in the emission spectrum. An exciton and a biexciton doublet consisting of cross-polarized lines should appear in the spectrum, separated by the FSS respectively. $\pi+$ and $\pi-$ correspond to linearly (and orthogonally) polarized light.

example [22, 26, 27, 28, 29, 63, 65, 66]) due to its technological relevance [10, 23]. Modern quantum key distribution protocols (e.g. the BB84 protocol [67]) for quantum cryptography are based on encoding data into qubits represented by single polarized photons [68].

Apart from the technological challenges to produce QD-based single-photon emitters it is essential to control the polarization of the emitted photons in order to obtain well-defined qubits. The XX→X→0 cascade provides such control via the FSS. A large FSS yields polarized photons with well defined polarization directions together with the possibility to energetically filter the two directions. An FSS below the homogeneous line width of the X and XX transitions on the other hand was predicted to yield polarization entangled photon pairs [23, 36] that can also be used for quantum key distribution. Indeed, in 2006 the groups of D. Gershoni and A. J. Shields provided independently from one another the corresponding experimental proof [69, 70]. It is therefore of largest importance to understand and control the FSS.

2.2.4 Kramers' Theorem

The addition of other charge carriers to an exciton results in charged and higher excitonic complexes and a drastic change of the fine structure. An essential notion for the discussion of this fine structure is Kramers' degeneracy theorem from quantum

mechanics. Since this theorem significantly simplifies the analysis of the fine structure of particles with half-integer total spin (e.g. singly charged excitonic complexes) it will be outlined briefly in this section.

Time inversion in quantum mechanics for a stationary state is expressed by substituting a state Ψ with its complex conjugate Ψ^*. This follows from the fact that the time-dependent Schrödinger equation preserves its form when substituting t with $-t$ and going to the complex conjugate. If we include the spin s of the system and its projection s_z, the situation is slightly more complicated. Let TI be the time inversion operator, then

$$TI\Psi_{s,s_z} = (-1)^{s-s_z}\Psi^*_{s,s_z} \tag{2.18}$$

or

$$TI\Psi_{s,s_z} = (-1)^{s-s_z}\Psi_{s,-s_z}, \tag{2.19}$$

since time reversal inherently changes the sign of angular momentum [71]. The pre-factor is decisive for our considerations[12]. If we apply time inversion twice, we go back to the original system with its original eigenvalues. For the eigenstates we obtain

$$(TI)^2\Psi_{s,s_z} = (-1)^{s-s_z}TI\Psi_{s,-s_z} = (-1)^{2s}\Psi_{s,s_z}. \tag{2.20}$$

Consequently, only for systems with integer spin Ψ is transformed back to its original value. For systems with half-integer spin, however, the sign of Ψ changes. We have thus obtained two eigenfunctions Ψ_1 and Ψ_2 with $\Psi_1 = -\Psi_2$ for one eigenvalue ε: ε is (at least) twofold degenerate. Since electric fields are in general invariant under time reversal the presence of such fields does not alter this conclusion. This led *H. A. Kramers* 1930 to the formulation of the following theorem [72]:

> "For a system with half-integer value of the sum of all spins all states have to be at least twofold degenerate in arbitrary electric fields."

In our situation this means that all energetic states of excitonic complexes with half-integer total spin, such as singly charged excitons, are at least twofold degenerate. Note that this is not true any more if magnetic fields are applied since they break the symmetry of time inversion.

For a more elaborate discussion of Kramers' theorem see [71] Chap. 8, § 60 or [73]. The mathematical proof as given in the original paper [72] is reproduced in App. B.

---

[12]It has its origin in the transformation properties of the associated spin operators (see App. B).

2.2.5   Fine Structure of Singly Charged Complexes

With the help of Kramers' theorem it is now possible to discuss the fine structure of charged complexes.

Trions consist of one electron-hole pair and one extra charge carrier in the ground state. Since the two similar charge carriers occupy a closed shell, their total spin is zero due to the Pauli principle. The total spin of the trion is thus equal to the spin of the single charge carrier and is therefore half-integer. Only two possible states exist: $\left|\pm\frac{3}{2}\right\rangle$ for X^- and $\left|\pm\frac{1}{2}\right\rangle$ for X^+. According to Kramers' theorem these two states have to be degenerate in energy. It is trivial that the same is true for the final state, i.e. a single electron (hole) for X^- (X^+). Therefore, singly charged excitons do not display any fine structure in their spectra in the absence of a magnetic field.

For the initial state of the charged biexciton the situation is the same: Two electrons and two holes occupy closed shells and hence do not contribute to the complex' total spin. The excess charge carrier yields two possible spin states that are degenerate in energy. The situation changes for the final state, i.e. the excited (so-called "hot") trion (X^{+*}) where one of the two holes is in the first excited state. Here, all participating charge carriers occupy different shells and can therefore be in one of their two possible spin states independently from one another. For three charge carriers this yields eight (2^3) possible total spin states. Kramers' theorem, however, tells us that the degree of degeneracy can never be below two leaving four possibly different energy values for the hot trion. The possible recombination channels will be discussed for the positively charged biexciton only because of its relevance for this work. However, all considerations are valid for the negatively charged biexciton analogously. The discussion will closely follow the one given in [74] for the XX^-.

For simplification, the interaction terms can be separated into different hierarchies and be discussed one after another [75]. This has graphically been done in Fig. 2.9.

We start out with the aforementioned eightfold degenerate X^{+*}-state without any carrier-carrier interaction [Fig. 2.9 (a)]. The strongest interaction influencing the energy spectrum is the interaction between identical particles, here the two holes. Since we disregard the light holes and split-off holes, only the two heavy-hole spin configurations are possible ($\left|\pm\frac{3}{2}\right\rangle$). The two heavy holes physically behave like two spin-$\frac{1}{2}$ particles[13]. The spin interaction between two spin-$\frac{1}{2}$ particles gives the singlet-triplet structure known from basic quantum mechanics. The corresponding spin states in terms of total spin J and its projection J_z are $|0,0\rangle$ for the singlet and $|3,\pm3\rangle$ and $|3,0\rangle$ for the triplet. Together with the electron spin we receive the twofold degenerate states $\left|\frac{1}{2},\pm\frac{1}{2}\right\rangle$ originating from the singlet and the sixfold degenerate states $\left|\frac{7}{2},\pm\frac{1}{2}\right\rangle$,

---

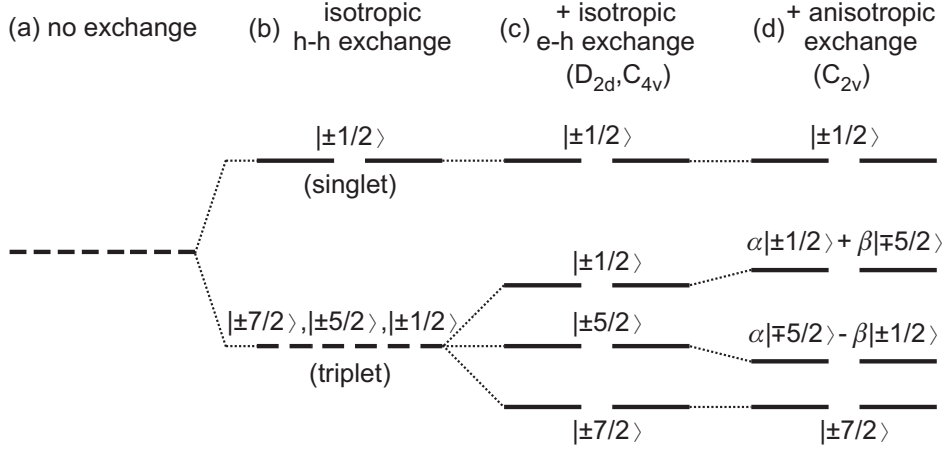[13]See also the concept of *pseudospin* in App. A.

Figure 2.9: Energy scheme for the hot trion states: (a) without exchange interaction, (b)with h-h and without e-h exchange interaction, (c) with full exchange interaction for, e.g., D_{2d} or C_{4v} symmetry, (d) with full exchange interaction for, e.g., C_{2v} symmetry. The numbers denote the projection of the complexes' total spin. The number of dashes gives the degree of degeneracy. α and β describe the mixing degree of the triplet states under anisotropic exchange.

$\left|\frac{7}{2}, \pm\frac{5}{2}\right\rangle$, and $\left|\frac{7}{2}, \pm\frac{7}{2}\right\rangle$ originating from the triplet [Fig. 2.9 (b)].

The isotropic e-h-exchange interaction lifts the triplet degeneracy, leading to four doublets [Fig. 2.9 (c)]. Note, that according to Kramers' theorem this degeneracy can not be lifted any further without a magnetic field, no matter how low the symmetry of the confinement may be. Consequently, lowering the symmetry to C_{2v} and hence introducing the anisotropic e-h-exchange does not further split the doublets contrary to the neutral-exciton case. It merely mixes some of the triplet states [Fig. 2.9 (d) and Tab. 2.2].

Analogously to the exciton case, the exchange Hamiltonian (Eq. 2.16) can be expressed in the basis of total hot trion spin states and reads:[14]

$$
\mathcal{H}^{ex} = \begin{pmatrix} 0 & \Delta_1/\sqrt{2} & \Delta_2/\sqrt{2} \\ \Delta_1/\sqrt{2} & \Delta_0 & 0 \\ \Delta_2/\sqrt{2} & 0 & -\Delta_0 \end{pmatrix},
\tag{2.21}
$$

where the rows and columns correspond to the triplet states $F_z = \left|\pm\frac{1}{2}\right\rangle, \left|\pm\frac{5}{2}\right\rangle$, and $\left|\mp\frac{7}{2}\right\rangle$ (App. A).

In order to discuss the influence of the electronic structure of the hot trion on the

---

[14]Some ambiguity concerning the energetic order of the unmixed triplet states, given by the diagonal terms, exists. The matrix (2.21) as derived in App. A suggests the order $|\pm\frac{5}{2}\rangle, |\pm\frac{1}{2}\rangle, |\pm\frac{7}{2}\rangle$. Single QD emission spectra in this and other works (e.g. [16]) clearly show that the $|\pm\frac{1}{2}\rangle$ states are above the $|\pm\frac{5}{2}\rangle$ states in energy as one would expect intuitively by ordering the states according to their spin. Figures 2.9 and 2.10 adopt the order given by the experiments.
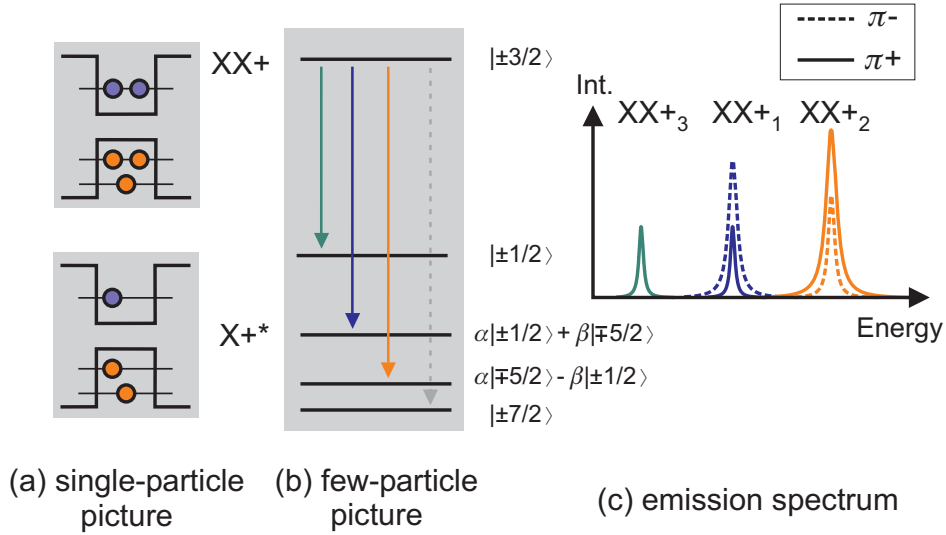
Figure 2.10: Transition scheme for the $XX^+ \to X^{+*}$ recombination. The broken gray arrow indicates a spin-forbidden transition. The numbers give the total spin projection of the corresponding state. $\pi+$ and $\pi-$ correspond to linearly (and orthogonally) polarized light.

spectra of the charged biexciton, the possible recombination channels have to be evaluated. The total spin of the charged biexciton ground state is $\left|\pm\frac{3}{2}\right\rangle$. Therefore, with a single photon only final states with total spin $\left|\pm\frac{1}{2}\right\rangle$ or $\left|\pm\frac{5}{2}\right\rangle$ are accessible. Furthermore, the recombining electron and hole have to have opposite spin. Consequently, also the remaining electron and ground-state hole have to have opposite spin. A look into Tab. 2.2 reveals, that the transition into the final state $\left|\pm\frac{7}{2}\right\rangle$ is completely forbidden, the transition into the final state $\left|\pm\frac{5}{2}\right\rangle$ is completely allowed and the transitions into the final states $\left|\pm\frac{1}{2}\right\rangle$ are partly allowed (since $\left|\uparrow, \Uparrow, \Downarrow\right\rangle$ is forbidden and $\left|\uparrow, \Downarrow, \Uparrow\right\rangle$ is allowed). Hence three transitions from the XX^+ to the X^{+*} are expected. The intensity of the transition into the $\left|\pm\frac{5}{2}\right\rangle$ states should be twice as high as the transitions into the $\left|\pm\frac{1}{2}\right\rangle$ states (Tab. 2.2 last column).

If the symmetry of the confining potential is lowered to C_{2v} the mixing of the trion states leads to an elliptical polarization of the transition lines. This is different from the exciton case and originates from the fact that the projection on the spin states $\left|\pm\frac{1}{2}\right\rangle$ and $\left|\mp\frac{5}{2}\right\rangle$ is not equal but depends on the two parameters α and β. The resulting states are thus [74]:

$$\alpha \left|\pm\frac{1}{2}\right\rangle \;+\; \beta \left|\mp\frac{5}{2}\right\rangle, \tag{2.22}$$

$$\alpha \left|\mp\frac{5}{2}\right\rangle \;-\; \beta \left|\pm\frac{1}{2}\right\rangle \tag{2.23}$$

symbol	single particle spin $\left| s, j_1, j_2 \right\rangle$	total spin $\left| F_z \right\rangle$	intensity
$\left| \uparrow, \Uparrow, \Uparrow \right\rangle$	$\left| \frac{1}{2}, \frac{3}{2}, \frac{3}{2} \right\rangle$	$\left| \frac{7}{2} \right\rangle_T$	0
$\left| \downarrow, \Uparrow, \Uparrow \right\rangle$	$\left| -\frac{1}{2}, \frac{3}{2}, \frac{3}{2} \right\rangle$	$\left| \frac{5}{2} \right\rangle_T$	1
$\left| \uparrow, \Uparrow, \Downarrow \right\rangle + \left| \uparrow, \Downarrow, \Uparrow \right\rangle$	$\left| \frac{1}{2}, \frac{3}{2}, -\frac{3}{2} \right\rangle + \left| \frac{1}{2}, -\frac{3}{2}, \frac{3}{2} \right\rangle$	$\left| \frac{1}{2} \right\rangle_T$	$1/2$
$\left| \uparrow, \Uparrow, \Downarrow \right\rangle - \left| \uparrow, \Downarrow, \Uparrow \right\rangle$	$\left| \frac{1}{2}, \frac{3}{2}, -\frac{3}{2} \right\rangle - \left| \frac{1}{2}, -\frac{3}{2}, \frac{3}{2} \right\rangle$	$\left| \frac{1}{2} \right\rangle_S$	$1/2$

Table 2.2: Four of the eight hot trion spin states in different notations. The remaining four states are obtained by multiplying all spins of the shown states by -1. $\uparrow$ ($\Uparrow$) in the first column denotes electron (hole) spin. The column "intensity" shows the expected relative intensity of the decay of an XX^+ into the corresponding X^{+*} state taking spin conservation into account.

with

$$\alpha = \arccos \left[\frac{1}{2} \arctan \left(\sqrt{2} \frac{\Delta_1}{\Delta_0} \right) \right], \tag{2.24}$$

$$\beta = \arcsin \left[\frac{1}{2} \arctan \left(\sqrt{2} \frac{\Delta_1}{\Delta_0} \right) \right]. \tag{2.25}$$

Only for the limit of $\alpha = \beta$, which requires $\Delta_1 \gg \Delta_0$, the polarization would be linear.

The term Δ_2 additionally mixes the dark states $\left| \pm \frac{7}{2} \right\rangle$ with allowed states, thus introducing a new, partly allowed transition. I. A. Akimov and coworkers, however, pointed out, that Δ_2 is due to a relativistic correction of the conduction band and is usually of negligible magnitude [74]. In fact, in their experiments on single CdSe QDs they did not observe an extra transition although generally, exchange effects are greatly enhanced in II-VI QDs with respect to III-V materials. For the exciton, Δ_2 has been measured in magneto-optical experiments and has been determined to 0.1 Δ_1 in CdSe QDs [76] and 0 and 0.5 Δ_1 in two different InAs QDs [22]. It is therefore safe to neglect Δ_2 in the discussion. This will be justified in hindsight by the experimental results in Chap. 4.

If the corresponding transition lines can be correctly identified in the single-QD spectra, it is therefore possible to measure the singlet-triplet splitting, the triplet splitting (Δ_0 in Eq. 2.21) and the mixing term Δ_1. Δ_1 is particularly interesting because it is connected to the FSS; both parameters give the degree of anisotropy of the confining potential.

2.2.6 Fine Structure of Multiply Charged Complexes

Another complex with a pronounced fine structure will be discussed here for the sake of correctly interpreting the experimental spectra: the doubly charged exciton. Again, the positive complex, i.e. the X^{++} will be discussed here but the train of thought is analogous for the X^{--}.

The X^{++} is somewhat more complicated than the previously discussed complexes, because here both, initial and final states, are split. Nonetheless, with the considerations developed in the previous section, the analysis is straightforward.

First, the initial state, the X^{++}, has to be considered (Fig. 2.11 upper panel). The QD is occupied with one electron in the ground state, two holes in the ground state and one hole in the first excited state [Fig. 2.12 (a)]. Since the two holes in the ground state have to have zero total spin due to the Pauli principle, the energetic structure is governed by the exchange interaction between one electron and a hole complex with the same total spin as a single hole (Eq. 2.17), similar to the exciton. Indeed, the previously discussed dark and bright doublets are recovered (see Fig. 2.11 upper panel). The magnitude of the splittings, however, will be different, since the interaction is now between the electron in the ground state and a three-hole complex.

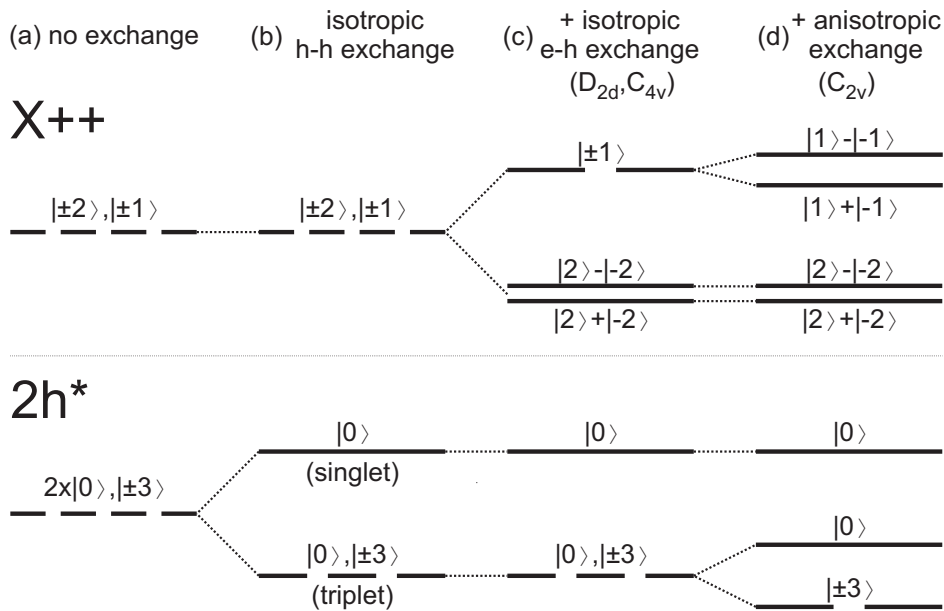The final state of the transition comprises two holes, one in the ground state and

Figure 2.11: Energy scheme for the initial and final states of the doubly positively charged exciton decay: (a) without exchange interaction, (b) with h-h and without e-h exchange interaction, (c) with full exchange interaction for, e.g., D_{2d} or C_{4v} symmetry, (d) with full exchange interaction for, e.g., C_{2v} symmetry. The number of dashes gives the degree of degeneracy.
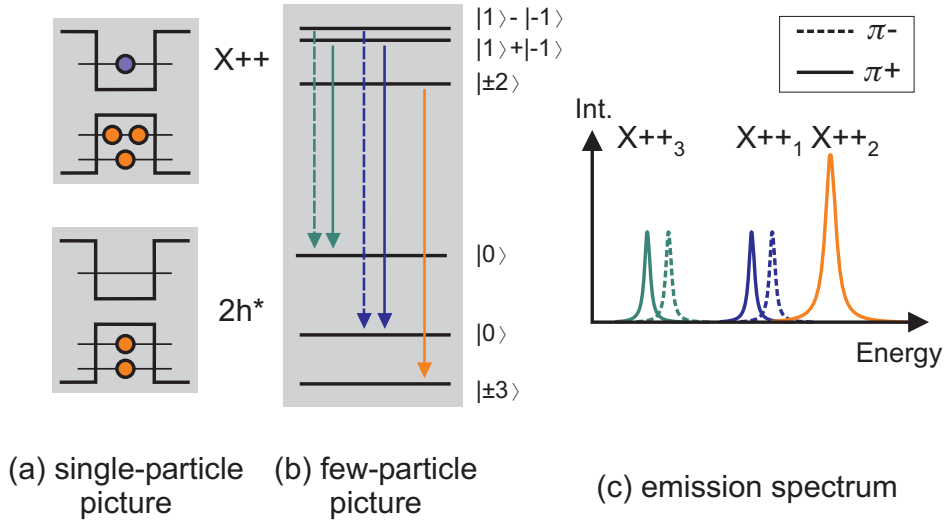
Figure 2.12: Transition scheme for the $X^{++} \rightarrow 2h^*$ recombination. The numbers give the total spin projection of the corresponding state. $\pi+$ and $\pi-$ correspond to linearly (and orthogonally) polarized light.

one in the first excited state. The exchange interaction again yields the singlet-triplet structure discussed in the last section. Interestingly, M. Edinger and coworkers point out, that in a quantum dot the splitting of the triplet states under full exchange is unique to holes and does not occur for electrons [77]. The lower panel in Fig. 2.11 shows the energetic structure of the two holes. Naturally, electron-hole exchange interaction has no effect here, since no electrons are present.

Figure 2.12 again shows the analysis of the occurring transitions between all possible initial and final state configurations. Again, Δ_2 will be neglected for the reasons mentioned in Sec. 2.2.5 and in accord with calculations by the group of A. Zunger [77] for the X^{++}. Three main features should thus be visible in the spectra. Two of them are composed of polarized doublets resembling the splitting between the two initial states $|1\rangle - |-1\rangle$ and $|1\rangle + |-1\rangle$. The analysis of the corresponding spectra should therefore yield the "bright" splitting of the X^{++}, which will be compared to the X FSS and the triplet splitting of the two holes (combined with the "dark-bright" splitting of the X^{++}), which will be compared to the XX^+ case in Chap. 4.

In summary this section gave a general analysis of the Coulomb interaction in QDs. The importance of direct Coulomb interaction, correlation, and exchange interaction was discussed. Different emission energies for different excitonic complexes and a unique fine structure for each complex are predicted. Consequently, this analysis set the stage for successful identification of different lines in a single-QD spectrum and for comparison between theory and experiment especially concerning the variety of exchange energies mentioned.

2.3   Electric Fields – Quantum Confined Stark Effect

Real semiconductor crystals in which the QDs are embedded are never ideal. That means they contain a number of defects of various types, such as interstitial defects, vacancies, doping atoms, screw and step dislocations. Additionally, the QD material considered here has a larger lattice constant than the surrounding matrix material. Even if the QDs grew pseudomorphically this results in strain fields nourishing the development of defects. All these defects result in energy states which can be occupied or empty (i.e. charged or neutral). The same is true for surface or interface states that inevitably form at the interfaces of two different materials.

The vast number of hot electrons and holes generated by the electron beam in the cathodoluminescence setup lead to a constant charging and discharging of these states, introducing electric fields in the vicinity of the QDs. These fields lead to a bending of the electronic bands of the QD (Fig. 2.13) thus influencing the energies of the transitions in the QD.

Following the notation in atomic physics this effect has been dubbed *Quantum Confined Stark effect* [78]. Three different effects are induced by the band bending:

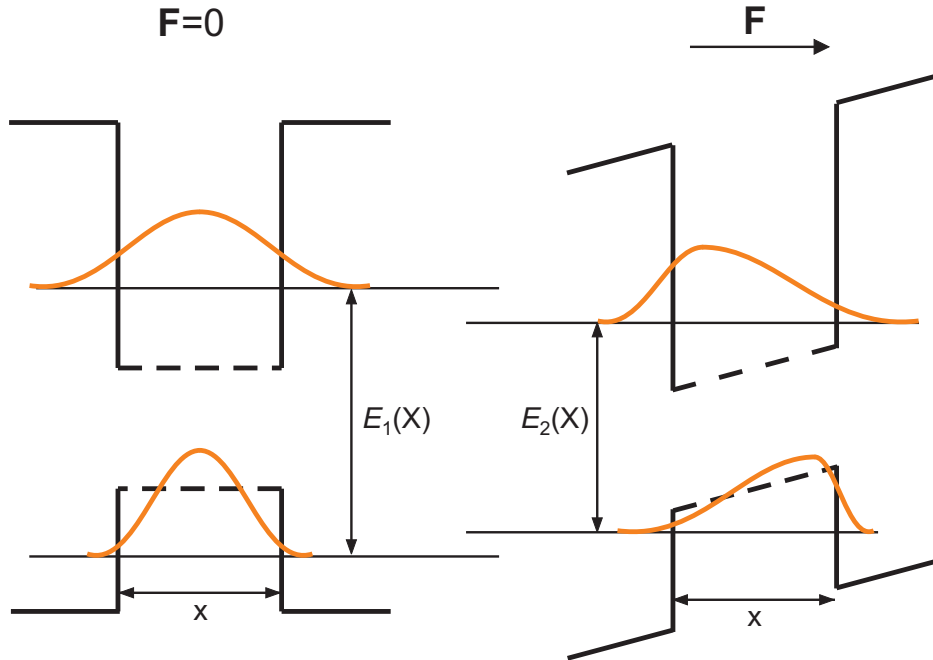1. Electrons and holes follow the electric field both lowering their energy (i.e. elec-

Figure 2.13: Energy scheme of a QD with and without external electric field **F**. The electron and hole wave functions are shown in orange. Due to the band bending under the electric field, the exciton transition energy $E(X)$ changes.

trons moving down in the energy scheme, holes moving up) (Fig. 2.13). The recombination energy is thus lowered, leading to a red shift of the corresponding transition.

2. Due to the spatial separation of electron and hole the exciton binding energy is reduced. This effect raises the energy of the exciton leading to a blue shift of the corresponding transition. This is also true for higher excitonic complexes, because the attractive Coulomb terms (C_{eh}) are reduced.

3. The spatial separation decreases the oscillator strength and therefore the time-averaged intensity of the corresponding transition.

The first effect dominates over the second one thus leading to an overall redshift of the luminescence with increasing electric field [78].

The continuous charging and discharging of states surrounding the QDs leads to slight variations in the energy of the transition lines. The amplitude of this jitter can be up to several meV (see Sec. 3.3). Since the exact evolution of the jitter is a function of the local electric fields in the QDs, all lines from one QD will display the same jitter pattern thus providing a fingerprint for a specific QD. The jitter thus represents a powerful tool to identify spectra of individual QDs when the QD density is too high to only excite or detect one QD at a time [17] (see Sec. 3.3). Note, that the *amplitude* of the jitter can vary from one excitonic complex to the other due to the different ability of the complexes to screen the electric fields and their different dipole moments.

2.4   Carrier Dynamics

This section will discuss the homogeneous broadening of discrete transitions and the recombination dynamics of excitonic complexes in a QD and in how far it is influenced by the electronic fine structure.

If an exciton is excited it induces a polarization **P** in the surrounding medium due to its electromagnetic field. The first scattering process that occurs destroys the coherence with the original field: the quantum mechanical phase is lost. Scattering processes that destroy the phase are divided into processes with energy relaxation, e.g. emission or absorption of a phonon or, ultimately, recombination of the exciton, and *pure* phase-relaxing processes under energy conversion, e.g. scattering with ionized impurities and defects (not applicable for spatially confined QD excitons), Coulomb scattering with free electrons or excitons or elastic phonon scattering. The characteristic time at which the fraction of the polarization that is still coherent with the original field decays to its e^{-1}-th part is called phase relaxation time T_2. It is divided into components T_1

for processes with energy transfer and T_p for processes under energy conversion and is given by

$$\frac{1}{T_2} = \sum_i \frac{1}{2T_{1,i}} + \sum_j \frac{1}{T_{p,j}}.^{15} \tag{2.26}$$

T_2 is connected to the homogeneous line width Γ of the corresponding transition line via the Heisenberg uncertainty principle:

$$\Gamma = \frac{2\hbar}{T_2}. \tag{2.27}$$

In a luminescence spectrum, this results in a Lorentzian line shape of the transition line with a finite full width at half maximum. A completely discrete resonance as suggested by the δ-function-like DOS will therefore not be observed no matter how high the spectral resolution of the setup. This effect is called homogeneous broadening (compare to inhomogeneous broadening Fig. 2.4). In QDs and at low temperatures a typical recombination time $T_{1,rec}$ of excitons is on the order of 1 ns thus resulting in a homogeneous line width of 1.3 μeV. In this case the $T_{p,j}$ are long compared to $T_{1,rec}$ and therefore do not contribute much to Γ. Consequently, the resulting T_2 can only be measured via Γ using extremely high resolving luminescence setups (e.g. [79]) or employing phase sensitive techniques such as four wave mixing [80].

In the following, $T_{1,rec}$ will be examined in more detail. If a QD is occupied with an exciton the population N of the exciton state is 1. After spontaneous recombination and emission of a photon the population is 0. The question to be discussed here is how "fast" this recombination process takes place, i.e. after what time the population decreases from 1 to 0. If the experiment is repeated, this time will not necessarily be the same since recombination is a statistical process. Therefore, the experiment has to be rerun a number of times to acquire an "average" dynamic behavior. The population will then denote the average population the QD will have after a certain amount of time, or the probability of finding the QD in that particular state. If in half of the cases the QD will have recombined after a time $t_{1/2}$, then the population at $t_{1/2}$ is 0.5. The characteristic lifetime $T_{1,rec} = \tau$ is the time where $N(t) = \frac{N_0}{e}$.

In the simplest case the decline of the population of a state due to recombination is proportional to the population itself. In bulk semiconductors one has to additionally take band-to-band recombination of free carriers into account which is a bi-molecular process, i.e. the rate of decline is proportional to n^2 [81]. In a QD, however, when a pure 2-level exciton system is assumed the decline of the population can be described

---

[15]The factor of 2 originates from the comparison between the polarization $\mathbf{P} = \mathbf{P}_0 \exp(-t/T_2)$ and the population $N = N_0 \exp(-t/T_1)$ of a state, where $N \sim I$ (emission intensity) $\sim |E|^2$ (electric field) $\sim P^2$.

by the simple differential equation

$$\frac{dN(t)}{dt} = -RN(t) \tag{2.28}$$

where $R = \frac{1}{\tau}$ is the *rate* at which the intensity declines. The solution is the well-known formula for mono-exponential decay:

$$N(t) = N_0 \cdot e^{-\frac{t}{\tau}}. \tag{2.29}$$

The population can be monitored by measuring the temporal evolution of the intensity of the exciton emission, i.e.

$$I(t) = I_0 \cdot e^{-\frac{t}{\tau}}. \tag{2.30}$$

The recombination lifetime is composed of radiative (i.e. conversion of electron-hole pairs into photons) and non-radiative (e.g. emission or absorption of phonons) components. In high-quality semiconductor materials with few defects and at low temperatures, where the phonon branches are almost empty, the lifetime is dominated by recombination, i.e. radiative processes. The radiative lifetime of an exciton is given by [82]

$$\tau_{rad} = \frac{2\pi\varepsilon_0 m_0 c^3}{ne^2 E_X f_{eff}}, \tag{2.31}$$

where

$$
\begin{aligned}
\varepsilon_0 \quad &- \quad \text{vacuum permittivity,} \\
m_0 \quad &- \quad \text{free electron mass,} \\
c \quad &- \quad \text{vacuum speed of light,} \\
n \quad &- \quad \text{index of refraction of the corresponding material,} \\
e \quad &- \quad \text{elementary charge.}
\end{aligned}
$$

It is therefore a function of both the exciton transition energy E_X and the effective oscillator strength f_{eff} that is obtained by integrating the oscillator strength over the unit square.

Of course the QD can be in more states than just being empty or occupied by an exciton. Every excitonic complex can have its own unique lifetime since it has its own unique oscillator strength. Furthermore, the radiative lifetime of an excitonic complex (EC) is composed of the *characteristic transition times* $\tau_{i,f}(EC)$ of all allowed transition channels from initial states i to final states f [83]:

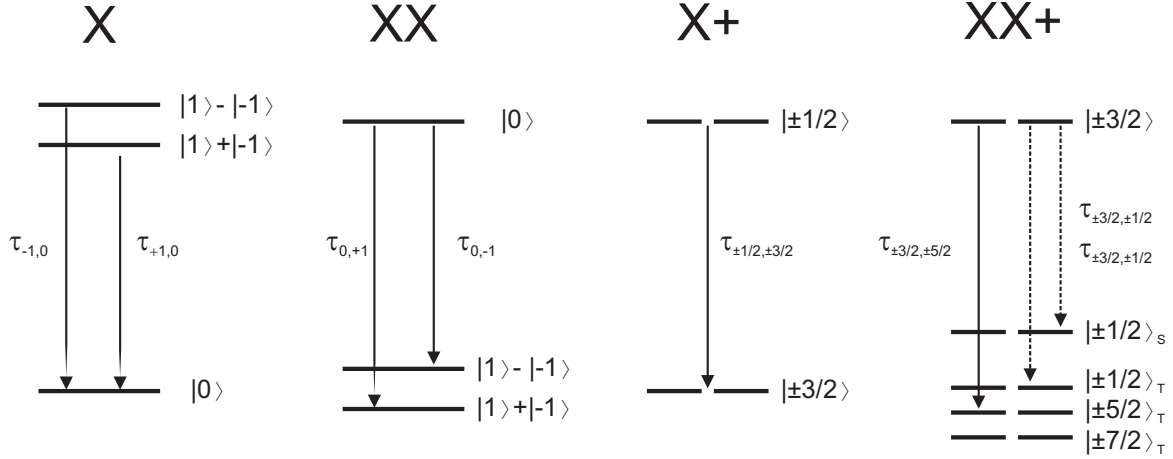$$\frac{1}{\tau(EC)} = \sum_{i,f} n_i \frac{1}{\tau_{i,f}(EC)}, \tag{2.32}$$

Figure 2.14: Possible recombination channels for the X, XX, X$^+$ and XX$^+$ decay. The n participating electronic states for each complex are labeled with their total spin state $|F_z\rangle$. Broken lines indicate the degree of degeneracy. Broken arrows denote transitions with reduced transition probability.

where n_i is the mean population of the state i.

Consequently, the fine structure discussed in the last section plays an important role in the analysis of the lifetimes, because it determines the number of recombination channels.

We will assume that all characteristic transition times for a certain excitonic complex are identical, i.e. $\tau_{m,n}(EC) = \tau_{k,l}(EC) = \tau_{EC}$ where the transitions $m \rightarrow n$ and $k \rightarrow l$ are allowed. This assumption is sensible since the oscillator strength is independent of the actual spin configuration as long as the spin selection rules are obeyed. Under this precondition we will now determine the expected lifetimes of X, X$^+$, XX, and XX$^+$ merely by counting the number of possible recombination channels for each complex.

Figure 2.14 shows the decay schemes for the excitonic complexes in question as derived in the last section. States that do not play a role for recombination (i.e. dark states) have been omitted.

The exciton has two recombination channels. For a sufficiently small FSS and disregarding any spin-flip processes the population of the two bright exciton states is 0.5. Therefore, the radiative lifetime of the exciton amounts to

$$\frac{1}{\tau(\text{X})} = \frac{1}{2}\frac{1}{\tau_{-1,0}} + \frac{1}{2}\frac{1}{\tau_{+1,0}} \approx \frac{1}{\tau_\text{X}}. \tag{2.33}$$

Correspondingly, the radiative lifetime of the biexciton amounts to

$$\frac{1}{\tau(\text{XX})} = \frac{1}{\tau_{0,-1}} + \frac{1}{\tau_{0,+1}} \approx 2\frac{1}{\tau_\text{XX}}. \tag{2.34}$$

The initial $\left(\left|\pm\frac{1}{2}\right\rangle\right)$ and the final states $\left(\left|\pm\frac{3}{2}\right\rangle\right)$ of the X^+ decay are both twofold degenerate (Fig. 2.14). The X^+ lifetime therefore amounts to

$$\frac{1}{\tau(X^+)} = \frac{1}{2}\frac{1}{\tau_{+1/2,+3/2}} + \frac{1}{2}\frac{1}{\tau_{-1/2,-3/2}} \approx \frac{1}{\tau_{X^+}}. \tag{2.35}$$

In the XX^+ case, four transitions have to be taken into account. Note, that two of these transitions are only "half-allowed" (see Tab. 2.2). The total radiative lifetime of the XX^+ therefore accounts to

$$
\begin{aligned}
\frac{1}{\tau(XX^+)} &= \overbrace{\frac{1}{2}\left(\frac{1}{2}\frac{1}{\tau_{+3/2,+5/2}} + \frac{1}{2}\frac{1}{\tau_{-3/2,-5/2}}\right)}^{\text{singlet transition}} \\
&+ \frac{1}{2}\left(\frac{1}{2}\frac{1}{\tau_{+3/2,+5/2}} + \frac{1}{2}\frac{1}{\tau_{-3/2,-5/2}}\right) \\
&+ \frac{1}{2}\frac{1}{\tau_{+3/2,+5/2}} + \frac{1}{2}\frac{1}{\tau_{-3/2,-5/2}} \\
&\approx 2\frac{1}{\tau_{XX^+}}. \tag{2.36}
\end{aligned}
$$

The question is in how far the characteristic transition times differ among the excitonic complexes and from transition to transition. G. A. Narvaez and coworkers calculated in Ref. [83] the characteristic transition times of the X, $X^{-/+}$, and XX recombination channels and the resulting radiative lifetimes for lens-shaped $In_{0.6}Ga_{0.4}As/GaAs$ QDs of different height. Independent of height, they found that the characteristic transition times of exciton and biexciton $\tau_{-1,0}(X)$, $\tau_{+1,0}(X)$, $\tau_{0,-1}(XX)$, and $\tau_{0,+1}(XX)$ differ only very slightly. The characteristic transition times of the trions by contrast depend strongly non-monotonically on QD height and also differ among each other, e.g. $\tau_{i,f}(X^+) \neq \tau_{i,f}(X^-)$ for all QDs calculated.

Under the assumption that an equal charge state results in similar characteristic transition times, we expect for the neutral complexes

$$\frac{\tau(X)}{\tau(XX)} \approx 2 \tag{2.37}$$

and, for the charged complexes

$$\frac{\tau(X^+)}{\tau(XX^+)} \approx 2. \tag{2.38}$$

Deviations of the experimental values of these two ratios are then due to differences in characteristic transition times from complex to complex.

Chapter 3

Experimental

This chapter gives an overview of the experimental techniques used throughout this work. The first section describes the experimental setup and the generation of secondary electron and cathodoluminescence images. The second section outlines the epitaxial growth of quantum dots (QDs) and introduces the samples that were examined in this work. An overview of the possibilities to isolate single-QD spectra concludes this chapter.

3.1 Cathodoluminescence Spectroscopy

Single-QD spectroscopy aims at unveiling features in the spectra of semiconductor QDs that would normally be hidden under the inhomogeneously broadened ensemble peak (see Sec. 2.1.2). However, obtaining these spectra is a very challenging task, that requires high standards of spatial and spectral resolution of the spectroscopic setup. Three different techniques are generally used worldwide to meet these challenges. By far the most common technique is confocal microscopy for micro-photoluminescence (μPL) and micro-photoluminescence-excitation (μPLE) spectroscopy. Here, the exciting light[1] is coupled into an optical microscope objective ideally producing an excitation spot below one μm. The luminescence light is collected through the same objective and subsequently analyzed with a monochromator and a detector. Another possibility is scanning near-field optical microscopy (SNOM) [84]. Here, the excitation light passes through a glass tip with a diameter much smaller than the wavelength of the light. The sample is then excited by the evanescent light field in the immediate vicinity of the tip. In principle this technique allows resolutions in the sub-wave-length range thus circumventing the limit given for conventional optical microscopes (as used for μPL). However, the experimental effort is higher than in μPL and the collection efficiency, in

---

[1]different laser systems or high brightness lamps can be used

general, is lower.

Here, cathodoluminescence spectroscopy based on a scanning electron microscope (SEM) is conducted [85]. It uses high voltage electrons in the 10 kV range as excitation source. The wavelength of such electrons is on the order of 10 pm well below the wavelength of photons. Even though the aberration of the magnetic lenses is high this technique can still provide resolutions in the nm range. A thorough introduction to cathodoluminescence spectroscopy can be found in [86]. The specific setup used here will be described in the next section.

3.1.1   Experimental Setup

The cathodoluminescence setup is based on a commercially available SEM of the type JEOL JSM 840. It has been additionally equipped with a light detection system consisting of a monochromator and a suitable detector. A schematic overview of the setup is shown in Fig. 3.1.

The SEM consists of a gun section that generates the electron beam. The electrons are thermally emitted by a LaB_6 cathode that is heated to 1500 °C. From the cloud
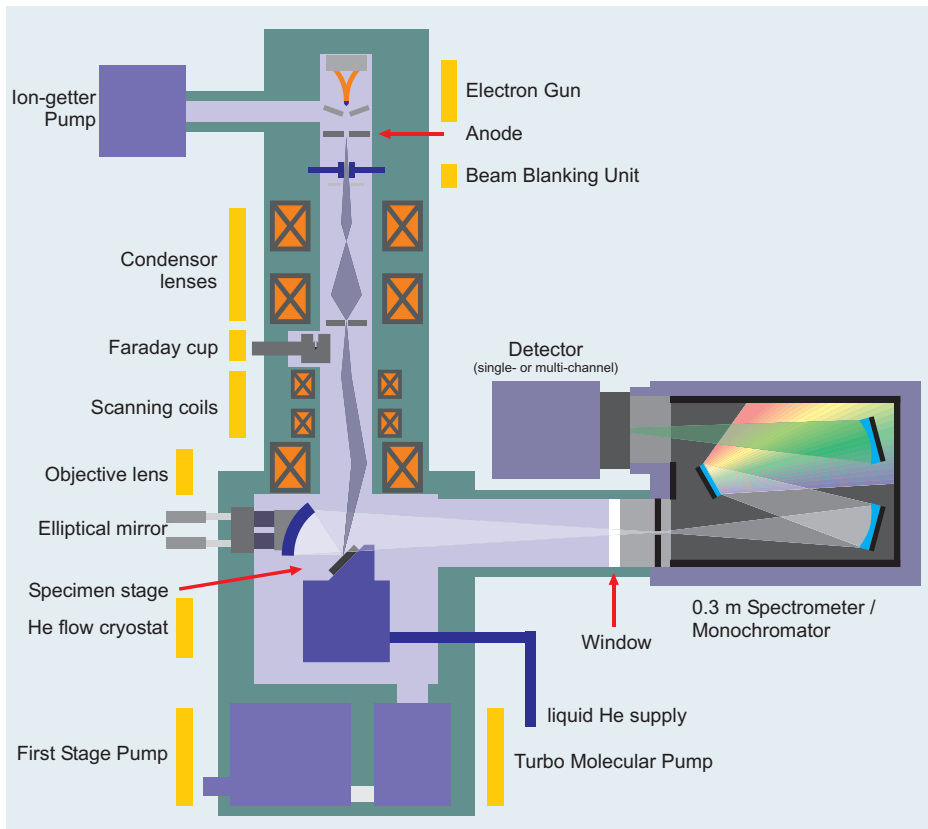

Figure 3.1: Schematic view of the cathodoluminescence setup described in the text (image taken from [87]). Light-blue areas indicate high-vacuum regions.

of electrons that forms around the crystal electrons are then accelerated towards the anode by a high-voltage electric field thus producing the electron beam. The voltage can be varied for this particular SEM between 3 and 40 kV. A negatively biased Wehnelt cap additionally focuses the beam. The electrons then pass through a system of magnetic coils that correspond to optical lenses in an optical microscope and are therefore dubbed magnetic lenses. Analogously to the light in a microscope, the electron beam passes through condensor and objective lenses. When the high energy electron beam hits the sample a number of different processes are initiated such as generation of x-ray Bremsstrahlung, Auger processes, backscattering of primary electrons, and others. Two processes are important for the setup shown in Fig. 3.1. On the one hand secondary electrons from the semiconductor crystal leave the sample when enough energy is transferred from the primary electrons of the exciting electron beam. The amount of secondary electrons emitted into a given solid angle depends on the surface topology of the material and the material itself. Collecting these electrons with an electron detector combined with scanning over the sample with the help of scanning coils produces the SEM image yielding the corresponding information about the sample surface.

On the other hand, one primary electron can generate up to[2] 1000 electron hole pairs via high-energy collision processes and re-absorption of Auger and x-ray radiation thus ionizing the semiconductor atoms. The electron hole pairs thermalize via the emission of photons, phonons, scattering and Auger processes, and ionization of lattice atoms and can then be captured in potential wells (e.g. QDs) where they recombine. This corresponds to above-band gap excitation with a laser beam only with much larger energies. While the energy of the exciting photons in photoluminescence setups are usually on the order of the band gap of the semiconductor, i.e. a few eV, the energy of the primary electrons in an SEM is on the order of a few keV. The light emitted via recombination of the electron-hole pairs is called cathodoluminescence and carries information about the electronic structure of the sample constituting the subject of interest for this work.

High vacuum is necessary to operate an SEM since the mean free path of the electrons has to be long enough for them to reach the sample surface without being absorbed or scattered by residue gas molecules. This is provided for by different pumping systems. A pre-stage consisting of a diaphragm pump and a small turbo molecular pump provides a pressure low enough for the exhaust of a big turbo molecular pump. Additionally, an ion getter pump is installed near the gun section of the microscope. It further decreases the pressure near the cathode in order to grant a long lifetime of the

---

[2]depending on the energy of the electron beam and the band gap of the semiconductor material

LaB$_6$ crystal. The system is supplemented by a cryogenic trap. It operates with liquid nitrogen and freezes residue gas molecules to its surface. The final pressure inside the chamber is as low as 10^{-7} mbar.

The sample is mounted onto a flow cryostat supplied with liquid helium with an integrated heating system. It provides temperatures between 6 and 300 K.

The optical detection system consists of an elliptical mirror that reflects the cathodoluminescence light into a 30 cm monochromator and adjusts the beam to the aperture of the monochromator. The monochromator can be equipped with a number of gratings with different line densities ranging from 50 to 1200 lines per mm providing different spectral resolutions and different blaze angles for different detection wavelengths. A slot in front of the monochromator can host an optical analyzer foil, which enables polarization dependent measurements. Two different multi-channel detectors were used for the measurements depending on the wavelength of the light to be detected. A liquid nitrogen-cooled Si CCD camera sensitive between 350 and 1050 nm or a liquid nitrogen-cooled InGaAs diode array for wavelengths between 850 and 1700 nm can be employed. Both detectors were manufactured by Princeton Instruments. The maximum spectral resolution as given by this setup is 120 μeV at a typical photon energy of 1.3 eV.

3.1.2   Time-Resolved Measurements

For time-resolved measurements a beam blanking unit is introduced into the beam path just below the anode (see Fig. 3.1). It consists of a plane-parallel capacitor connected to a high-frequency rectangular voltage signal with a typical amplitude of 5 V that can deflect the electron beam such that no electrons reach the sample and thus no luminescence is excited. The rise and fall times of the electron beam are better than 120 ps [88]. A typical pulse length is 5 ns at a repetition rate of 25 MHz. This pulse configuration allows a luminescence decay from a steady-state situation thus excluding any influence of initial carrier capture and relaxation processes on the measured transients.

A Si avalanche photo diode (APD) SPCM-AQR-13 from Perkin Ellmer was employed as a detector. It has a photon detection efficiency above 15 % between 420 and 990 nm with a peak efficiency of 65 % at 650 nm and a dark count rate of 200 counts/s. Its sensitivity in the wavelength range important for small InAs QDs between 900 and 950 nm is unmatched by any other fast photodetector on the market which makes it the most common choice for single-dot time-resolved spectroscopy on InAs QDs. Its weakness is the comparatively broad instrument response function with a full-width at half maximum of 350 ps [89]. The APD timing pulses are fed to an
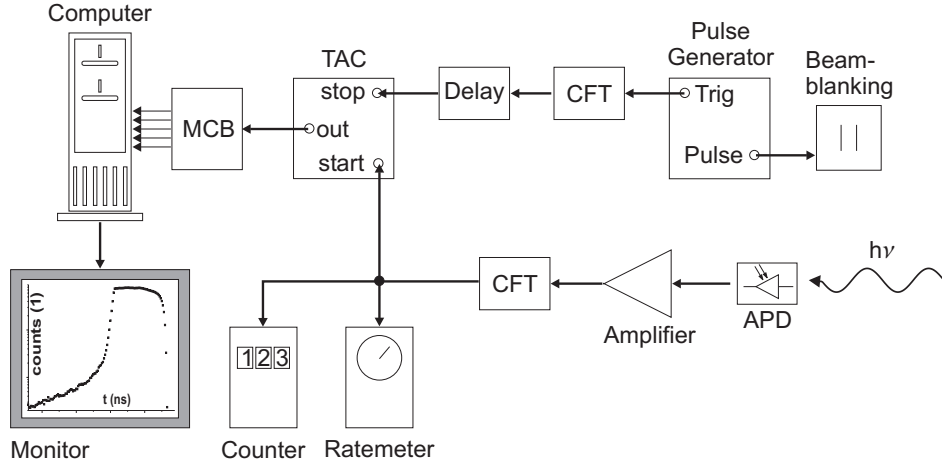
Figure 3.2: Schematic of the inverted time-correlated single-photon-counting chain with constant fraction trigger (CFT), time-to-amplitude converter (TAC), avalanche photo diode (APD), and multi-channel buffer (MCB).

inverted time-correlated single-photon-counting chain shown schematically in Fig. 3.2. It contains constant fraction trigger modules, a time-to-amplitude converter, and a multichannel buffer that is read out by a computer. A thoroughgoing fitting procedure of the measured transients that is presented in App. C sustains accuracies of ± 100 ps of the measured decay times.

3.1.3 Cathodoluminescence Mapping

A specific strength of the CL setup is the possibility to simultaneously record an SEM image and cathodoluminescence data. In this way structural and spectroscopic data can be combined to achieve information about the spatial origin of the detected luminescence. This can be optimized by recording so-called CL maps where a full spectrum is taken for every point of the SEM image. This is possible in a reasonable amount of time only when employing a multi-channel detector. Thus, four-dimensional data blocks are recorded with information on the two spatial coordinates x and y and for every pair of such coordinates a complete spectrum, i.e. wavelength λ and intensity I. Naturally, it is not possible to display the full information contained in $I(x, y, \lambda)$ in one single graph. However, depending on the specific situation monochromatic CL maps $[I_{\lambda_0}(x, y)]$ or polychromatic CL maps $[I_{\lambda_1}^{\lambda_2}(x, y) = \sum_{\lambda=\lambda_1}^{\lambda_2} I_\lambda(x, y)]$ can be generated. This technique makes it possible to locate QDs in a small-QD-density sample and to relocate QDs after the sample had been temporarily removed from the sample stage (see Sec. 3.3).

In order to initially locate the QDs a third CL mapping format turned out to be more favorable: the intensity at the wavelength with maximum intensity $I_{max}(x, y) =$

$I_{\lambda(I_{max})}(x, y)$. This is especially helpful if shoulders of broader peaks (e.g. the wetting layer) are in the chosen spectral window since such broader peaks have a large polychromatic intensity and a small monochromatic intensity with respect to the sharp QD resonances. The wetting layer therefore disturbs the $I_{\lambda_1}^{\lambda_2}$ images but is suppressed in the I_{max} images.

Examples of I_{max} and I_{λ_0} images can be seen in Fig. 3.7 and Fig. 4.14, respectively.

3.2   Epitaxial Growth of Quantum Dots and Examined Samples

In homoepitaxial processes, where identical semiconductor materials are grown on top of each other or if the lattice constants of different materials are almost identical (i.e. AlGaAs on GaAs) closed layers of material form one after the other in order to minimize the surface energy (Frank-van-der-Merve growth mode).

In heteroeptaxial processes different crystalline materials are combined that will generally have different lattice constants. Epitaxially grown QDs can form via self-organization when the QD material has a larger lattice constant than the matrix material. The total energy of the system then includes surface, strain, and volume energy. Under certain growth parameters and for certain materials it is energetically favorable to not form closed layers thus minimizing surface energy but maximizing strain energy but to form nanometer-sized islands just like water drops on a hydrophobic surface. This can happen either on a one monolayer thick so-called wetting layer (Stranski-Krastanow growth mode) or directly on the matrix material (Vollmer-Weber growth mode). For optimal optical quality of the sample it is important that the QD crystal structure is free from defects. Otherwise charge carriers would recombine non-radiatively at such defect states. The QD would be optically inactive. Obtaining such defect-free structures is by no means trivial and requires a lot of know-how. Today, epitaxially grown quantum dots can be fabricated in a number of material systems, such as InAs in GaAs, InP in InGaP, CdSe in ZnSe or GaN in AlGaN.

The QDs examined in this work are grown in an Aixtron metal-organic chemical vapor deposition (MOCVD) machine. The metal-organic source material, so-called precursors, are directed into the MOCVD reactor where high temperatures break them up into their metallic and organic components. Depending on the offered substrates and growth parameters such as temperature, pressure, and mass flow semiconductor crystals form on the substrate. The gaseous remnants are removed from the reactor. It is also possible with this technique to intentionally introduce contaminants into the reactor to grow doped semiconductor layers. This is mandatory for the production
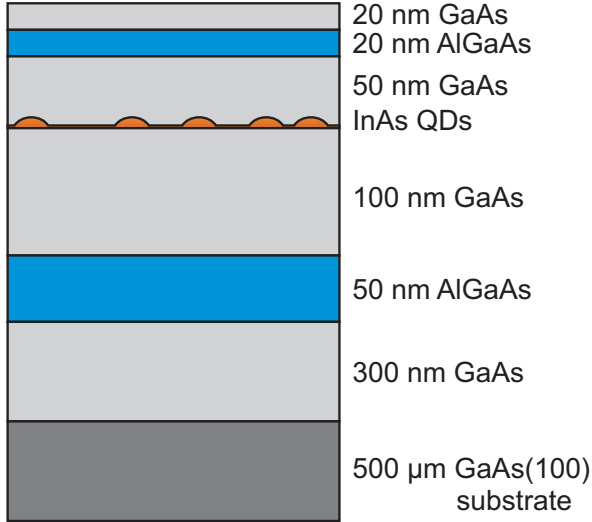
Figure 3.3: General sample structure of the samples examined in this work. The exact structure of the active QD layer varies from sample to sample and is described in the text. AlGaAs diffusion barriers are introduced in order to provide a higher luminescence yield.

of electronic devices. The crystals grown here consist of Al, Ga, In and As from the alternative precursors trimethylindium, -gallium, -aluminum and tertiarybutylarsine. The QDs consist of (In,Ga)As embedded in a GaAs matrix. This material crystallizes in the cubic zinc-blende crystal structure. It is a direct semiconductor with band gaps of 1.52 eV for GaAs and 0.42 eV for InAs at cryogenic temperatures [53]. This makes this material system interesting for telecom applications. The important wavelengths here are 1.3 μm (= 0.954 eV) and 1.55 μm (= 0.8 eV) dictated by minima in the dispersion and attenuation of commonly used optical fibers. These wavelengths can in principle be reached by combining InAs and GaAs in the ternary alloy InGaAs. Practically, however, problems like low crystal quality of thick In-rich layers and modification of the band gap via strain fields make the production of opto-electronic devices in these wavelength regions solely based on InAs and GaAs very challenging.

The basic sample structure is similar for all samples examined here and is given in Fig. 3.3. The AlGaAs layers have a larger band gap than the surrounding GaAs and thus serve as diffusion barriers for the charge carriers. This way the probability for the charge carriers to reach the QDs is enhanced and thus the luminescence yield increases. The important and innovative concepts that make the samples interesting and suitable for single-QD spectroscopy are connected with the growth of the active QD layer itself. Three samples have been examined in detail:

Sample ML (<u>M</u>ono<u>L</u>ayers): In this sample subensembles of self-similar QDs with different height and base length have formed. The self-similarity of the QDs within the same sample makes it possible to link their electronic structure directly to the QD height. Additionally, the energy range of QD emission is extremely wide spreading from 1.05 to 1.38 eV. Metallic shadow masks have to be used to isolate single-QD spectra (see Sec. 3.3).

Sample NR (No Rotation): During growth of the QDs the rotation of the wafer was shut off. This led to a gradient of QD density and makes single-QD spectroscopy without shadow masks possible in some regions of the sample.

Sample GI (Growth Interruption): An extremely long growth interruption after deposition of the QD material leads to the formation of mainly large QDs. Only a few small QDs remain, since they are spectrally separated from the large QDs. This again makes single-QD spectroscopy without shadow masks possible.

In the following the examined samples and their characteristics are presented in greater detail.

3.2.1   Multi-Modal Quantum Dot Distribution

The ensemble PL spectrum of **sample ML** displays a pronounced oscillatory behavior (Fig. 3.4). It has its origin in a special growth mode of the QD layer.

After the QD material had been deposited, a 5 s growth interruption was introduced during which antimony was offered in the reactor. It acts as a surfactant smoothing
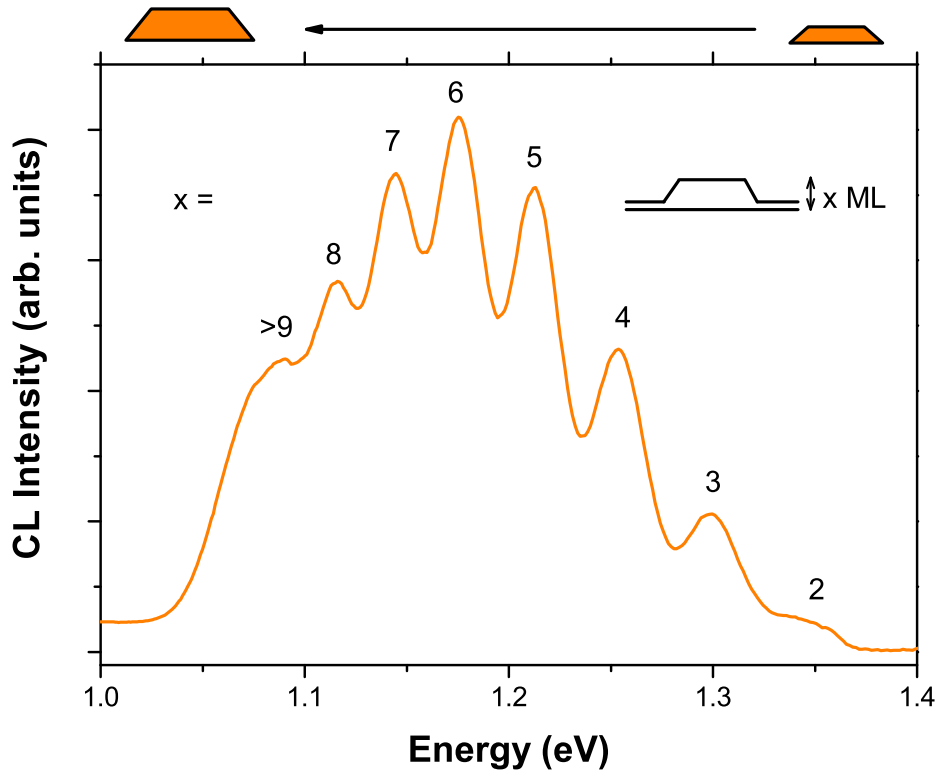

Figure 3.4: Low temperature PL spectrum of sample ML. The prominent oscillation on the spectrum is due to a multimodal QD distribution into distinct subensembles described in the text. The numbers give the height of the QDs in the corresponding subensemble in full InAs monolayers.

the interface between QDs and cap layer. No evidence of incorporation of Sb atoms was found [90]. During the growth interruption the QDs undergo an evolution (see also description of sample GI on page 46). QD seeds with a fixed base length in their early stage of development evolve into QDs with a fixed height [91]. Thus, self-similar QD subensembles form with an onion-like structure [90] resulting in the spectrum shown in Fig. 3.4. Every peak in the spectrum originates from such a subensemble of QDs with a fixed height. The peaks can be numbered consecutively according to the height in monolayers of the QDs in the corresponding subensemble starting with 2 for the smallest QDs on the high energy side to >9 on the low energy side.

Such a distinct QD size distribution is very valuable for single-QD spectroscopy. Due to the self-similarity of the QDs a direct link exists between QD height and luminescence energy. In order to analyze the dependence of electronic properties on QD height one has to merely compare spectra of QDs at different energies. Additionally, the ensemble spectrum covers a broad range of energies granting access to QDs of very different heights.

The QD density in this sample is, however, larger than 10^{10} per cm^2 which requires the application of shadow masks for single-QD spectroscopy (see Sec. 3.3).

3.2.2 Low-Density Quantum Dots

In order to facilitate the isolation of spectra of single QDs (see Sec. 3.3) it is favorable to grow samples with low QD densities. This issue is very complicated and requires good control over the growth parameters, as the parameter window between no QDs at all and densities larger than 10^9 QDs per cm^2 is very narrow.

One possibility is switching off the rotation of the wafer during growth of the QD layer as has been done during the growth of **sample NR**. Normally, the wafer rotates in the reactor in order to provide similar growth conditions over the whole wafer resulting in homogeneous growth of the sample. By switching off this rotation the growth conditions become very inhomogeneous resulting in a gradient of the QD density over the wafer ranging from 0 to >10^{10} QDs per cm^2. This produces an area on the wafer where the QD density is low enough for single-QD spectroscopy. Usually this gradient is very steep. This implies that the area with suitable QD densities is very small, on the order of a few 100 μm. The SEM, however, can accurately position the electron beam within this area thus allowing single-QD measurements. Since the QD density is so low in the area of interest no PL ensemble spectrum can be recorded for sample NR. The main aspect of this growth mode simultaneously constitutes its main disadvantage: the inhomogeneous growth conditions over the sample. Self-similarity as obtained in sample ML is hence not achieved here. Additionally, the range of QD
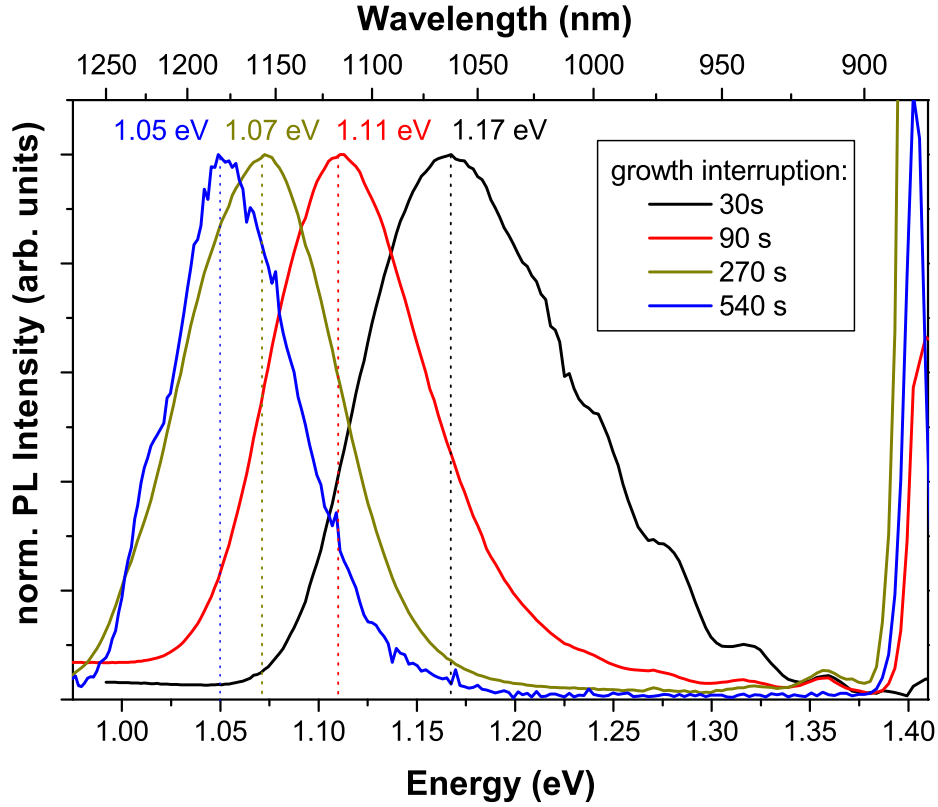
Figure 3.5: Ripening effect of QDs. The growth conditions for all four samples shown were identical except for the duration of a growth interruption after deposition of the QD material. The longer this interruption the lower the emission energy of the ensemble peak alluding to larger QDs. The sample with 540 s growth interruption corresponds to sample GI in the text.

emission wavelengths is limited to < 980 nm.

Another possibility is based on in-situ ripening of the QDs [90]. Immediately after QD material deposition a growth interruption is introduced in order to give the QDs time to build. Shortly after deposition a large number of small QDs is present on the sample. Then a material transfer is initiated where larger QDs gain in size at the expense of smaller QDs. Deposition of the cap layer immediately stops this process: the current size distribution is fixed. Consequently, the longer the growth interruption, the fewer small QDs are present since they either dissolve or grow to become larger QDs. This leads to an overall redshift of the QD ensemble peak due to the quantum size effect. This process is illustrated in Fig. 3.5 where the ensemble PL of QD samples with different growth interruptions is shown. Note, that the ripening process is apparently not finished after as much as 540 s although it slows down considerably with respect to shorter times.

In **sample GI** the growth interruption was 540 s. Then, only very few small QDs remain. In the spectral range between 1.2 and 1.35 eV the density is now small enough
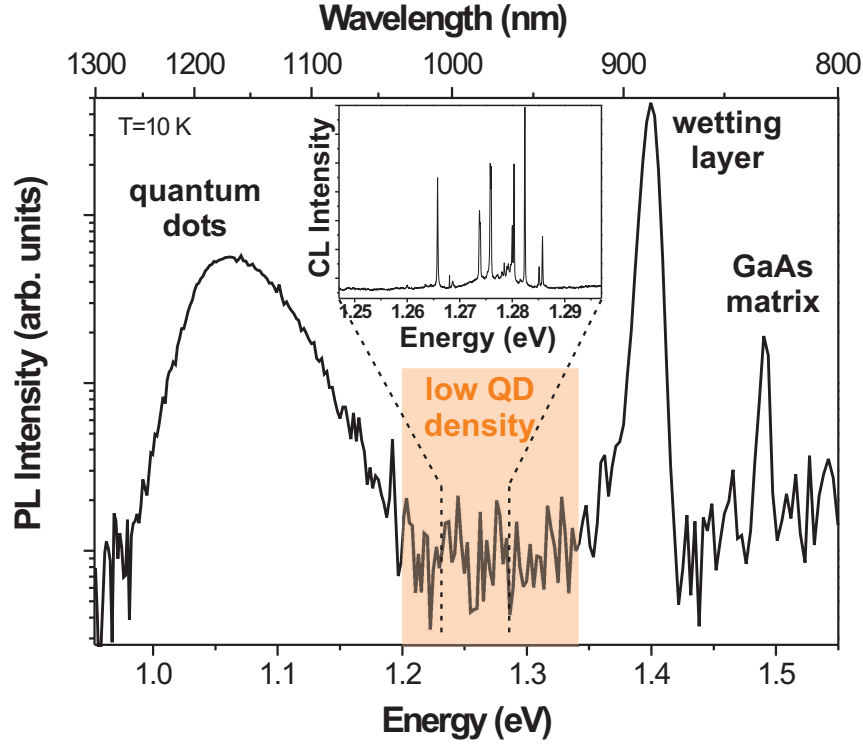
Figure 3.6: Low temperature spectrum of sample GI. The orange box indicates the spectral range where single-QD spectroscopy is possible. A sample spectrum of a single QD is given in the inset.

to perform single-QD spectroscopy (see Fig. 3.6). Note, that the actual QD density is still high. But since the few remaining small QDs are spectrally separated from the mass of the larger ones, they are now easily accessible with CL mapping (Fig. 3.7).

3.3   Probing single Quantum Dots

Isolating QDs from a larger ensemble for single-QD spectroscopy is very challenging. Generally, three different techniques are used.

The most simple one is examining a sample where the QD density is low enough that only one QD is excited at a time [Fig. 3.8 (a)]. This of course requires accurate growth control as outlined in Sec. 3.2.2. A good example of a sample with low enough QD density is shown in Fig. 3.7. Here, a CL map of sample GI is shown that illustrates the possibility of isolating the QD spectra without further ado.

If the QD density is too high, metal shadow masks can be applied [92] [Fig. 3.8 (b)]. Here, it consists of a 70 nm thick film of metal with circular nano apertures with 100 or 200 nm in diameter. They are produced by applying a solution with polystyrene spheres with the desired diameter onto the sample surface. After evaporation of the solvent the nano spheres remain and metal of the desired thickness is applied onto
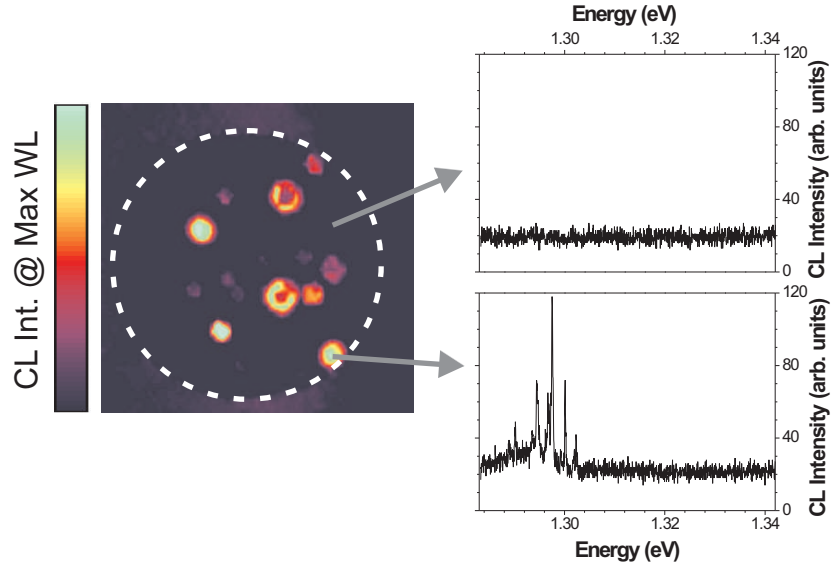
Figure 3.7: Left: Color-coded CL map of the intensity at the wavelength of maximum intensity of sample GI in the energy range 1.283 – 1.342 eV. Successful isolation of spectra of different QDs can be seen. Right: Two spectra extracted from the CL map from the locations indicated by the gray arrows.

the sample by thermal evaporation. In a last step the spheres are removed from the sample in an ultra-sonic bath in an appropriate solution (here: ethyl acetate). The metal is chosen such that the absorption coefficient is as high as possible at the QDs' emission wavelength and such that the film sticks to the sample even in the ultra-sonic bath. Au in combination with 10 nm of Ni as adhesive has proven to produce the desired results for GaAs-based material. A critical downfall of this technique is the fact that in order to supply sufficient spatial resolution the apertures have to be much smaller than the emission wavelength of the QDs. Consequently, the light has to tunnel through the apertures which leads to a severe cut-down in light intensity. This technique requires that the apertures are in the so-called *near field* of the QDs.
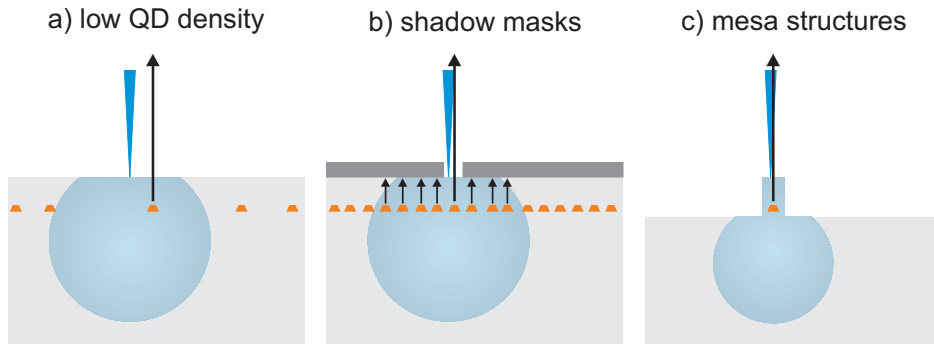

Figure 3.8: Schematics of three different techniques to probe single QDs.
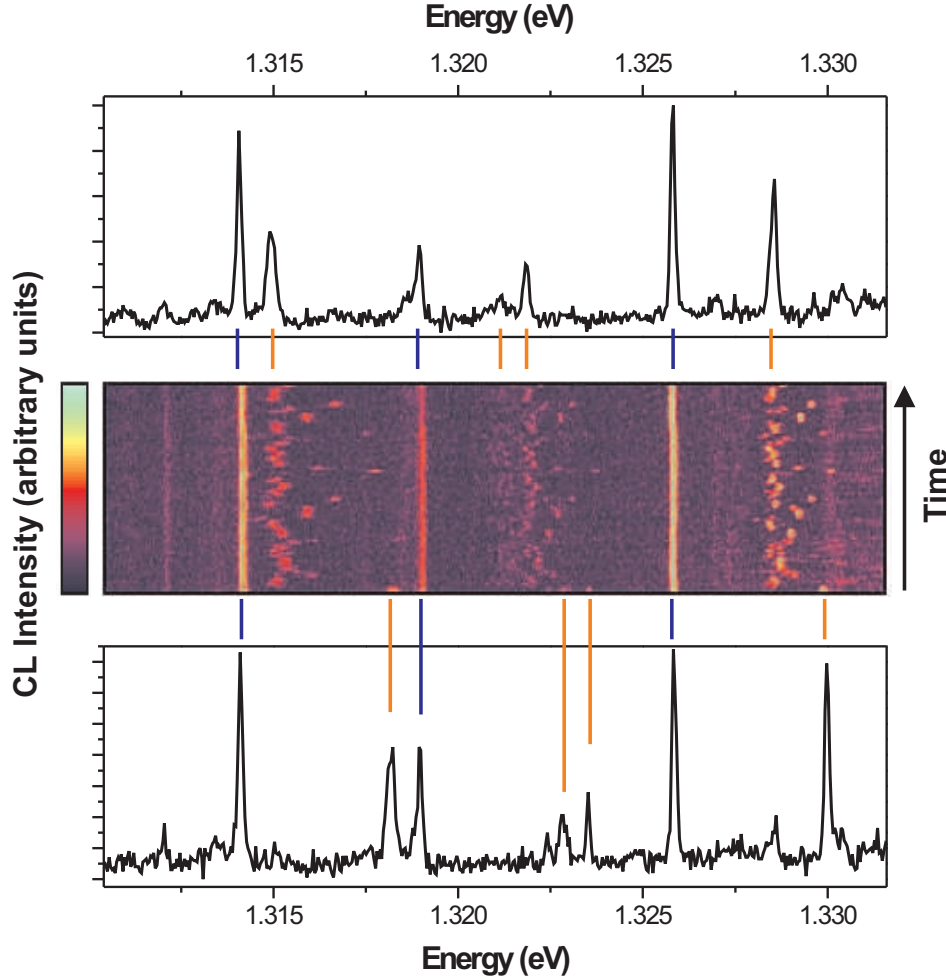
Figure 3.9: Spectral diffusion patterns of two QDs of sample ML. The time series shows a total of 40 s. The upper (lower) panel shows the last (first) spectrum recorded. QD spectra can be identified according to their jitter pattern (blue and orange lines).

R. D. Grober and coworkers estimated that the near field of the aperture has an extent on the order of the aperture's diameter [93]. This implies that the QDs must not be covered by more than 200 nm of capping material. Otherwise the amount of light coupled through the nano-apertures out of the sample is not enough for single-QD spectroscopy.

For the sake of completeness, a last possibility to probe single QDs shall also be mentioned although it has not been used in this work. It is possible to etch mesa structures into the sample and thus isolating the QDs themselves rather than the light they emit [see Fig. 3.8(c)]. The mesas have to be on the order of a few 100 nm which makes them very hard to process. Additionally, the possible influence of surface states has to be taken into account.

Oftentimes the QD density is too high to completely isolate the spectra of a single QD and light from a few QDs is detected simultaneously even when shadow masks are

used. However, if the density of the QD emission lines is low enough, the Quantum Confined Stark Effect (QCSE) helps to identify those lines that originate from the same QD. The QCSE leads to an alteration of the QD emission energies under the presence of electric fields (see Sec. 2.3). This effect is best visualized when time series of spectra are recorded. An example of such a time series is given in Fig. 3.9. The central part of the figure shows the time series. The CL intensity is given on a linear color scale. The top panel shows the last spectrum of the time series, the bottom panel show the first recorded spectrum. Without the information of the time series no correlation of the lines is possible and thus no analysis of spectra of a single QD can be made. Even the number of QDs that emit the measured lines is unknown. In the given time series, however, two generally different behaviors of the lines can clearly be identified. One group (blue connection lines) shows relatively constant emission energies, while a second group (orange connection lines) changes its spectral position randomly in the course of 40 s. The total amplitude of the jitter in this example is >3 meV. Since the jitter pattern is unique to every local environment of the QDs one can thus conclude that Fig. 3.9 shows the spectra of two different QDs. This way it is possible to analyze QD spectra even if more than one QD is probed simultaneously.

The jitter, also called spectral diffusion, depends on a vast number of parameters. Of course it depends on the sample itself and its structural quality, i.e. defect density and type of defects. But even QDs in the very same sample and of comparable size (and therefore emission energy) show extremely different patterns (which is why it is so helpful here). This indicates that the local electronic environment of the QDs in one sample can be extremely different. Its first observation was made by S. A. Empedocles and coworkers on colloidal CdSe QDs [94]. Since then this effect has been observed in a number of different self-assembled QD systems such as CdSe/ZnSe [17], InP/GaP [95], InAlAs/AlGaAs [96] and InGaN/GaN [18] just to mention a few.

Additionally, the excitation method plays a role. It has been shown, that the same QD that showed a pronounced jitter when excited with the electron beam of the cathodoluminescence showed no jitter at all when excited with the laser of a μPL setup [97]. It seems that the excess energy of the electrons plays an important role in charging and discharging the interface or defect states.

Isolating the spectra of single QDs is still a demanding challenge. This challenge is met, however, with a combination of growth and processing control and the exploitation of the QCSE thus making the analysis of the electronic properties of single QDs via optical spectroscopy possible.

Chapter 4

Results

This chapter presents the experimental results and therefore constitutes the main part of this work. In the first section the quantum dot (QD) spectra will be decoded step by step ultimately assigning each transition line to the decay of a specific excitonic complex. The second part of the chapter describes in how far the electronic properties change with varying QD size. Special attention will be given to the fine structure of the excitonic complexes and its manifestation in the spectra. A comparison to the theory derived in Chap. 2 will be given where appropriate. Then a way for targeted manipulation of the electronic structure of the QDs by thermal annealing is introduced. In the last section results of time-resolved measurements will be reported and a connection to the fine structure will be established.

4.1 Decoding Single-Quantum-Dot spectra

As discussed in Chap. 2 different excitonic complexes comprised of a different number of charge carriers exist in QDs, such as excitons (X), biexcitons (XX), charged excitons or trions (X^+, X^-), and even charged biexcitons (XX^+, XX^-). Due to the different occurring Coulomb interaction terms the transition lines in a spectrum originating from the recombination of an electron-hole pair in two different complexes will differ in energy. Since carrier capture into the QDs is a statistical process and the electron [98] and hole [99] capture times are on the order of picoseconds and the recombination times are on the order of nanoseconds, a spectrum recorded over the period of several 100 ms can comprise transition lines from different excitonic complexes simultaneously. Figure 4.1 shows a spectrum of a single QD from sample GI as an example, displaying nine emission lines numbered 1 through 9. Most of these lines occur in all single-QD spectra recorded in this work. This systematic behavior together with excitation-dependent and polarization-dependent measurements enable the unambiguous assignment of the
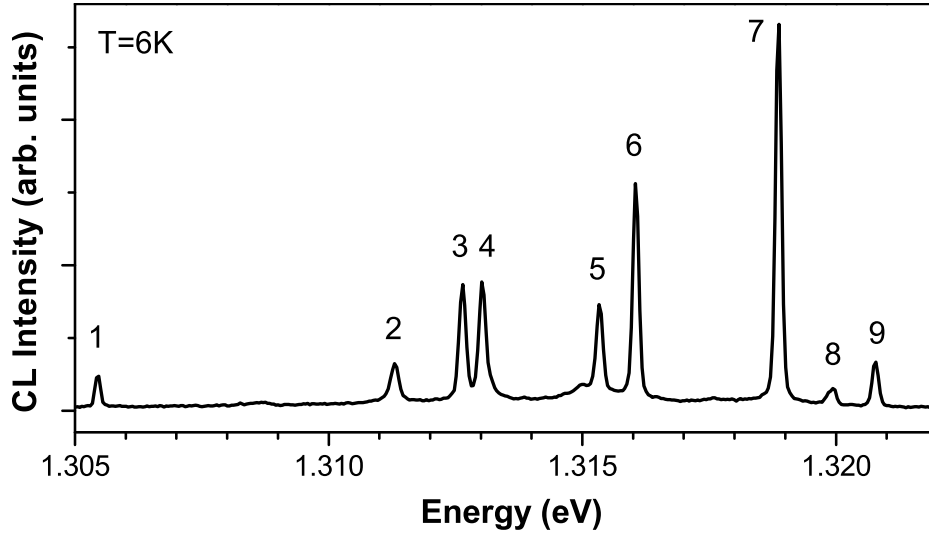
Figure 4.1: Spectrum of a single quantum dot from sample GI displaying nine different emission lines stemming from different excitonic complexes.

lines to the decay of specific excitonic complexes.

For an accurate analysis of the single-QD spectra it is essential to be able to change the excitation density. Other than in all-optical systems the application of optical filters is not possible in cathodoluminescence. One can, in principle, alter the beam current of the electron beam in order to change the excitation density. However, this is not possible over a wide enough range to obtain all excitation regimes necessary to identify all excitonic complexes. Additionally, a change of the beam current requires careful readjustment of the magnetic lenses to achieve a good SEM image rendering this technique time consuming and therefore not practical. Instead, a faster method has been applied here.

By moving the electron beam away from the center of the QD fewer electron hole pairs reach the QD via carrier diffusion. This is equivalent to reducing the local excitation density in the QD's proximity. Thus, by varying the distance between electron beam and QD center the excitation can be varied continuously. Although this approach is more qualitative than the application of optical filters in micro-photoluminescence it is sufficient to obtain the different excitation regimes needed for the identification procedure.

While moving the electron beam away or towards the QD and thus altering the local excitation density every some 100 ms[1] a spectrum is recorded. The spectra are then reassembled and yield time series (similar to the jitter time series in Fig. 3.9) with varying excitation densities. The time series corresponding to the spectrum shown in Fig. 4.1 is given in Fig. 4.2. It is evident that some lines have noticeable intensity at

---

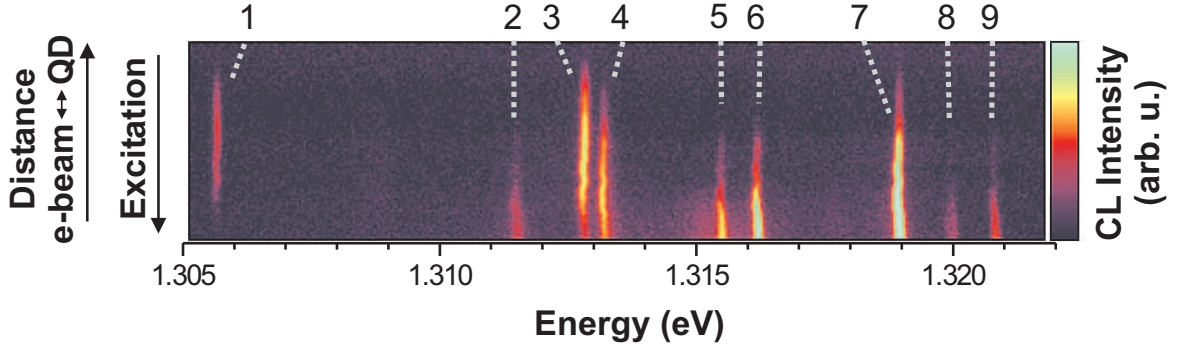[1]depending on the intensity of the lines

Figure 4.2: Color-coded spectra in a time series with varying excitation. The excitation density increases from top to bottom. Clearly, some lines appear at weaker excitation than others indicating that they originate from lower excitonic complexes.

lower excitation densities than others. In this specific example the three lines appearing at the lowest excitation densities are lines 1, 3, and 7. Since at these excitation densities only few charge carriers reach the QD, the lines originate from the lowest excitonic complexes possible, i.e. X, X^-, and X^+. We know from theoretical considerations of the magnitude of the Coulomb interaction terms that the X^- should be on the low energy side of the X and the X^+ on the high energy side (see Sec. 2.2.1). Furthermore, a slight positive background doping is present in all examined samples that leads to more prominent positively charged complexes. We therefore conclude that line 1 originates from the X^-, line 3 from the X and line 7 from the X^+. This assignment will be confirmed by polarization-dependent measurements (see below).

The next line appearing in Fig. 4.2 is line 4. The next higher excitonic complex to be considered consisting of four charge carriers is the XX. Indeed, the XX will turn out to be the origin of line 4. Again this will be proven by polarization-dependent measurements.

We are left with lines 2, 5, 6, 8, and 9. The lines appear at yet higher excitation densities and thus belong to more complicated complexes. The considerations of Sec. 2.2.5 and 2.2.6 together with the polarization-dependent measurements will allow the identification of the corresponding complexes.

If a linear polarizer foil is introduced into the optical detection path and aligned along the [110] and [1$\bar{1}$0] crystal direction, respectively, some of the lines in Fig. 4.1 show a prominent fine structure. Figure 4.3 illustrates this situation.[2]

We know from Chap. 2 that exchange interaction leads to a fine structure of different transitions. We make use of this fact here, to further identify the transitions.

---

[2]Figure 4.3 shows a spectrum of a different QD from sample GI simply because the features to be discussed are more prominent in this example. All features are also present in the spectrum in Fig. 4.1 when using the linear analyzer.
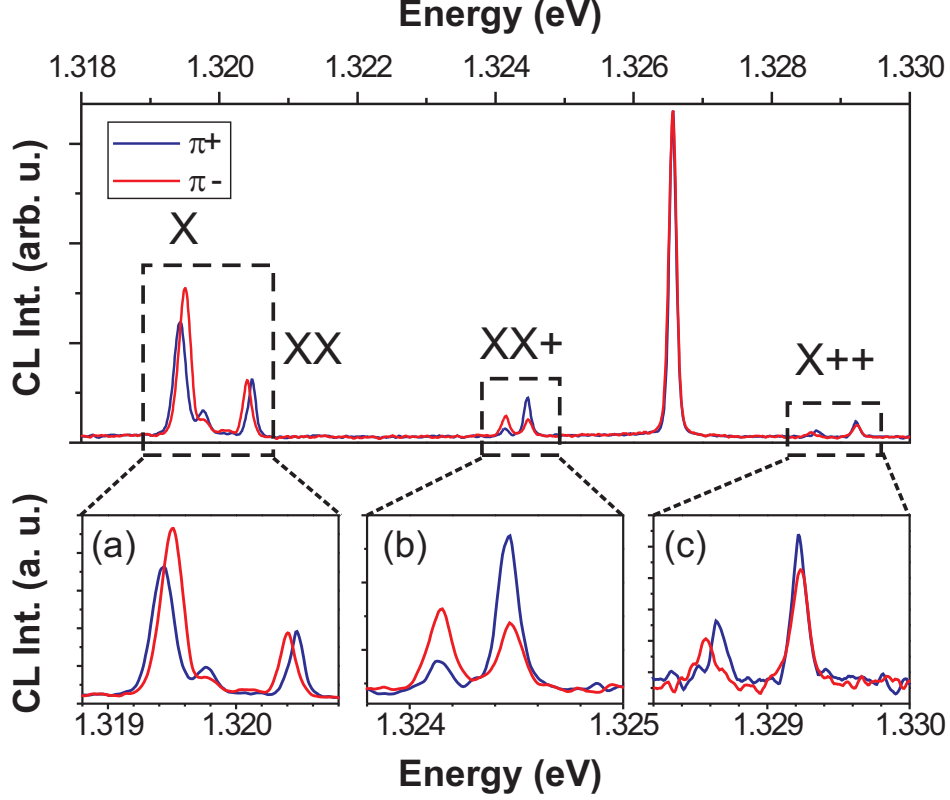
Figure 4.3: Polarization-dependent spectrum of a single QD taken for two orthogonal crystal directions ($\pi+ = [110]$, $\pi- = [1\bar{1}0]$). The fine structure of X, XX, XX$^+$ and X^{++} is magnified in the lower panels. a) Excitonic fine-structure splitting in the X and XX emission. b) Two elliptically polarized XX$^+$ emission lines. c) Two X^{++} emission lines, one of them showing an exciton-like splitting.

The strong resonance at 1.3265 eV in Fig. 4.3 shows no polarization. This line corresponds to line 7 in Fig. 4.1 that was tentatively assigned to the X$^+$ decay. Indeed the X$^+$ should show no fine structure due to the Kramers degeneracy (see Sec. 2.2.5) The same is true for the X$^-$ line (not shown in Fig. 4.3).

In Fig. 4.3 (a) the two lines that we have already identified as originating from X and XX are shown (corresponding to lines 3 and 4 in Fig. 4.1). The cross-polarized doublet structure of the lines predicted in Sec. 2.2.3 Fig. 2.8 is well visible, thus confirming their excitonic/biexcitonic origin.

Figure 4.3 (b) shows the polarization behavior of lines corresponding to lines 5 and 6 from Fig. 4.1. It reproduces exactly what we expect from the XX$^+$ decay [see Fig. 2.10 (c) lines 1 and 2]: an elliptically polarized doublet structure. This, together with its energetic position[3] and the systematics with which doublets of this kind were found in a large number of QD spectra, pinpoints the two lines as XX$^+$ transitions.

---

[3]with the same argumentation as for X and X$^+$ the XX$^+$ is always expected on the higher energy side of the XX.

Figure 4.3 (c) shows the polarization behavior of lines 8 and 9 from Fig. 4.2. Here, the fine structure as expected from the decay of the doubly positively charged exciton (X^{++}) is reproduced [see Fig. 2.12 (c) lines 1 and 2]: one doublet on the lower energy side and one singlet with double intensity on the high energy side. Again, the energetic position and systematics identify these lines as the X^{++} transition.

For both, the XX^+ and the X^{++}, an additional singlet transition is expected to appear in the spectra (see Figs. 2.10 and 2.12). This transition, however, has not been observed throughout this work[4]. Other experiments in the literature that examined charged complexes confirm that this transition is either not or only weakly visible in the emission spectra. I. A. Akimov and coworkers intensively examined the electronic structure of the XX^- in CdSe QDs and saw no sign of the singlet transition although their signal to noise ratio was very high [74]. B. Urbaszek and coworkers examined negatively charged complexes in single InAs QDs [100]. They saw no sign for the singlet transition for the XX^- and a weak singlet transition for the X^{--} which was about 20 times weaker than the triplet transitions. Finally, N. I. Cade and coworkers examined large InAs QDs emitting around 0.94 eV and they also saw no singlet transitions for the XX^-, XX^+, and X^{++} [101]. One possible explanation for the absence of this transition is fast relaxation of the singlet $|0\rangle_S$ into the triplet $|0\rangle_T$ state. Due to the Heisenberg uncertainty principle fast relaxation implies a large energetic broadening. In the emission spectrum the transition line would therefore be very broad and disappear in the noise level.

Very recently M. Ediger and coworkers published a spectrum where they attributed the X^{++} singlet transition to a line in their spectrum which has equal intensity as the triplet transitions [77]. However, results of only one QD were reported and the splitting of the line, that would confirm their identification, was close to their experimental precision.

The analysis described above makes it possible to identify a large number of excitonic complexes in the spectra. Figure 4.4 shows the sample spectrum discussed so far with labels for X, X^+, X^-, XX, XX^+ and X^{++}.

Especially under high-excitation conditions some spectra show lines that can not be unambiguously identified. One such example is line 2 in Fig. 4.1. The energetic position hints towards a resonance from the XX^- decay. The XX^+ singlet transition discussed above is unlikely as origin since the line appears at considerably higher excitation densities than the other XX^+ resonances (see Fig. 4.2). Another example are weak lines sometimes appearing at the low energy side of the X^- which could be

---

[4]The singlet transition may be visible in some spectra where unidentified lines are present. However, the lack of any systematics made a definite identification impossible.
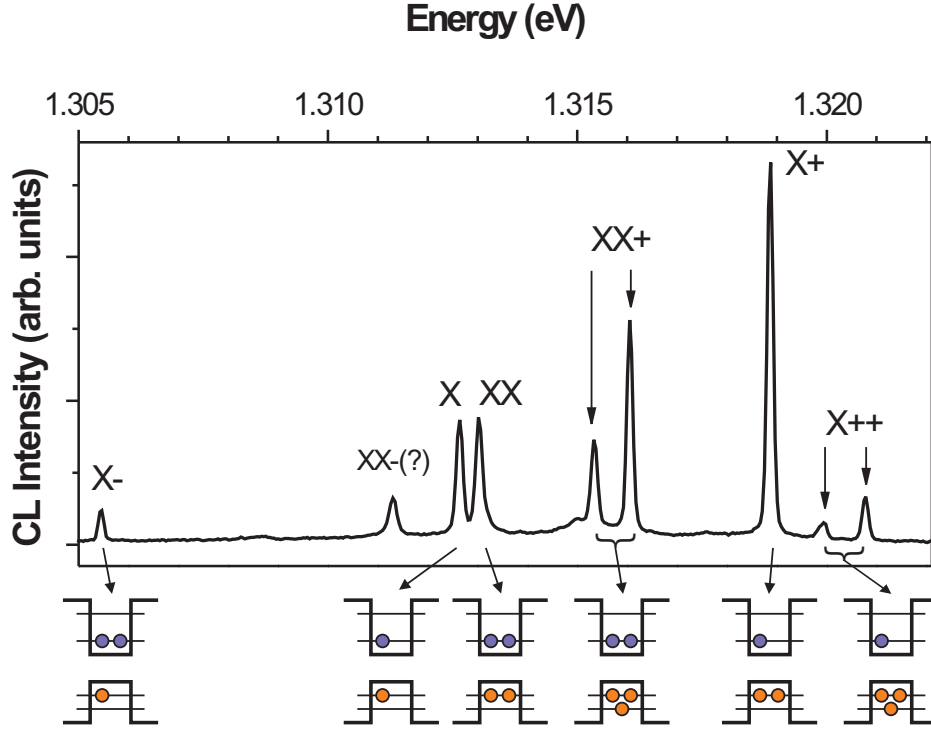
Figure 4.4: single-QD spectrum from Fig. 4.1 with the origin of the lines shown. The sketches on the lower side show the configuration of the charge carriers in the QD for the respective excitonic complex.

due to the X^{--} decay. However, the appearance of all these lines is rare and they are usually too weak to reliably analyze their fine structure. This makes the identification of such lines speculative. They have therefore not been further considered in this work.

4.2   Structural vs. Electronic Properties

For targeted growth of single QDs for applications it is important to understand the way structural changes of a QD will influence its electronic structure. Some simple connections are well established by now. The larger the QD (at otherwise constant parameters) for example, the lower its transition energy. This is known as the quantum size effect [1]. Another slightly more complicated connection exists between strain and transition energy. Hydrostatic strain increases the energy of both conduction and valence band. However, the conduction band is much more sensitive to this effect. This means that the higher the hydrostatic strain inside the QD the higher the transition energy [51]. This effect has also been exploited technologically by introducing strain reducing layers into the structure in order to push the luminescence wavelength of InAs QDs towards 1.3 [102] and 1.5 μm [103].

Here, more subtle effects will be investigated that gain more and more importance

since devices based on single QDs such as single-photon emitters have moved more into focus. We will discuss in how far QD size and symmetry affect binding energies and the fine structure of excitonic complexes. This is possible by applying the identification procedure described in Sec. 4.1 to a large number of single-QD spectra and systematically analyzing their differences and similarities.

4.2.1 Excitonic Binding Energies

We have concluded from a simple comparison of effective masses that adding an electron (a hole) to an excitonic complex should in general shift the transition to lower (higher) energies (see Sec. 2.2.1). The exact numerical value of the binding energies, however, depends on the shape of the wave functions and the resulting overlap and therefore the exact QD morphology. In particular, the dependence of the binding energies on the QD size will be analyzed in the following.

Sample ML is very suitable for this kind of analysis since the self-similarity of the QDs from different subensembles guarantees a straight forward interrelation between QD size and transition energy (see Sec. 3.2.1). Figure 4.5 shows the binding energies of X^-, X^+, XX, and both components of XX^+ with respect to the exciton transition energy for 111 QDs and the theoretical predictions made by eight-band $\mathbf{k \cdot p}$ theory and configuration interaction for X^-, X^+, and XX (from Ref. [58]). The QD structures that enter the theoretical model have been chosen to fit ensemble PLE spectra [104] and TEM measurements. This analysis is the continuation of the work by S. Rodt and coworkers [16] who examined the same sample but were restricted to the energy region above 1.2 eV due to the lack of a suitable detector for longer wavelengths. This limitation has been overcome with the acquisition of an InGaAs diode array that complements the Si CCD camera and thus enables the examination of the binding energies over the whole ensemble PL peak from 1.05 to 1.35 eV.

Several observations can be made in Fig. 4.5.

1. The rule that adding one electron (hole) to a complex shifts the transition energy to lower (higher) energies is universal for QDs in this sample with one exception on the very low energy side, where the X^+ is at lower energy than the X.

2. All binding energies show a clear dependence on exciton energy and hence QD height. The X^- seems to play a special role since the QD size effect on its binding energy is much smaller than for all other complexes. Additionally, its binding energy decreases for lower exciton energies contrary to the other complexes.

    The binding energy of the X^- is governed only by electron-electron and electron-
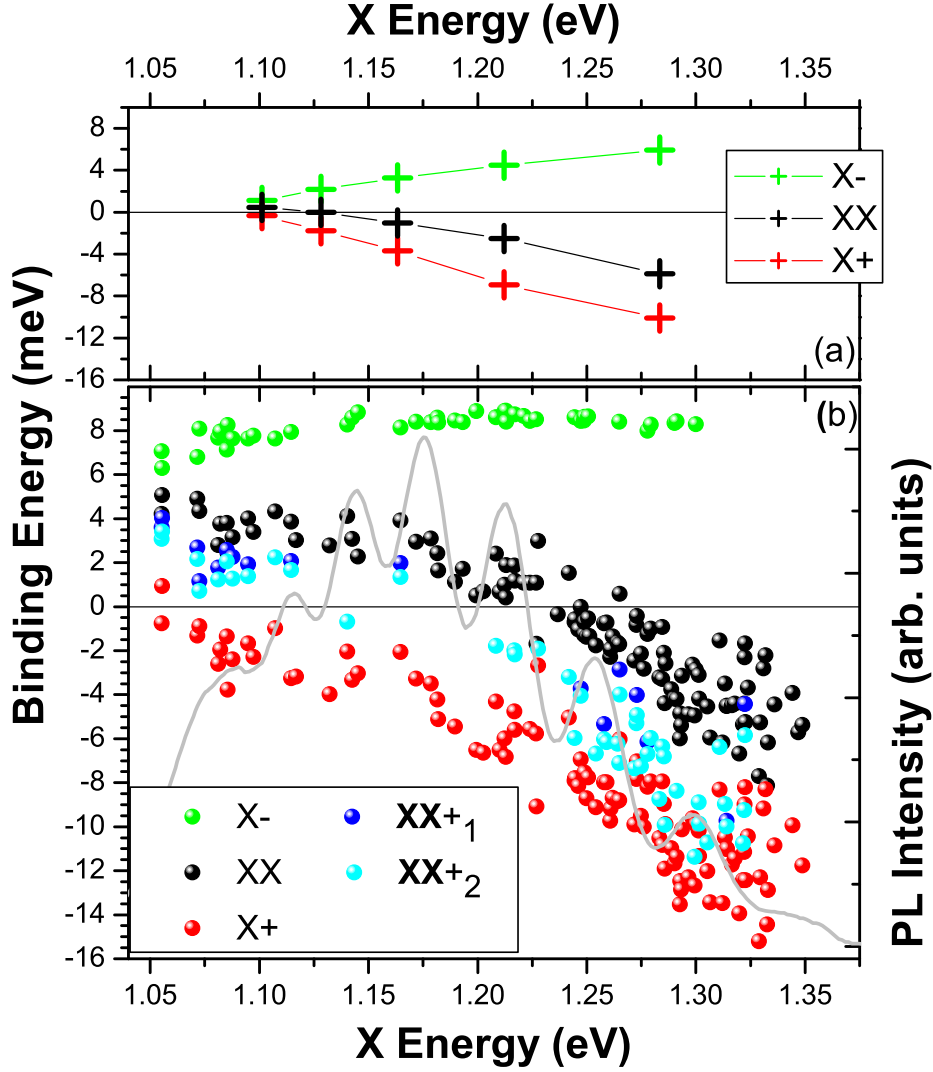
Figure 4.5: a) Theoretical values for the binding energies of X^-, XX, and X^+ with respect to the X versus the X recombination energy as obtained from CI calculations. b) Experimental values for binding energies of four different excitonic complexes. A clear dependence can be seen resulting from changing wave function shape and thus Coulomb energies between the participating charge carriers (see text). The gray line illustrates the ensemble PL spectrum.

hole Coulomb energies[5]. All other binding energies also contain hole-hole Coulomb energies. We can thus conclude, that the hole-hole Coulomb energy drastically changes with QD height relative to the other two terms. Since the hole wave functions are strongly confined in the QD due to their large effective mass they react sensitively on the QD's structure. The electron on the other hand is spread out into the matrix and is comparatively independent of the QD structure. This explains the strong dependence of the hole-hole Coulomb terms on QD height.

---

[5]since $E_{bind}^{X^-} = -C_{ee} - C_{eh}$ (see Eq. 2.11)

3. XX and XX$^+$ change their character from binding to anti-binding with reduced QD height. This is also a consequence of the increasing magnitude of the repulsive hole-hole interaction for smaller QDs. The binding to anti-binding crossovers are at $\approx$1.23 eV and $\approx$1.19 eV for the XX and the XX$^+$, respectively.

4. The energetic spread of the spectra is reduced for larger QDs. This is due to the fact that for larger QDs the hole wave function spreads out becoming more similar to the electron wave function. This leads to a convergence of the Coulomb interaction terms. The limit of this process, i.e. identical electron and hole wave functions with common centers of mass would imply degenerate X, XX, X$^-$, and X$^+$ energies[6] as implied by the theoretical values for the largest QD at 1.10 eV in Fig. 4.5 (a).

complex	E_{bind}^{min}	$E^{min}(X)$	E_{bind}^{max}	$E^{max}(X)$	$E_{bind}^{max} - E_{bind}^{min}$
X$^-$	6.3 meV	1.055 eV	8.9 meV	1.213 eV	2.6 meV
X$^+$	-15.2 meV	1.333 eV	0.9 meV	1.055 eV	16.1 meV
XX	-8.1 meV	1.333 eV	5.1 meV	1.055 eV	13.2 meV
XX$_1^+$	-9.7 meV	1.314 eV	4.0 meV	1.055 eV	13.7 meV
XX$_2^+$	-11.4 meV	1.299 eV	3.4 meV	1.055 eV	14.8 meV

Table 4.1: Summary of the maximum and minimum binding energies for X$^-$, X$^+$, XX, and XX$^+$ relative to the X. The X$^-$ binding energy varies by only 2.6 meV while the others vary by more than 13 meV. The maximal (minimal) binding energy of X$^-$ occurs at low (high) X energies contrary to all other complexes (red numbers).

Table 4.1 summarizes the spread of binding energies found in sample ML for different complexes.

The modeling with eight-band $\mathbf{k} \cdot \mathbf{p}$ theory reproduces the main experimental findings in a very convincing manner [Fig. 4.5(a)]. The general dependence of the binding energies on QD size (increasing with size for XX and X$^+$; decreasing with size for X$^-$) as well as the existence of an XX binding to anti-binding crossover are replicated. Some quantitative agreement is also reached with the theoretical values matching the experimental ones within a factor of 2 or better. Details, however, such as the almost constant X$^-$ binding energy and the energetic position of the XX binding-to-anti-binding crossover deviate from the experiment. This could be owed to the approximations made by eight-band $\mathbf{k} \cdot \mathbf{p}$ (macroscopic permittivity) and configuration interaction (incomplete basis). Additionally, the real QD structure may deviate slightly from the

---

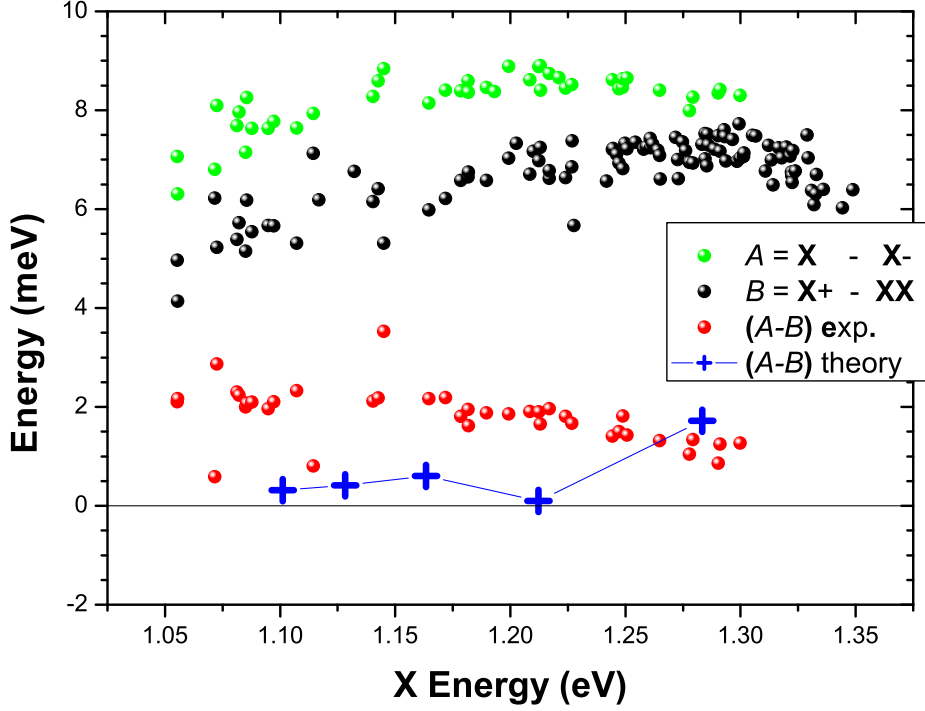[6]disregarding correlation and exchange

Figure 4.6: The energetic difference between the X and X$^-$ transition (A) and the X$^+$ and XX transition (B) as well as their difference ($A - B$) are shown. ($A - B$) gives a measure of the correlation (see text). The blue crosses give the correlation obtained from CI calculations.

model QD used in the calculations. This would have a noticeable impact on the binding energies since they have proven to sensitively depend on the actual structure [59].

As mentioned in Sec. 2.2.1 the simple treatment of the single-particle direct Coulomb interaction terms disregards few-particle effects, i.e. correlation and exchange. It is possible to quantitatively estimate the error made by this assumption with the experimental data gathered in Fig. 4.5.

Figure 4.6 shows the energetic difference between the X and X$^-$ transition (i.e. the X$^-$ binding energy) denoted as A and the difference between the X$^+$ and the XX transition denoted as B as well as their difference ($A - B$). A and B are a measure for the change in Coulomb interaction, when an electron is added to the X and the X$^+$, respectively. In terms of direct Coulomb interaction the X$^-$ binding energy has been given in Chap. 2.2.1, Eq. 2.11:

$$A = E_{bind}^{X^-} = E(X) - [E(X^-) - E(e)] = -C_{ee} - C_{eh}. \tag{4.1}$$

B is the energetic difference between the transition X$^+ \to$ h and XX $\to$ X and accounts to

$$
\begin{aligned}
B = [E(X^+) - E(h)] - [E(XX) - E(X)] \ &= \ [E(e) + 2E(h) + 2C_{eh} + C_{hh} - E(h)] \\
&\quad -\{2E(e) + 2E(h) + 4C_{eh} + C_{hh} + C_{ee}
\end{aligned}
$$

$$-[E(e) + E(h) + C_{eh}]\}$$
$$= -C_{ee} - C_{eh}. \tag{4.2}$$

Comparing Eqs. 4.1 and 4.2 shows that A and B are composed of the same direct Coulomb energy terms C_{ee} and C_{eh}. Consequently, the difference between the two, illustrated by the red symbols in Fig. 4.6, gives the error made by neglecting correlation and exchange.

Exchange interaction exclusively enters the energetic balance in the form of the dark-bright splitting Δ_0 of the exciton ground state since both trion and XX ground states are fully degenerate (see Sec. 2.2). It increases the measured value of the X recombination energy by $\Delta_0/2$ with respect to the "real" value, i.e. the one that would be obtained when measuring the energetic center of the dark and bright exciton states. This means that both A and B are increased by the same amount $\Delta_0/2$ via E(X) (Eqs. 4.1 and 4.2) and thus, when considering $(A - B)$ the effects cancel each other out. In other words, exchange has no effect on $(A - B)$.

Consequently, the parameter $(A - B)$ is solely a result of correlation. We will now calculate, which correlation terms compose A and B in order to compare experiment and theory. We define the change due to correlation δ_{corr} by

$$E(X) = E(e) + E(h) + C_{eh} + \delta_{corr}(X) \tag{4.3}$$
$$E(XX) = 2E(e) + 2E(h) + C_{ee} + 4C_{eh} + C_{hh} + \delta_{corr}(XX) \tag{4.4}$$

and analogously for the trions. Note that the change due to correlation always leads to a lowering of the total energy. Hence all $\delta_{corr} < 0$.

We know that in $(A - B)$ all single particle energies and all direct Coulomb terms amount to zero. Only the correlation terms remain. From Eqs. 4.1 and 4.2 and noting that $\delta_{corr}(e) = \delta_{corr}(h) = 0$ we obtain

$$(A - B) = \delta_{corr}(X) - \delta_{corr}(X^-) - \delta_{corr}(X^+) + \delta_{corr}(XX) - \delta_{corr}(X)$$
$$= \delta_{corr}(XX) - \delta_{corr}(X^-) - \delta_{corr}(X^+) \tag{4.5}$$

This balance of correlation corrections is visualized by $(A - B)$ in Fig. 4.6. Its magnitude varies only slightly between 1 and 2 meV over the whole energy range. This confirms the conclusion that the change in binding energies in Fig. 4.5 is predominantly due to a change in direct Coulomb terms. For the absolute values, however, the correlation terms are important as they can be close to the same order of magnitude as the total binding energies.

In [58] the correlation terms have been explicitly calculated for the QDs shown in Fig. 4.5 (a) for X, X$^-$, X$^+$, and XX. It is therefore possible to extract these values[7] and

---

[7]The values have been updated with respect to [58] to account for an inaccuracy in the calculation
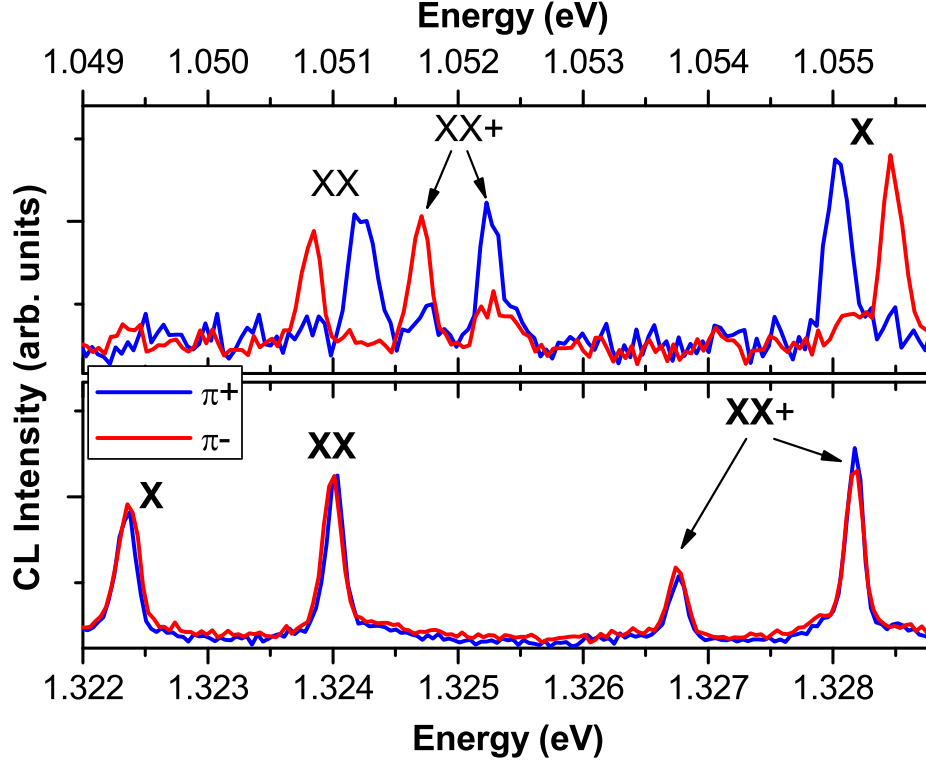
Figure 4.7: Polarization resolved single-QD spectra from sample ML. Upper panel: large QD with low emission energy; lower panel: small QD with large emission energy. The corresponding excitonic complex is given for each line. $\pi+$ is along the $[1\bar{1}0]$ crystal direction, $\pi-$ along the orthogonal $[110]$ crystal direction.

compare them to the experiment analogous to the binding energies. This is visualized by the crosses in Fig. 4.6. The sign of $(A-B)$ is correctly reproduced indicating that the relative strength of the different correlation terms is correct. However, except for very small QDs the correlation correction expressed by $(A-B)$ is underestimated. This suggests that quantitatively correlation in general is not correctly accounted for in the model used.

4.2.2 Fine Structure

In this section the fine structure of the different excitonic complexes will be analyzed. The fine structure is a manifestation of a specific aspect of the quantum mechanical Coulomb interaction resulting from the fermionic character of the charge carriers: the exchange interaction (Sec. 2.2.2).

The theory of this interaction has been studied in detail in Chap. 2. Emission line splittings and polarization behavior have been attributed to isotropic and anisotropic

---

of $\delta_{corr}(XX)$ [105]. The deviation is so small (<0.8 meV), however, that it does not alter the general conclusions here or in [58].
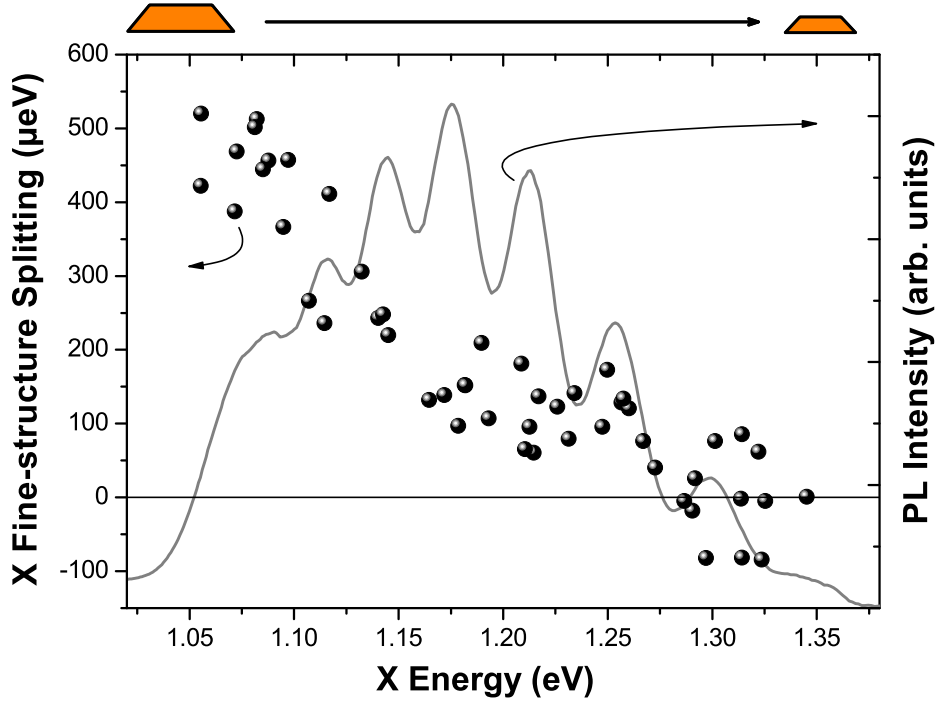
Figure 4.8: FSS values vs. X transition energy for 50 different QDs of sample ML. A clear trend is visible yielding small and even negative FSS values for high energies (small QDs) and large FSS values for low energies (large QDs). The PL ensemble spectrum of the sample is given by the gray line.

exchange effects between confined charge carriers. However, so far only a qualitative analysis has been given that helped with the identification of the emission lines.

The purpose of this section is to analyze the exchange interaction quantitatively and to connect the exchange effects of different excitonic complexes with each other to reveal their common origin.

We will start by focusing on the exciton fine-structure splitting (FSS). Figure 4.7 shows polarization resolved spectra of two QDs of sample ML for small and large transition energies, thus probing a large and a small QD.

We will concentrate on the X and XX transition first since they both give a direct measure of the FSS (see Fig. 2.8). It can clearly be seen, that the QD at small energies shows a large FSS and vice versa. Here, the QD with an exciton transition energy of 1.0553 eV shows a FSS of 420 μeV and the QD with an exciton transition energy of 1.3223 of 20 μeV which is close to the accuracy of the experimental setup.

In order to find out whether the FSS is generally a function of transition energy, spectra of 50 different QDs of sample ML were examined and the FSS extracted. Fig. 4.8 shows the result of this analysis, i.e. the FSS as a function of transition energy.

Indeed, the QDs from this sample show a large FSS at small energies and vice versa with the values varying between -80 μeV to 520 μeV. At very high energies

QDs/matrix	FSS [μeV]	setup	Ref.
InAs/GaAs	-80 – 520	CL	this work
InAs/GaAs	110 – 180	μPL	[22]
InAs/GaAs	≤ 140	μPL	[29]
InAs/GaAs	-30 – 70	μPL	[108]
InAs/GaAs	40	FWM	[26]
InGaAs/GaAs	30 – 150	μPL	[22]
InGaAs/GaAs	10 – 42	transmission	[66]
InGaAs/GaAs	8 – 36	pump & probe	[28]
InGaAs/GaAs	6 – 96	FWM	[65]
InAs/AlGaAs	500 – 1000	μPL	[27]

Table 4.2: Examples of experimental values of the exciton fine-structure splitting (FSS) in In(Ga)As quantum dots. Column 1 gives the material system and column 3 the experimental techniques used (FWM = four-wave mixing).

above 1.3 eV the FSS can even change its sign[8]. This is particularly interesting since it demonstrates the possibility to fabricate QDs with a FSS close to zero. Such a QD could be used as a source for entangled photon pairs [23] for quantum key distribution [106, 107].

A number of different experiments have been conducted in the past in order to resolve the two bright exciton transitions and measure the FSS in different material systems. Table 4.2 gives examples of different values measured by different groups in the (In,Ga)As/(Al,Ga)As system. An FSS of >180 μeV has only been observed when Al was added to the matrix material which increases the barrier height and thus confinement. Stronger confinement leads to a larger overlap of electron and hole thus increasing Coulomb interaction including exchange. No systematic dependence of the FSS on transition energy as in Fig. 4.8 was found with the exception of R. J. Young and coworkers who have observed a variation of the FSS from 70 to -30 μeV in the 1.34 to 1.41 eV energy range for MBE-grown InAs/GaAs QDs [108].

In Chap. 2 it was shown that the FSS originates from the anisotropic part of the exchange interaction. This means it is a function of the symmetry of the confining potential.[9] FSS=0 holds exactly if the confinement symmetry is D_{2d} or C_{4v}. FSS$\neq$0 is a direct consequence if the confinement symmetry is C_{2v} or lower. Its magnitude is,

---

[8]The FSS is defined to be positive when the X line at lower energies is polarized along the [1$\bar{1}$0] crystal direction.

[9]It is important to note that the symmetry to be considered is that of the *overall* confinement potential resulting from QD structure, piezoelectricity, and atomistic effects.
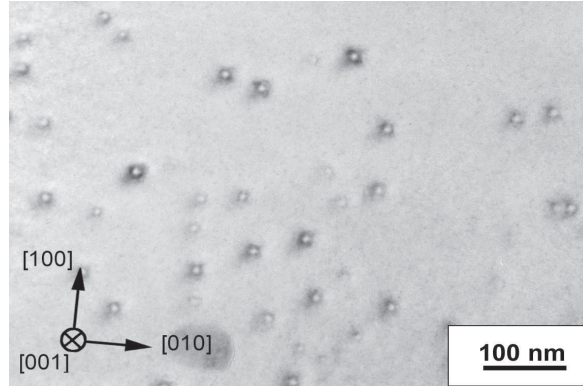
Figure 4.9: Plan view TEM image of a sample similar to sample ML. The QD density is roughly 10^{10} QDs per cm^2. No apparent elongation along a common direction is visible. (Image courtesy of I. Häusler, AG Neumann, HU Berlin.)

so-to-say, a measure for the deviation from C$_{4v}$ or for the degree of anisotropy of the potential in the growth plane.

In principle, three different effects lead to such a symmetry lowering:

Structural elongation of the QD: If the QD itself is elongated into one direction the potential is naturally anisotropic; it aligns to the QD structure. The spectroscopic data on the FSS imply an elongation of the potential into the $[1\bar{1}0]$ crystal direction for most QDs (positive FSS values). In plan view transmission electron microscope (TEM) measurements of similar samples[10], however, no such structural elongation is visible (see Fig. 4.9). Great care has to be taken, however, when interpreting such data, as TEM images visualize the strain field of the sample and not the real structure. Still, a strong elongation above 1.2:1 into any direction can be safely excluded from the images.

Piezoelectricity: Complicated strain fields are generated in the QD structures due to the different lattice constants of QD and matrix material. The shear strain components lead to a separation of the negative and positive charge centers and therefore to piezoelectric fields [51]. These fields have C$_{2v}$ symmetry in the basal plane since the potential minima and maxima form near the corners of the QD pyramid bases which are parallel to the [100] direction [54]. This leads to an anisotropy of the potential along [110] as implied by the spectroscopic data.

Atomistic symmetry anisotropy: Even for perfectly symmetric pyramids opposite interfaces are not completely identical on the atomistic level due to the underlying zinc-blende crystal structure. This leads to different interface potentials [63].

---

[10]No Sb was offered during growth of this sample which leads to a slightly smaller lateral size of the QDs with respect to the ones in sample ML.
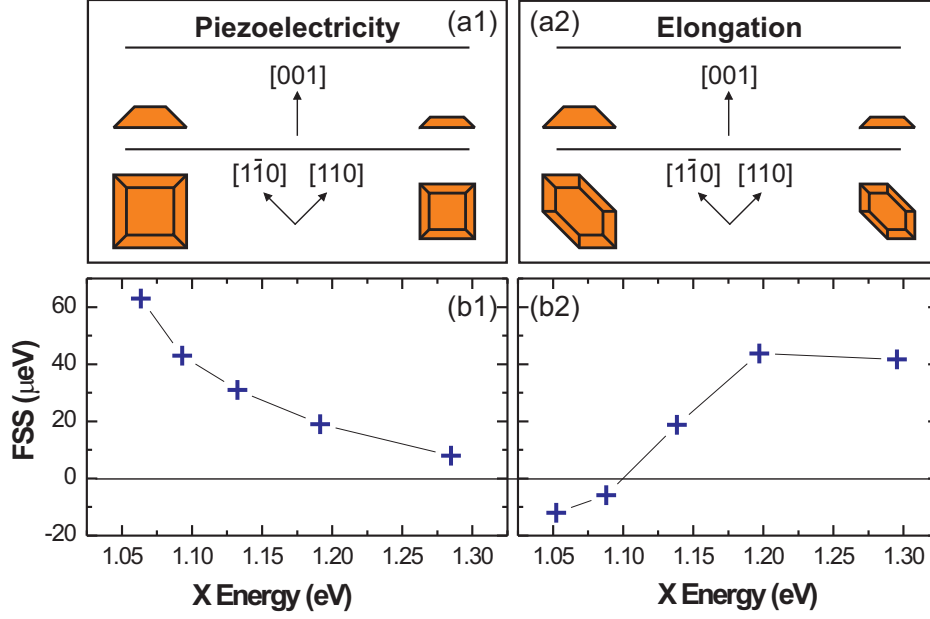

Figure 4.10: Calculated exciton fine-structure splitting (FSS) values for a series of QDs with a square base including piezoelectricity (b1) and a series of QDs elongated in the $[1\bar{1}0]$ crystal direction in absence of piezoelectricity (b2). The structural assumptions of the modeled series are shown in (a1) and (a2).

> This effect is augmented and carried into the QD structure by strain [64]. Since this is an atomistic effect, i.e. it depends on the exact atomic positions, it can not be described by an envelope function theory such as eight-band $\mathbf{k}\cdot\mathbf{p}$. In pseudopotential calculations G. Bester and coworkers have produced FSS values smaller than 10 μeV coming from ASA [63]. This effect has therefore been disregarded in the following discussion.

The essential question is which of these effects increases with QD size and is therefore responsible for the experimentally observed trend.

To distinguish the impact of elongation and piezoelectricity, calculations of the FSS for a series of square-based QDs *including* the effect of piezoelectricity [Fig. 4.10 (a1)] and a complementary series of QDs elongated along $[1\bar{1}0]$ with a lateral aspect ratio of 2 in *absence* of the piezoelectric field [Fig. 4.10 (a2)] have been carried out, despite the fact, that no elongation was noticeable in the TEM images.

To assess the role of piezoelectricity quantitatively, an accurate value of the prime input parameter, the piezoelectric constant e_{14} has to be known. However, as G. Bester et al. pointed out [64], the standard reference for the InAs piezoelectric constant $e_{14} = 0.045$ C/m² [109] can not be considered a trustworthy value for strained InAs QDs. More recent measurements [110, 111, 112, 113] on strained InGaAs quantum wells grown on GaAs(111) substrate suggest an e_{14} value with a negative sign and a

much larger magnitude. Due to the apparent strain dependence of e_{14}, the exact value for strained InAs QDs is unknown. To encounter this problem the values of the most recent work [113] have been extrapolated to obtain the value of strained InAs. As indicated before, the obtained value $e_{14} = -0.385$ C/m^2 has a different sign than the 'standard' value for bulk InAs. However, since there is no direct experimental confirmation for this value, quantitative results of the calculations have to be treated with caution.

Figure 4.10 (b) shows the resulting FSS values for both series. The obtained trend for series 1 (piezoelectricity) is in qualitative accord with the experiment (Fig. 4.8). The relevance of the piezoelectric potential for the FSS stems from its strong dependence on QD height, which has already been shown earlier [54], independent of the chosen value of e_{14}. This explains why the FSS strongly increases with increasing QD size (decreasing exciton energy) [Fig. 4.10 (b1)]. Quantitative agreement however could not be reached (see below). A strong *elongation* of the QDs in the [1$\bar{1}$0] direction by contrast does not reproduce the experimentally observed trend [Fig. 4.10 (b2)]. An elongation in the perpendicular [110] direction (which is equivalent to reflecting the results on the x-axis) also fails. It gives strongly negative FSS values for small QDs and slightly positive values for large QDs. Therefore, elongation can be ruled out as the source of the observed systematic trend of the FSS in the QDs investigated.

It should be pointed out that the exchange interaction was calculated including only monopole terms and only 1st order piezoelectricity. In first calculations the so far omitted dipole terms show a much stronger impact on FSS [105]. This may be the reason why quantitative agreement could not be reached so far in spite of the somewhat speculatively enlarged piezoelectric constant. 2nd order piezoelectricity can also have a strong impact. Under certain circumstances it can even surpass the effects of the first order [60]. It has also been shown to sensitively depend on QD geometry [59] and therefore presents another possible source for the quantitative deviation between theory and experiment.

At this time the question of the physical origin of the symmetry lowering leading to the FSS can not be resolved in full detail. It is a combination of QD structure, piezoelectricity, and ASA. Piezoelectricity seems to be the most promising candidate to account for the strong QD size dependence of the FSS while slight structural elongations and the ASA effect are independent of QD size. For a given QD size they induce a scatter of the observed FSS values. For small QDs, where the influence of piezoelectricity is weak this scatter leads to the observed negative FSS values demonstrating the possibility that in principle QDs with an FSS close to zero exist.

We now examine the XX$^+$ emission. The two transition lines labeled XX$^+$ in Fig. 4.7 show a very different behavior in the two spectra apart from their spectral
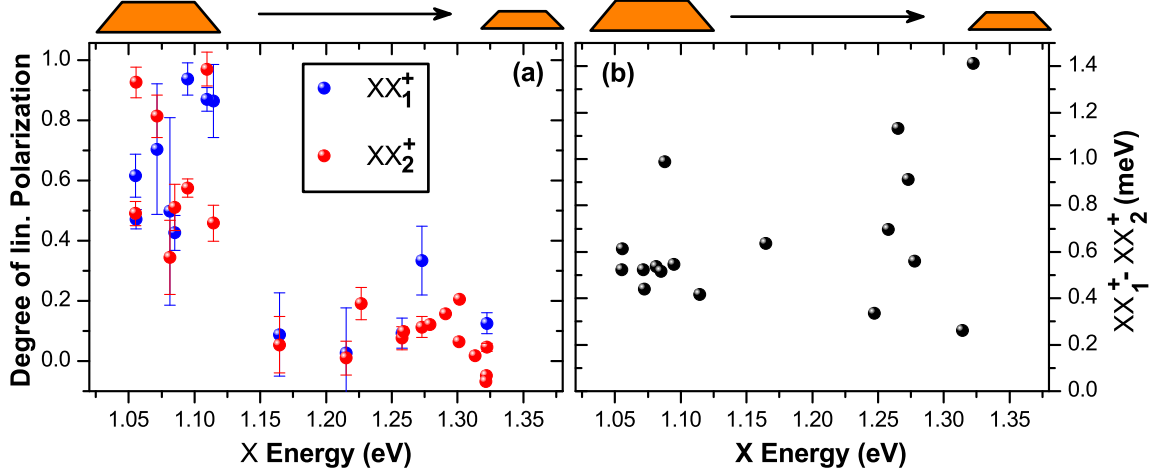
Figure 4.11: Degree of linear polarization (a) of the two XX^+ lines and energetic distance (b) between them vs. X transition energy. The polarization degree is governed by the anisotropic electron-hole exchange interaction and shows a clear trend with strongly elliptically polarized lines for small X energies. The energetic distance is dominated by the hole-hole triplet splitting and shows no noticeable trend with X energy.

position relative to the X which has been analyzed in the previous section. For the small QD at high transition energies the two lines show almost no measurable linear polarization and their energetic difference accounts to 1.4 meV. For the large QD at low energies both lines are strongly elliptically polarized, i.e. their intensity in one polarization direction is much stronger than in the other, orthogonal one. Additionally, their energetic difference is only 0.5 meV. Again, the question is whether these characteristics vary systematically with QD size.

Figure 4.11 shows both linear polarization degree p and energetic distance between both XX^+ lines vs. the X transition energy. p has been calculated from the line intensities using

$$p = \pm \frac{I_{\pi-} - I_{\pi+}}{I_{\pi-} + I_{\pi+}} \qquad (4.6)$$

for XX_1^+ $(+)$ and XX_2^+ $(-)$, respectively. p turns out to be QD-size dependent analogous to the exciton FSS [Fig. 4.11(a)]. We remind ourselves, that the larger p the stronger the final triplet X^{+*} states intermix. This intermixing, in turn, is a function of the anisotropic exchange parameter Δ_1 (see Sec. 2.2.5) that is also responsible for the exciton FSS. These measurements therefore nicely confirm that while the number of participating particles varies between two (X: one electron, one hole) and three (X^{+*}: one electron, two holes), the underlying physical effect leading to the FSS and the finite polarization degree is the same: the anisotropic exchange interaction.

Contrary to p, the energetic distance of the two XX^+ lines does not depend on QD size [Fig. 4.11(b)]. This distance is comprised of the triplet splitting of the two

holes in X^{+*} under the presence of a ground state electron (see Sec. 2.2.5). This splitting is >0 even for perfectly isotropic confinement potentials. Apparently it is not exclusively sensitive to the QD height but to other factors that can vary in the QDs even for constant transition energies[11] [see the large scatter between 0.2-1.4 meV for X energies around 1.3 eV in Fig. 4.11(b)]. This can be understood because the QD-size dependent effect responsible for symmetry lowering and therefore p and the FSS is piezoelectricity. For the triplet splitting symmetry lowering and therefore the size dependence of piezoelectricity is not the key factor.

Finally, the fine structure of the X^{++} will be discussed. Systematic investigation of the X^{++} lines requires a larger luminescence yield, since these line are usually weak in intensity. Sample ML is not suitable because the necessity to use metal shadow masks leads to a major cutback in detected intensity.

Instead, sample GI was examined. At energies >1.25 eV it enables single-QD spectroscopy without shadow masks due to the low spectral density in this energy range resulting from the long growth interruption (see Sec. 3.2.2). Unfortunately, the self-similarity of the QDs that enabled the analysis of the electronic structure with respect to QD size is not given in this sample. Still the X^{++} lines carry valuable information about the electronic structure of the QDs that can be extracted even without detailed knowledge of the specific structural parameter QD height.

Figure 4.12 (a)-(c) recalls the possible transition channels of X, X^{++}, and XX^+. Electronic states that do not participate in transitions observed in the experiment are gray-shaded. Their position in the energy schemes can not be verified by experiment in this work[12].

The two orange boxes in Fig. 4.12 (a)-(c) indicate similarities in the electronic structure of the different complexes. We start by comparing the possible X and X^{++} decay paths [Fig. 4.12 (a),(b)]. The X has two transitions which are energetically separated by the FSS, henceforth called Δ_1^X for the sake of notation conformity. The X^{++} has three transitions, two of them are separated by $\Delta_1^{X^{++}}$. Δ_1^X and $\Delta_1^{X^{++}}$ have in common that they both describe the anisotropic exchange interaction between electrons and holes. In the single-particle picture Δ_1^X describes the interaction between one ground state electron (e^0) and one ground state hole (h^0); $\Delta_1^{X^{++}}$ describes the interaction between e^0 and one first excited state hole (h^1) under the presence of two h^0. The question to be analyzed is whether Δ_1^X and $\Delta_1^{X^{++}}$ scale with each other quantitatively. Both values can easily be extracted from the spectra as shown in Fig. 4.12 (d).

Figure 4.13 (a) shows Δ_1^X vs. $\Delta_1^{X^{++}}$ for 26 QDs of sample GI. No correlation can be seen. Surprisingly, even the signs of the Δ_1^i are not correlated. It seems that the

---

[11]For example: aspect ratio, base length, interface roughness, strain fields …
[12]Only magnetic fields make the analysis of such states possible.
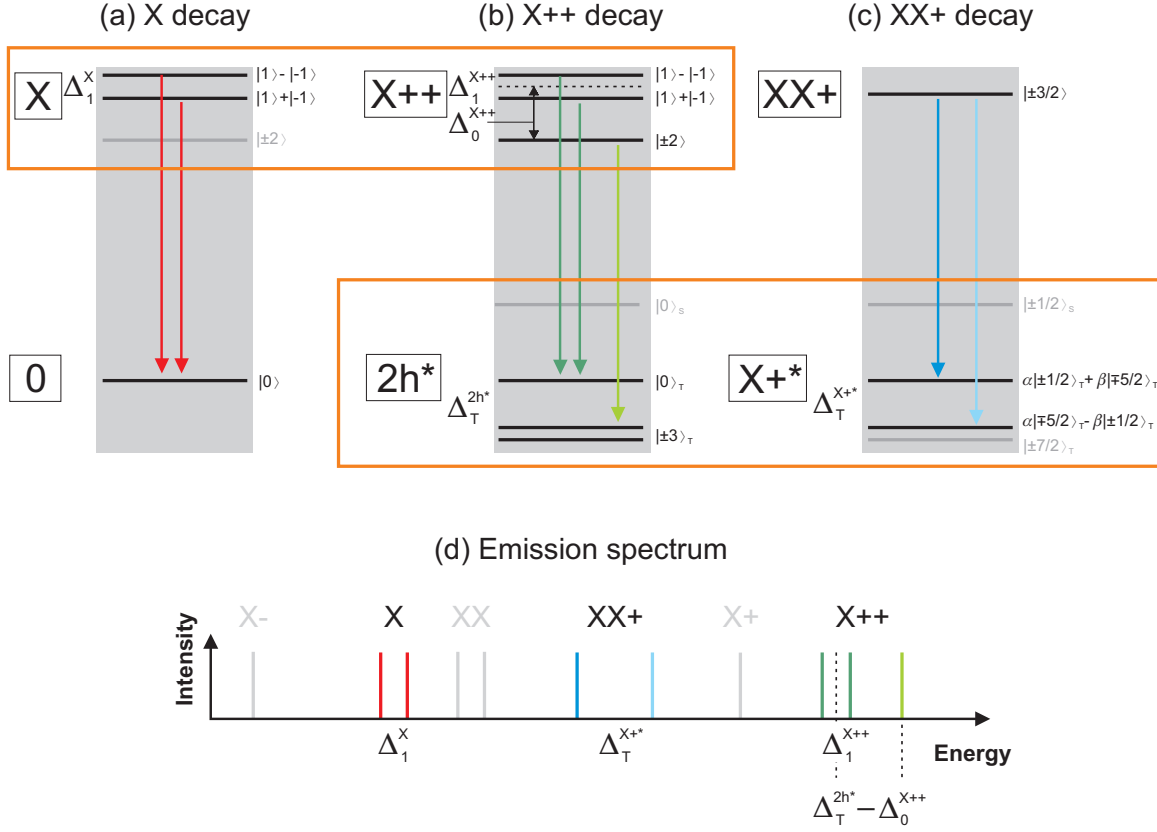

Figure 4.12: Transition schemes for the X (a), X^{++} (b), and XX^+ (c) decay. Arrows indicate possible recombination channels. The orange boxes highlight similarities in electronic structure of different complexes. Gray-shaded states do not participate in the experimentally observed transitions. (d) shows the resulting single QD emission spectrum. Gray-shaded lines indicate resonances from other complexes not discussed in (a)-(c).

interaction between e^0 and h^0 and between e^0 and $2h^0h^1$ are independent from one another. This may be due to the different wave function shape of h^0 and h^1. Still, some correlation between the two would have been expected. Accordingly, no educated guess concerning the exciton dark-bright splitting from the position of the third X^{++} line can be made. It would be very interesting to extend this study to lower energies where Δ_1^X is expected to increase drastically. Unfortunately a sample enabling this study is not available at this time.

Next, the focus will be placed on comparing the X^{++} and the XX^+ decay. The electronic structure of the corresponding final states 2h* and X^{+*} are both connected to the splitting of the triplet states of two holes. Δ_T^{2h*} describes the triplet splitting for one h^0 and one h^1. $\Delta_T^{X^{+*}}$ describes the splitting for the same particles, this time under the presence of an additional e^0. These parameters are not quite as easily accessible from the spectra as the Δ_1^i. $\Delta_T^{X^{+*}}$ is modified by the anisotropic exchange interaction via the mixing of the triplet states (see Sec. 2.2.5). This modification, however, should
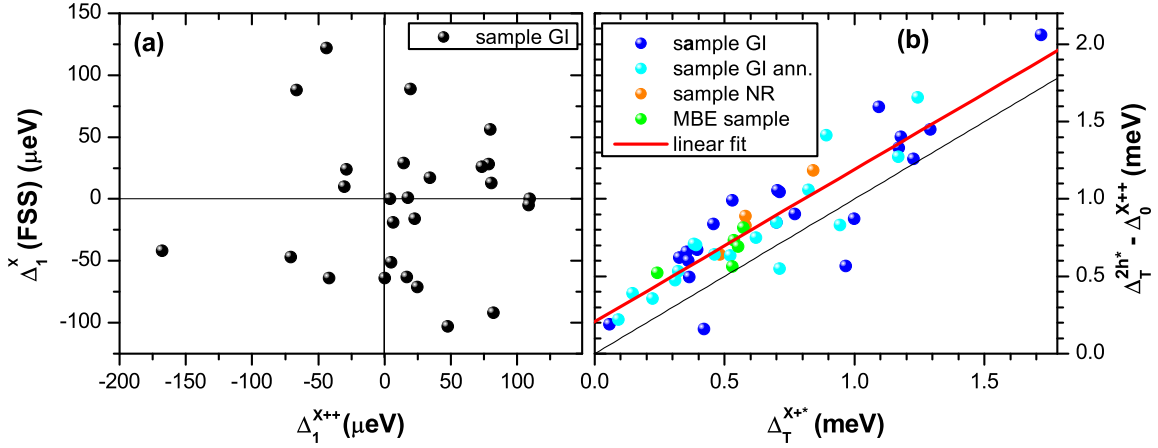
Figure 4.13: Quantitative comparison of different exchange energies. (a) X fine-structure splitting (Δ_1^X) vs. X^{++} polarization splitting ($\Delta_1^{X^{++}}$): No correlation is visible. (b) $2h^*$ triplet splitting (Δ_T^{2h*}) [minus X^{++} "dark-bright"' splitting ($\Delta_0^{X^{++}}$)] vs. X^{+*} triplet splitting ($\Delta_T^{X^{+*}}$): A clear linear dependence is observed. The linear regression (red line) yields a slope of 0.985 and an offset of 0.21 meV. For comparison, the black line has a slope of 1 and passes through the origin.

be sufficiently small for QDs with E(X)>1.25 eV [Fig. 4.11 (a)][13]. Δ_T^{2h*}, in turn, is decreased in the spectra by $\Delta_0^{X^{++}}$. This introduces some inaccuracy into the analysis since no experimental values for $\Delta_0^{X^{++}}$ exist. M. Ediger and coworkers have published theoretical values between 91 (InGaAs/GaAs QDs) and 178 μeV (InAs/GaAs QDs) [77].

Figure 4.13 (b) shows ($\Delta_T^{2h*} - \Delta_0^{X^{++}}$) vs. $\Delta_T^{X^{+*}}$ for three different samples [sample GI, sample NR and a reference sample of MBE grown InAs/GaAs QDs (data courtesy of E. Siebert and T. Warming)]. A strong correlation with a linear correlation coefficient of 0.90 can be seen. The linear regression yields a slope of 0.985 and an offset of 0.21 meV. This result nicely confirms the common origin of the fine structure of the XX^+ and the X^{++} emission: the triplet splitting of the two final state holes. It is also a strong proof for the correct identification of the X^{++} lines. Interestingly, the addition of the extra electron seems to lower this splitting in the X^{+*}, even outweighing the reducing influence of $\Delta_0^{X^{++}}$.

Table 4.3 gives a summary of the different exchange energies measured.

4.2.3 Summary

This section drew a detailed picture of the electronic (fine) structure of single QDs that is unprecedented in the literature. Sample ML presented a unique possibility to

---

[13]The low polarization degree p for high energies indicates weak mixing of the triplet states.

exchange term	sample	measured values
Δ_1^X (FSS)	sample ML	-80 - 520 μeV
	sample GI	-100 - 120 μeV
$\Delta_1^{X^{++}}$	sample GI	-170 - 110 μeV
$\Delta_T^{X^{+*}}$	sample ML	0.25[i] - 1.40 meV
	sample GI	0.05[i] - 1.70 meV
	sample NR	0.50[i] - 0.85 meV
$\Delta_T^{2h^*} - \Delta_0^{X^{++}}$	sample GI	0.15[i] - 2.05 meV
	sample NR	0.65[i] - 1.20 meV

Table 4.3: Summary of the exchange energy ranges measured in the three samples ML, GI, and NR. For a description of the different Δ terms see text and Fig. 4.12 (a)-(c).
[i] Smaller values below the experimental precision exist. QDs, where this was the case are not included in this summary because of unreliable line identification. Negative values, however, have not been observed.

link electronic with structural properties due to the self-similarity of QDs of different subensembles. By measuring the excitonic binding energies the complex interplay between charge carriers via Coulomb interaction could be dissected and direct Coulomb interaction, correlation, and exchange interaction were examined in detail. Especially the analysis of the exchange effects present a novelty by tracing back the fine structure of different complexes to their (sometimes common) physical origin. By comparing the experimental results with realistic modeling via eight-band $\mathbf{k}\cdot\mathbf{p}$ theory and CI some aspects of the electronic structure of QDs were found to be well described by the theory (sign and magnitude of the binding energies, trends of X^+ and XX binding energies and FSS with QD size) and other aspects were identified where the theoretical framework needs to be enhanced (trend of X^- binding energy with QD size, correlation, FSS magnitude). This should help to further improve existing models and thus deepen the understanding of the electronic structure.

4.3 Manipulation of the Electronic Structure via Thermal Annealing

The electronic structure of QDs has been analyzed in detail in the last section. When it comes to applications, targeted engineering of this structure is of utmost importance for device functionality and performance. The transition energy, for example, needs to be controlled in order to match the conditions specified by detector sensitivity or fiber

transmission characteristics. Moreover, as already mentioned, a vanishing exciton fine-structure splitting (FSS) in QDs is the key parameter for the generation of entangled photon pairs from the XX→XX→0 decay [23, 36, 114] that are essential for quantum key distribution protocols [106, 107]. In order to spectrally filter the two entangled photons it is favorable to be able to adjust the corresponding biexciton binding energy.

While the transition energy can be controlled to a certain degree by an appropriate choice of materials and adjusting the growth conditions, targeted growth of QDs with given binding energy or FSS is far more complicated. FSS post-growth modification was demonstrated using external electric [29, 115] and magnetic fields [116] as well as externally applied stress [117]. In order to limit the complexity of a final device, however, it is desirable to modify the FSS permanently, e.g. by precise variation of the QD structure. Thermal annealing at temperatures above the growth temperature can considerably alter the electronic structure of QD ensembles leading to a change of FSS [28, 65, 108] and biexciton binding energy [108]. While Refs. [28] and [65] measured average properties of QD ensembles, R. J. Young et al. determined the electronic properties of individual QDs by performing single-QD spectroscopy [108]. However, they analyzed QDs randomly chosen before and after annealing. In contrast to that, a systematic study of the influence of annealing on the emission characteristics of *one and the same* QD for consecutive steps of annealing is presented here.

The two consecutive annealing steps lasted five minutes at 710 °C and 720 °C respectively, performed under As atmosphere in the MOCVD reactor in order to stabilize the sample surface.

The main challenge that needs to be met in order to perform such an analysis is the spectroscopic measurement of the identical QD prior and after the annealing process. Since the annealing procedure takes place outside the cathodoluminescence setup the QD has to be relocated after removing the sample from and remounting it to the sample holder. The QD density has to be low enough to provide an unambiguous correlation between spatial coordinates and the specific QD measured. In other words, only one QD has to be detected for a certain position of the electron beam. Otherwise, the QD measured *after* the annealing process cannot be assigned unambiguously to the QD measured *before* the annealing process. The jitter pattern is no help here, since it does not work as a fingerprint for a QD when measured at two different points in time. Additionally, no shadow masks can be used since they are not stable at the temperatures required for annealing.

Sample GI meets these requirements by showing a low enough QD density at transition energies >1.25 eV. Circular mesas with 24 μm in diameter were etched into the sample surface that served as markers in order to roughly relocate the position on the sample. They are large enough to not influence the QD's electronic structure
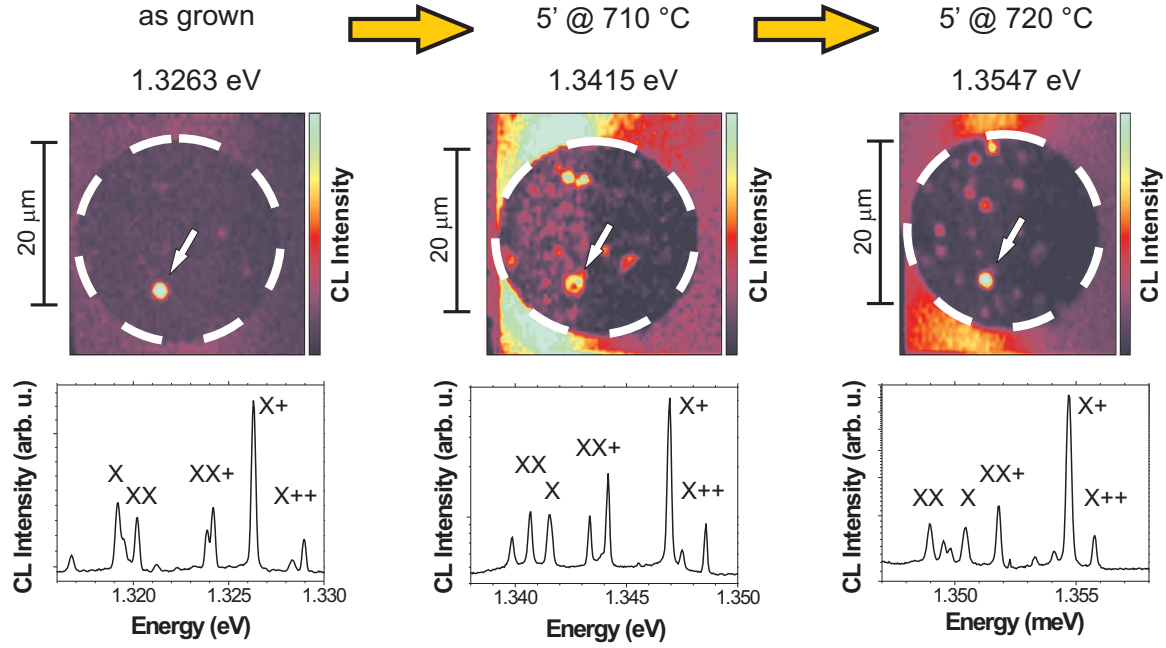
Figure 4.14: In the upper part, monochromatic CL images of the mesa are shown for the as-grown case and after two consecutive annealing steps. The position of the examined QD is indicated by a white arrow. The lower part shows CL spectra of the QD before and after the two respective annealing steps. The lines originating from neutral and charged excitonic complexes are identified.

via surface effects. Within one mesa the position of the QD can be very accurately located with the help of CL maps. Figure 4.14 shows monochromatic CL images of a mesa viewed from the top before and after the annealing steps. The bright spot in the images indicates the position of the QD under examination. In the two left images the energy of the X^+ transition energy is chosen, in the right image the energy of the XX transition. Sometimes other QDs in the same mesa emit light at the same energy. However, the QD density is low enough to attribute the bright spot indicated by the arrow in Fig. 4.14 to one and the same QD. It is thus possible to follow the evolution of the QD's spectrum over several annealing steps.

4.3.1   Transition Energies

The QD spectra change dramatically due to a modification of the QD structure during the annealing procedure. The main process that takes place is interdiffusion of In and Ga atoms since the annealing temperature of >700 °C is higher than the QD growth temperature of 485 °C. Ga incorporation into the QD leads to an increase of the band gap thus shifting the spectrum towards higher energies (see Fig. 4.15). In this specific example the X transition energy increased by 19.9 meV after two annealing steps at
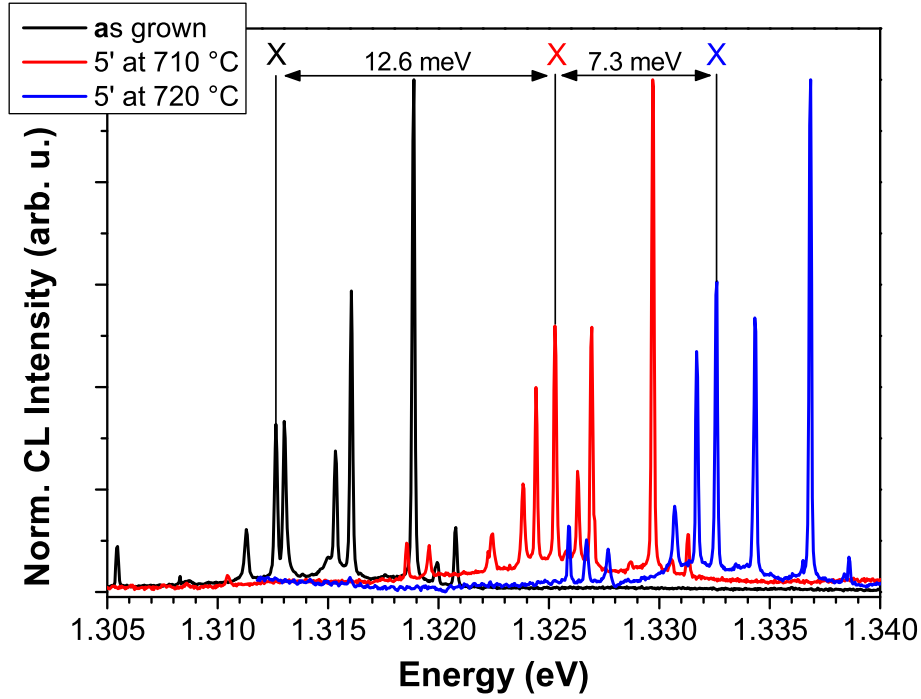
Figure 4.15: Effect of two consecutive annealing steps on the spectrum of a single QD. The X transition energy redshifted by an overall value of 19.9 meV due to the incorporation of Ga and the consequential band gap increase.

710 and 720 °C, respectively. For other QDs the shift was as high as 47.2 meV. This shows, that different QDs react very differently upon annealing depending on the local temperature reached and the local strain field.
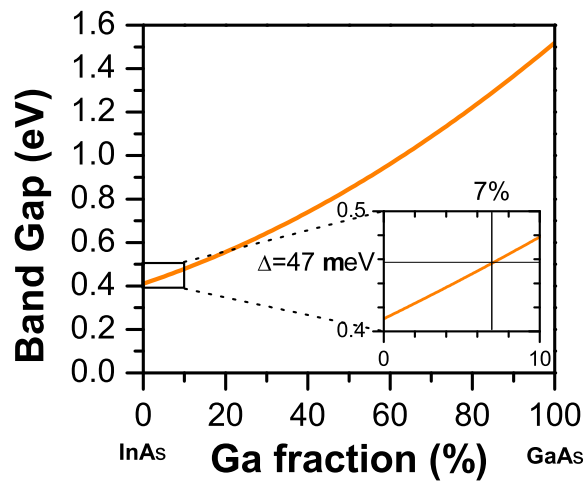

Figure 4.16: Band gap dependence on the Ga fraction in the ternary semiconductor InGaAs for 2 K (after [118]). The inset is a magnification for In-rich compounds showing a change in band gap of 47 meV for a Ga content of 7 %.

The band gap at 2 K of the ternary compound $In_xGa_{1-x}As$ is given by [118]

$$E_g(In_{1-x}Ga_xAs) = (0.4105 + 0.6337x + 0.475x^2) \text{ eV}. \tag{4.7}$$

This relation is visualized in Fig. 4.16.

A change of the band gap of InAs by 47 meV implies an average Ga content of 7 %. This, of course, is only a very rough estimate of the real situation. In fact, a grading of the interfaces will take place resulting in QDs with high In content in the center and high Ga content on the outside. Also, the average Ga content of 7 % is underestimated due to the fact that the effective size of the QD increases upon annealing. This weakens the effect of increased band gap reducing the total emission energies due to the quantum size effect.

4.3.2 Binding Energies

In view of the fact that the excitonic binding energies strongly depend on the QD structure (see Sec. 4.2.1), they should also change upon annealing. This will be analyzed in the following.

Again, neutral and charged excitonic complexes (X, X^+, X^-, XX, XX^+) were identified following the identification procedure introduced in Sec. 4.1. Figure 4.17 shows the change of the spectrum for a sample QD upon annealing. For ease of comparison the energetic position of the X line has been set to 0 meV. For the particular QD shown the X transition energy increased by 43.6 meV after both annealing steps. The XX shifts to lower energies with respect to the X line, changing its character from anti-binding ($E_{XX}^B = -2.1$ meV) to binding ($E_{XX}^B = 2.6$ meV) with a total change in binding energy of $\Delta E_{XX}^B = 4.7$ meV. Likewise, the X^+ binding energy increases by $\Delta E_{X^+}^B = 6.3$ meV. The X^- on the other hand shows the opposite trend becoming less binding with its binding energy decreasing by $\Delta E_{X^-}^B = $ -1.3 meV. The annealing process thus has a surprisingly large impact on all binding energies, suggesting a drastic change of the involved wave functions and/or their mutual position.

This time the majority of the excitonic complexes (X, X^+, XX, XX^+) show larger binding energies for larger X transition energies, contrary to what has been observed in sample ML (see Fig. 4.5). This is a consequence of the simultaneous variation of two parameters: a) QD material (and therefore band gap) and b) effective QD size. In this annealing series the *larger* the QD the *higher* its emission energy due to its higher Ga content. The binding energies are predominantly a function of wave function size and position and therefore react mainly to the size and shape of the confining potential. In both cases, sample ML *and* annealing series of sample GI, larger binding energies (except for X^-) are a consequence of the weaker hole-hole Coulomb interaction C_{hh}
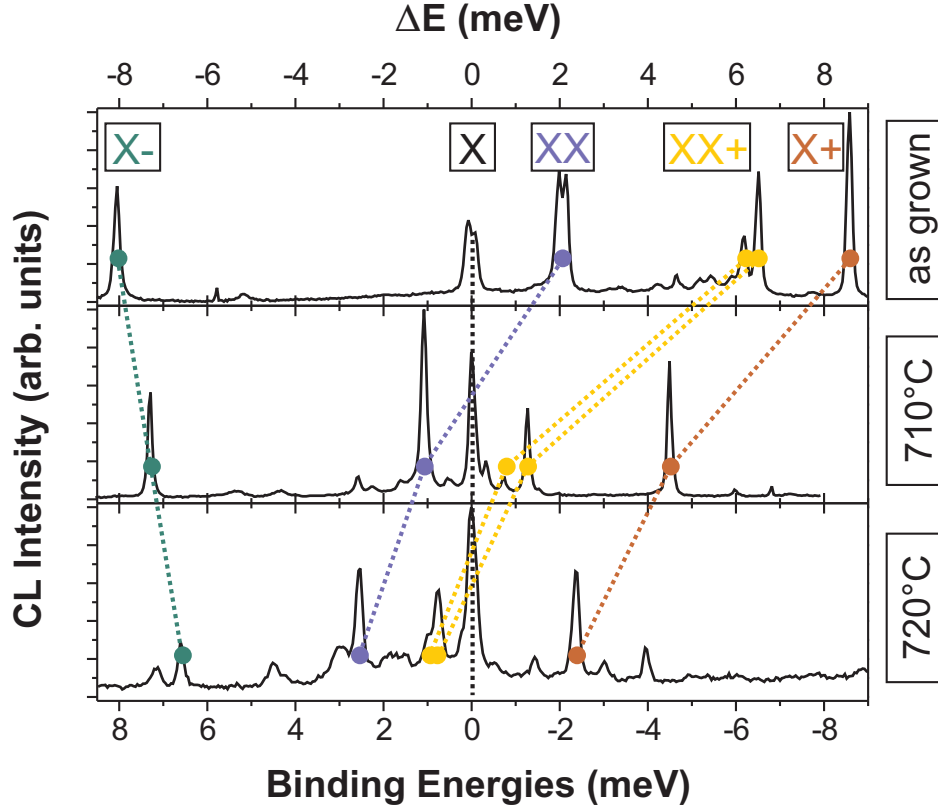
Figure 4.17: Effect of two consecutive annealing steps on the binding energies of the excitonic complexes of a single QD. 0 meV corresponds to the respective neutral exciton recombination energy (1.2738 eV for as-grown, 1.3002 eV for 710 °C, and 1.3174 eV for 720 °C). The X^- line shifts to higher energies with respect to the X line (i.e. the X^- becomes less binding). All other lines follow the opposite trend (i.e. become more binding).

due to the larger QD size (see also Sec. 4.2.1).

Figure 4.18 shows the change of the binding energies for X^+, X^-, and XX for three QDs that were tracked across three annealing steps (five minutes at 710, 720, and 730 °C, respectively). The qualitative trends confirm the results of Fig. 4.17. Quantitatively, however, the effect of the annealing process on the binding energies varies strongly.

The experimental results were again modeled using eight-band $\mathbf{k} \cdot \mathbf{p}$ theory for the single particle orbitals and CI for the few-particle states. The as-grown QD was assumed to have truncated pyramidal shape with {101} side facets, a height of 1.42 nm, a lateral size of 11.3 nm, and an In content of 100 %. There is some uncertainty concerning these numbers since the determination of the structure of a few small QDs within an ensemble of large QDs is very difficult. While reliable information about the QD structure in the similar sample ML exists [90], the exact influence of the long growth interruption on the morphology of the QDs is unknown. The annealing process and the resulting exchange of In and Ga atoms grades the interfaces between matrix
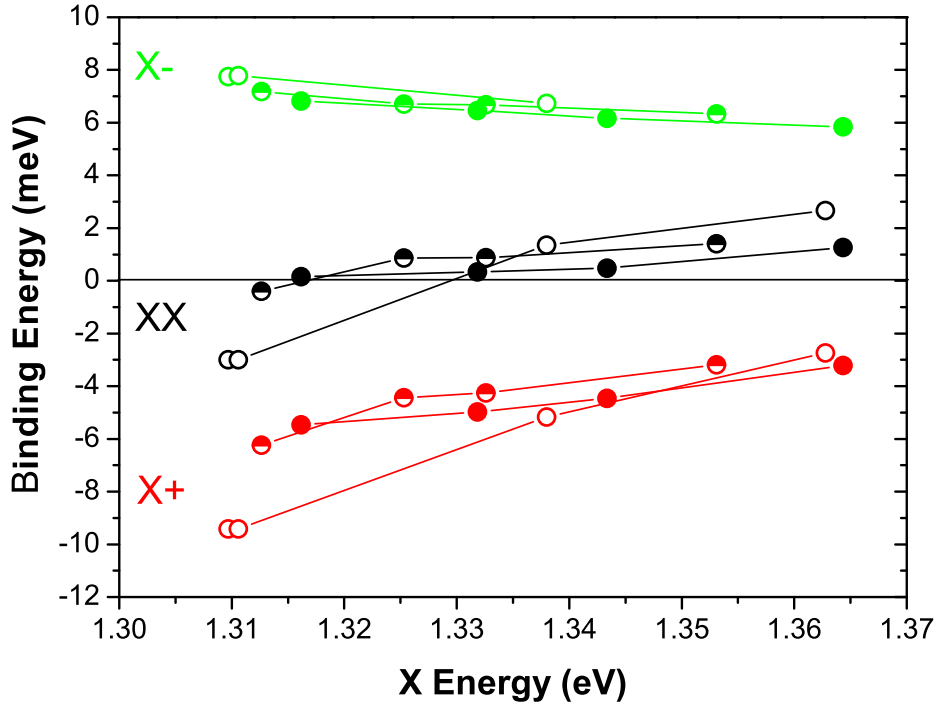
Figure 4.18: Effect of thermal annealing on the binding energies of three different QDs (indicated by different symbols). Shown are the binding energies for the QDs as grown and after the consecutive annealing steps at 710, 720, and 730 °C (from left to right), respectively. The annealing leads to a change in exciton transition energy due to the change in band gap of the QD material (horizontal shift of the data points) and to a change in binding energies mainly due to the variation in wave function shape (vertical shift, see text).

material and QD. This effect was simulated by applying a smoothing algorithm for each annealing step, corresponding to Fickian diffusion.

Results for the calculated binding energies of X^+, X^- and XX are shown in Fig. 4.19. The experimentally observed energetic order of X^- and X^+ is reproduced by the theory. Also, the general trend of the trion binding energies upon annealing (X^- becomes less binding, X^+ becomes more binding) is in good agreement. However, there are some discrepancies between theory and experiment: The change of character of the biexciton (i.e. from anti-binding to binding) as observed in the experiment is not reproduced by the modeling. Also, the experiment revealed a much stronger relative shift for X^+ and XX than for X^- (see Fig. 4.17). Even more striking is the fact, that the interdiffusion assumed in the model is very strong leading to a shift of the X transition energy of 193 meV. Even so, the change in binding energies is very moderate. The process of annealing and its effect on the electronic structure of the QDs is apparently not correctly reproduced by the modeling.

Remarkably, the inaccurate trends can be corrected, when the attractive Coulomb interaction between electron and hole (J_{eh}) is artificially lowered for the as-grown QD
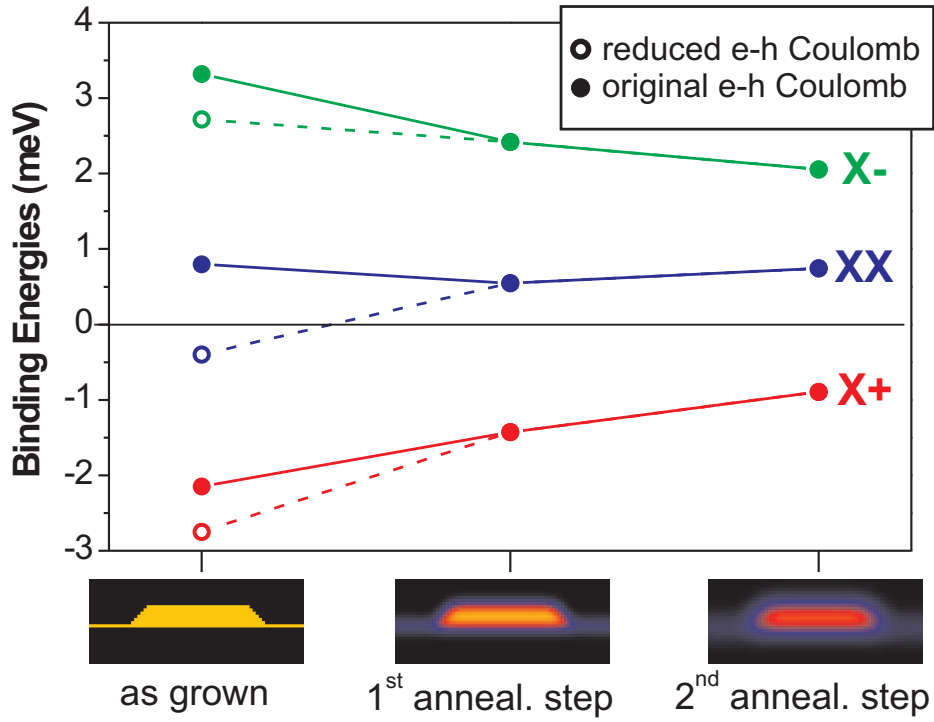
Figure 4.19: Calculated binding energies for X$^-$, X$^+$, and XX. The exciton transition energies are 1.0786 eV for the as-grown case and 1.1949 and 1.2716 eV for the annealed QDs, respectively. Open symbols correspond to a reduction of electron-hole Coulomb interaction by 0.6 meV simulating a misalignment of electron and hole wave functions (see text). The structural definition of each model QD for the calculation is displayed.

by 0.6 meV, corresponding to a reduction of 3%, while repulsive electron-electron (J_{ee}) and hole-hole (J_{hh}) Coulomb terms are left unaltered. Such an effect may result from a reduced electron-hole wave function overlap caused by either a slight elongation and misalignment of the wave functions or a mutual vertical displacement.

Using the assumption of reduced J_{eh} for the as-grown QD we observe both the biexciton crossover as well as the relative insensitivity of X$^-$ binding energy to annealing as seen in the experiment (open symbols in Fig. 4.19). A symmetrization of the wave functions with annealing is further supported by the drastic reduction of FSS [65] (see next section).

4.3.3   Fine-Structure Splitting

The excitonic FSS was recorded by performing polarization-dependent measurements. Generally, the FSS always decreased upon annealing. For the particular QD shown in Fig. 4.20 it decreased from 170 μeV to less than 20 μeV. By an appropriate choice of annealing temperature and duration it should thus be possible to reduce the FSS
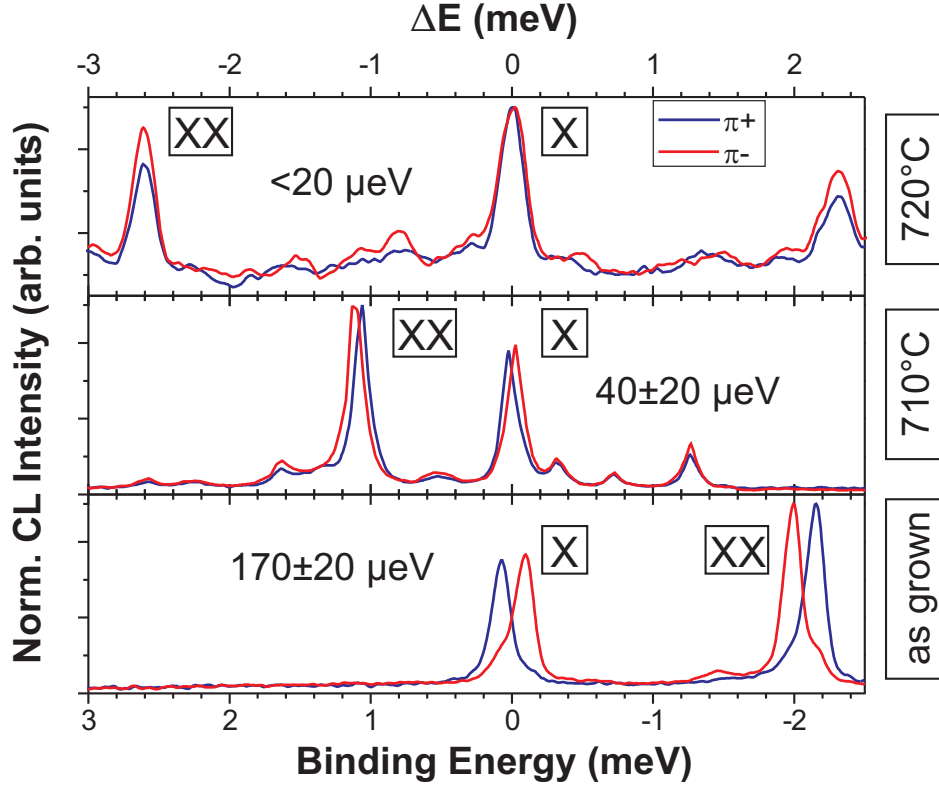
Figure 4.20: Polarization-dependent measurements of the same QD as depicted in Fig. 4.17 reveal the excitonic fine-structure splitting. It decreases from 170 ± 20 μeV to less than 20 μeV after the second annealing step.

in a controlled way below the homogeneous line width of the X-line (which is on the order of a few μeV at liquid He temperatures), a prerequisite for the generation of polarization-entangled photon pairs [36, 114].

The general trend of decreasing FSS [28, 65, 108] and increasing XX binding energy [108] by annealing has also been observed by other authors. Both were explained by a not further specified "symmetrization" of electron and hole wave functions. A possible explanation for this effect is that interdiffusion of Ga and In atoms reduces the strain fields in the structure by smoothing the interfaces. A reduction of the shear strain components in particular results in a decline of piezoelectric fields. As Sec. 4.2.2 has shown, these piezoelectric fields, in turn, summon the main part of the FSS. Consequently, the annealing should indeed lower the FSS as observed in the experiments.

4.3.4 Summary

Thermal annealing of the QDs at temperatures around 700 °C turned out to drastically influence their electronic structure. It is therefore a promising way for targeted

engineering of their emission characteristics: It was possible to increase the emission energies by almost 50 meV. The binding energies of the different complexes changed drastically. The largest impact was observed on the X^+ binding energy with a maximum total increase of more than 6 meV. It was further possible to induce a change of the character of the XX and XX^+ from anti-binding to binding. Finally, successful modification of the FSS was demonstrated. For a model QD the FSS decreased from 170 to less than 20 μeV upon annealing. This study is, however, only a first step towards a control of the electronic properties of QDs precise enough for device fabrication since the annealing steps were too rough to actually tune binding energies or FSS to a predetermined value.

Similar experiments that confirm the trends of X transition energy, XX binding energy and FSS have been conducted by D. J. P. Ellis and coworkers [119]. A different Ansatz for annealing has been reported by A. Rastelli and coworkers [120]. They applied the same laser beam used at low laser power to characterize QDs in a microcavity structure in a μPL setup to also anneal these QDs at high laser power. Despite the obvious advantage of being able to anneal *and* characterize the QDs in the same setup, they were able to tune the QD emission energy with resolution-limited accuracy. This way it could also be possible to tune binding and exchange energies on a similarly accurate scale. With this technique used on unprocessed samples, however, heat dissipation may present a limitation to the maximum local temperature of the QDs induced by the laser beam.

4.4   Time-Resolved Measurements

Chapter 2.4 predicted that the fine structure of the different excitonic complexes that has been studied in the last sections influences their decay times via the number of possible decay paths. In this section transients of emission lines from single QDs are presented in order to analyze the dynamics of the recombination processes. This study is mostly restricted to emission lines from X, X^+, XX, and XX^+ recombination since the intensity of the X^- and X^{++} transitions was too low to obtain a sufficient signal-to-noise ratio.

An example of the transients of different emission lines from one QD is given in Fig. 4.21. Different decay behaviors can be seen: the XX^+ intensity[14] decays the fastest followed by the XX-, X^+-, and X-line in that order.

---

[14]The XX^+ transient was always obtained from the more intense of the two emission lines. The other line yields the exact same decay time since the occupation of the very same complex is probed. However, due to the weaker intensity the signal-to-noise ratio is lower and thus the error in the extracted decay time is larger.
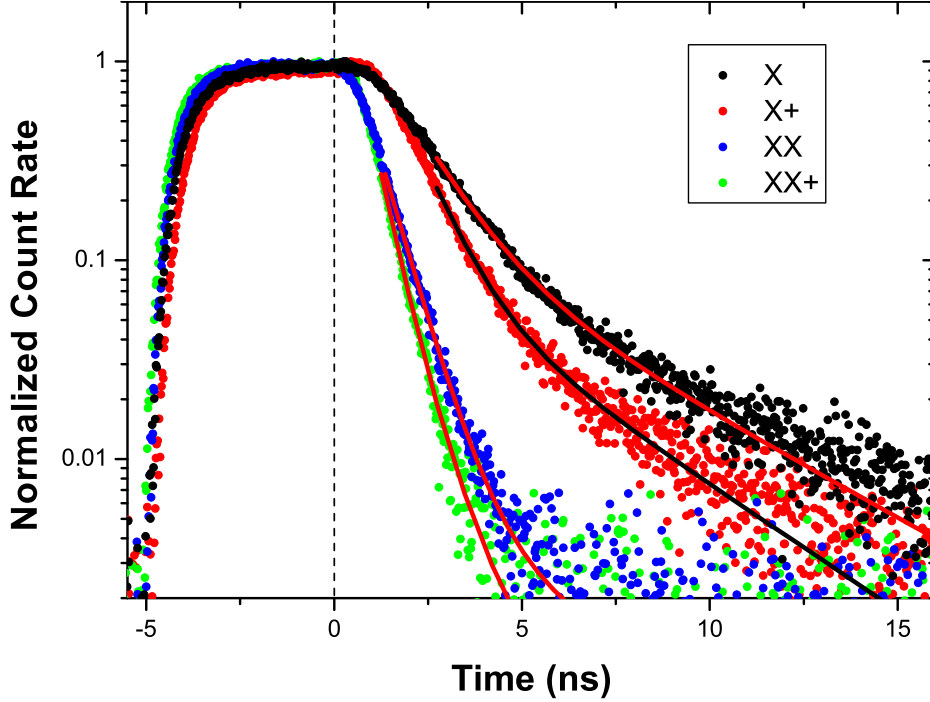
Figure 4.21: Transients of X, X^+, XX, and XX^+ from one QD. For all QDs measured, the decay times of neutral and charged excitons are noticeably longer than for the neutral and charged biexcitons. $t=0$ denotes the time when the electron beam was switched off.

The transients are dominated by a fast initial decay but the greater part also exhibit a second slower component. For X and X^+ transients the relative amplitude compared to the fast decay was between 0 and 0.1, for the XX and XX^+ transients between 0 and 0.01. The time constants for the slow component range between 4 and 9 ns. The second component originates from a process that feeds the initial state of the transition on a time scale slower than the initial decay after the global excitation (here the electron beam) has been switched off. In X-transients this has been attributed to the conversion of dark excitons to bright excitons via spin-flip processes [121]. This mechanism is unlikely here, since the same phenomena is present in the X^+, XX and XX^+ transients where no such dark states exist. Since X and X^+ exhibit a more intense second component than XX and XX^+ this suggests a feeding process due to lateral transfer from a low density of external charge carriers produced by re-emission from QDs or shallow defect states [122, 123].

In the following the fast initial decay of the different complexes will be analyzed. For the example in Fig. 4.21 the decay times were $\tau_X = 1.3$ ns, $\tau_{X^+} = 0.9$ ns, $\tau_{XX} = 0.75$ ns, and $\tau_{XX^+} = 0.6$ ns.

Figure 4.22 summarizes the results of the analysis of 26 different QDs of sample NR. The average decay times are $\bar{\tau}_X = 1.22 \pm 0.25$ ns, $\bar{\tau}_{X^+} = 0.97 \pm 0.15$ ns, $\bar{\tau}_{XX} = 0.86 \pm 0.12$ ns, and $\bar{\tau}_{XX^+} = 0.66 \pm 0.14$. The order of the complexes from slowest to
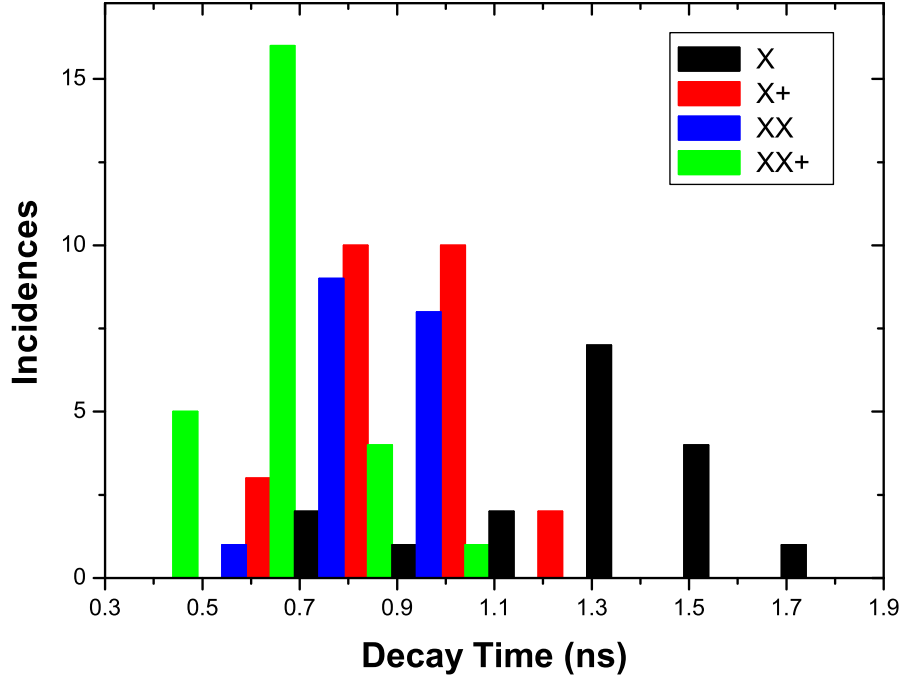
Figure 4.22: Distribution of the measured decay times for 26 QDs. The average decay times are $\bar{\tau}_\mathrm{X} = 1.22{\pm}0.25$ ns, $\bar{\tau}_{\mathrm{X}^+} = 0.97{\pm}0.15$ ns, $\bar{\tau}_\mathrm{XX} = 0.86{\pm}0.12$ ns, and $\bar{\tau}_{\mathrm{XX}^+} = 0.66{\pm}0.14$ ns.

fastest decay was almost always X, X^+, XX, XX^+ as in Fig. 4.21. It is noteworthy that the decay times of the X show a much larger scatter than the times of the other complexes as indicated by its larger standard deviation of 0.25 ns. The exciton decay times vary between 0.7 ns and 1.7 ns, a factor of 2.4. Apparently, the exciton wave function is more sensitive to variations in the QD structure than the wave function of other complexes. These results show that similar QDs in the same sample can exhibit very different dynamic behaviors. It is therefore important to probe the decay dynamics on a single-dot level and not to rely on ensemble measurements (that average over a large number of different QDs *and* different excitonic complexes) when analyzing dots for *single*-QD-based applications.

Due to its weak intensity, transients of the X^- could be measured for two QDs only. The sets of decay times were $\tau_\mathrm{X} = 1.4$ ns, $\tau_{\mathrm{X}^+} = 0.75$ ns, and $\tau_{\mathrm{X}^-} = 0.9$ ns for one QD and $\tau_\mathrm{X} = 1.4$ ns, $\tau_{\mathrm{X}^+} = 0.75$ ns, and $\tau_{\mathrm{X}^-} = 2.2$ ns for the other. No reliable trends or conclusions for τ_{X^-} can be drawn from just these two data points.

For six QDs the X^{++} resonance was strong enough for time-resolved measurements. $\tau_{\mathrm{X}^{++}}$ scatters between 0.9 and 1.2 ns and is identical within 0.2 ns to τ_{X^+}.

Figure 4.23 shows the decay times vs. the X^+ transition energy[15] analogous to

---

[15]Not all QDs showed a clear exciton resonance. However, the energetic distance between X and X^+ (i.e. the X^+ binding energy) is typically <10 meV, and therefore negligible for the energy range
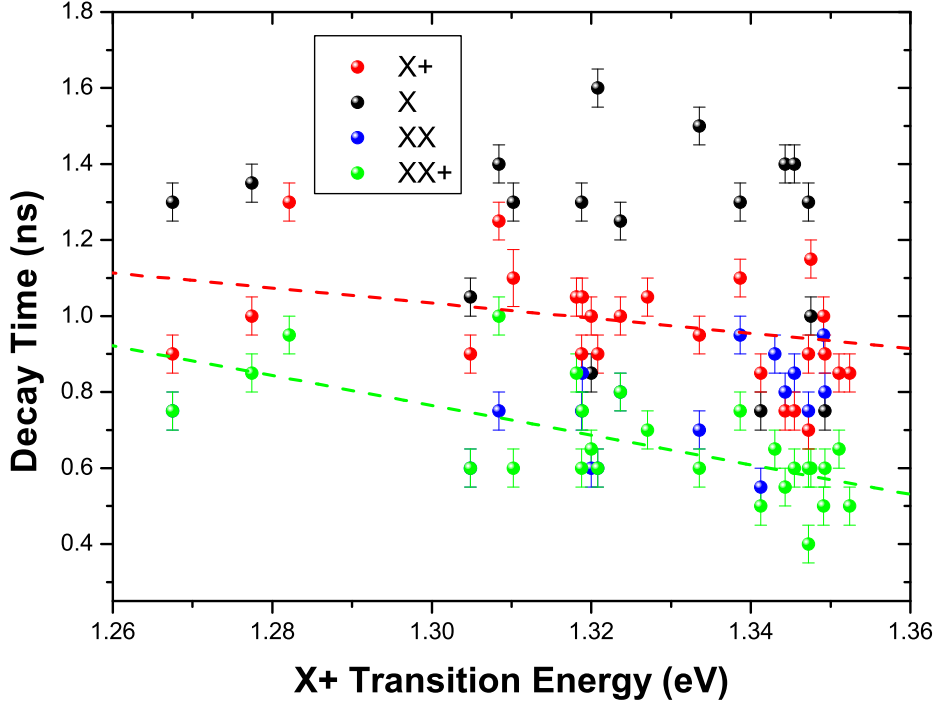
Figure 4.23: Decay times versus X^+ transition energy. Tentative trends are visible for XX and XX^+ only, as indicated by the linear regressions (dashed lines).

Fig. 4.5 for the binding energies. Unfortunately, the outcome is much less convincing mainly because of the reduced sensitivity of the APD combined with the lack of a sample with large QDs and simultaneous low QD density which result in a lack of suitable data for QDs with transition energies smaller than 1.26 eV.

For X^+ and XX^+ a slight increase of the decay times can be presumed for lower energies as indicated by the dashed linear-regression lines. This requires a smaller electron-hole wave-function overlap for the corresponding QDs. This is not surprising down to a certain QD size because the carriers are confined stronger in smaller QDs and hence their wave functions are more compact. From a certain point on, however, an inversion of this trend is expected because the wave functions start to ooze out more into the matrix. The reason why this is not observed here remains unclear. Time-resolved measurements of larger QD with transition energies smaller than 1.25 eV might give a conclusive answer to this question.

In order to compare the decay times of X and XX, identical characteristic transition times [that describe the decay through single possible recombination channels (see Sec. 2.4)] of X and XX are assumed. This assumption is supported by G. A. Narvaez and coworkers who calculated characteristic transition times for lens-shaped $In_{0.6}Ga_{0.4}As/GaAs$ QDs [83]. For their QDs the characteristic transition times
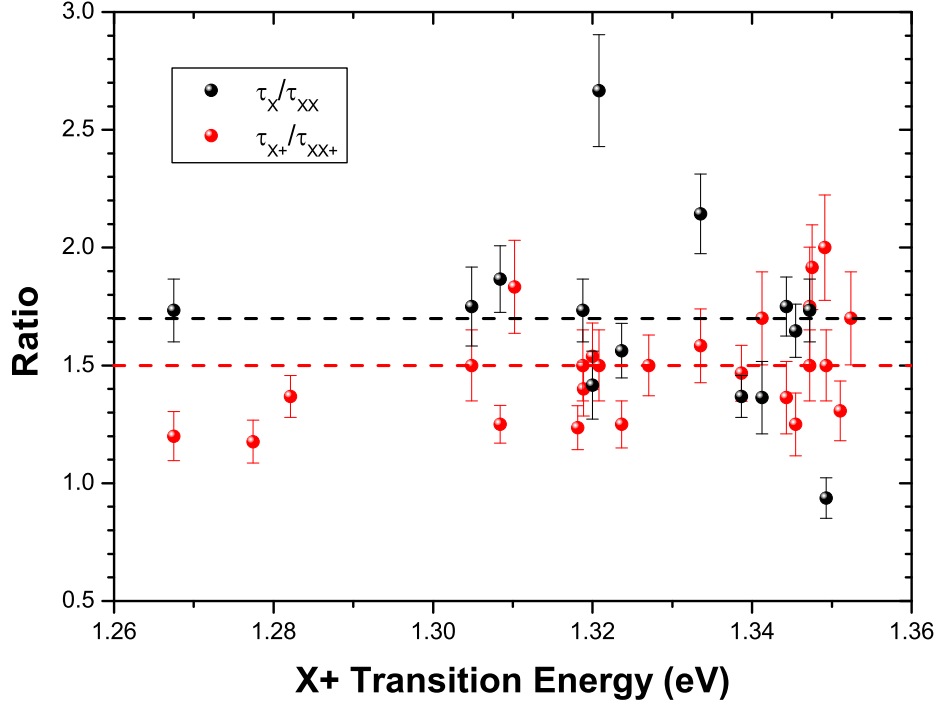
---

displayed in Fig. 4.23.

Figure 4.24: Selected Ratios of decay times versus X^+ transition energy. The measured value of $\tau_X : \tau_{XX^+} = 1.7 \pm 0.4$ deviates somewhat from the theoretically expected value of 2 due to a variation of *characteristic* transition times (see text). $\tau_{X^+} : \tau_{XX^+} = 1.5 \pm 0.2$ confirms the theoretical value. The different errors originate from different signal-to-noise ratios of the transients (see also App. C).

of the X and XX transitions are comparable for all QD sizes. This means that the expected ratio of decay times $\tau_X : \tau_{XX}$ according to their calculations is 2 due to the different number of decay channels (see Sec.2.4 and Fig. 2.14).

For the charged complexes, the situation seems to be more complex. According to Ref. [83] the characteristic transition times of X^+ and X^- critically depend on QD height. Therefore, a comparison of the decay times merely with the argument of a different number of decay channels seems to be less sensible. However, as a hypothesis we will assume that the characteristic transition times of similarly charged complexes, e.g. X^+ and XX^+ are similar. If this hypothesis is correct, the expected ratio $\tau_{X^+} : \tau_{XX^+}$ is 2 since X^+ has two and XX^+ has four possible decay channels (see Fig. 2.14). In the last section it has become clear, however, that one of the decay channels of the XX^+, namely the decay into the X^{+*} singlet state has a negligible oscillator strength. This alters the expected ration of the decay times. If the oscillator strength of the singlet states is indeed zero we are left with three XX^+ transitions changing the ratio $\tau_{X^+} : \tau_{XX^+}$ to 1.5.

Figure 4.24 shows the discussed decay time ratios for all QDs measured vs. X^+ transition energy. The mean values are 1.7±0.4 for $\tau_X : \tau_{XX}$ and 1.5±0.2 for $\tau_{X^+} : \tau_{XX^+}$.
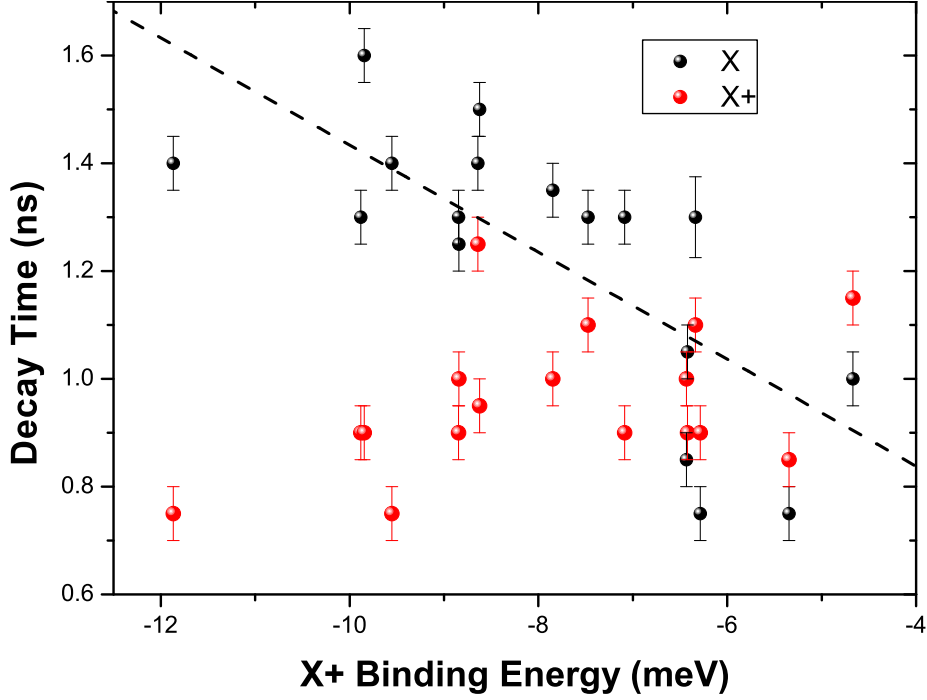
Figure 4.25: Decay times of X and X^+ versus X^+ binding energy. The exciton decay time increases with decreasing trion binding energy. Both depend on the electron-hole wavefunction overlap.

$\tau_X : \tau_{XX}$ is a bit below the expected value of 2. Additionally, the values show a large scatter. This means that the specific QD properties have a decisive influence on the ratio, especially via τ_X as we know from Fig. 4.22. Qualitatively, the longer decay time of the exciton with respect to the biexciton can be explained with the different number of decay channels as discussed in Sec. 2.4 (see especially Fig. 2.14). The exact value, however, crucially depends on the specific QD since the characteristic transition times seem to differ a lot from case to case and are not always comparable as in Ref. [83]. It is therefore not advisable to generalize results on $\tau_X : \tau_{XX}$ from just one or even a few QDs.

The picture changes for the $\tau_{X^+} : \tau_{XX^+}$ case. Here, the measured mean value matches exactly the expected value of 1.5. This result also confirms that the singlet transition indeed has negligible transition probability. The scatter is considerably smaller with a standard deviation of 0.2 indicating a closer consistency of the characteristic transition times of positively charged exciton and biexciton from dot to dot than for the neutral complexes.

A last investigation consists of the comparison of decay times and binding energies. This is interesting, since both parameters should be influenced by a common factor: the overlap of electron and hole wave functions. The smaller the overlap, the smaller the attractive Coulomb interaction C_{eh} and the smaller the binding energies of the

excitonic complexes (given that C_{ee}, C_{hh}, and correlation are kept constant). On the other hand, decreased wave function overlap increases the radiative lifetime of the excitonic complexes.

Figure 4.25 shows the decay times τ_X and τ_{X+} vs. the X^+ binding energy. Qualitatively, τ_X shows the expected tendency: Low X^+ binding energy coincides with longer decay time an vice versa. τ_{X+} on the other hand does not show this trend. Here, the simple picture of treating the many-particle complex as the sum of the single particles and thus arguing with (single) electron-hole wave function overlap fails. The robustness of τ_{X+} with respect to the X^+ binding energy compared to τ_X is the same effect as the larger scatter of τ_X with respect to all other decay times seen from a different angle. An exact explanation of this phenomenon, however, can not be given at this point.

This section has highlighted two findings. First of all, QDs from the same sample show very differing decay times for all excitonic complexes even for similar transition energies although the order is generally preserved: $\tau_X > \tau_{X+} > \tau_{XX} > \tau_{XX+}$. The second main lesson to be learned is that the different electronic fine structure of the various complexes is closely linked to the different recombination dynamics these complexes show in time-resolved experiments.

Chapter 5

Summary and Conclusion

In the work at hand single InAs/GaAs quantum dots (QDs) were investigated by catho-doluminescence spectroscopy. The main focus was placed on the energetic spectrum of excitonic complexes and its manipulation for the application of single QDs in novel devices, such as single-photon emitters for quantum communication.

The spectra of single QDs were isolated using different experimental techniques. Two different growth modes of the QDs were employed to achieve a QD density low enough to separate the spectra without further aid: One mode consisted of applying a 540 s growth interruption after deposition of the QD material. A ripening process during this growth interruption leads to a QD distribution consisting of mainly large QDs emitting at wavelengths >1000 nm. Very few small QDs remain emitting at shorter wavelength granting a spectral density of such QDs low enough for single-QD spectroscopy. In the other growth mode the conventional rotation of the substrate during QD growth was shut off. This leads to a very inhomogeneous QD density distribution ranging from 0 to >10^{10} QDs per cm^2. In some regions of the grown sample this again results in low enough QD densities. A third sample with a higher QD density was examined by applying near-field metal shadow masks with nano-apertures on the sample surface. This leads to a selection of QDs which are situated directly under the aperture and makes single-QD spectroscopy feasible.

Thus, spectrally sharp resonances of single QDs could be examined in the emission spectra. Identification of resonances from one and the same QD was possible by utilizing the spectral diffusion of the lines. Local electric fields in the QDs' surrounding lead to a slight energetic jitter of the lines, unique for every QD. Lines with the same jitter pattern could therefore be assigned to the same QD.

A single-QD spectrum regularly consisted of up to ten sharp emission lines. Systematic recording of a large number of such spectra together with polarization and excitation dependent measurement unveiled the decay of different excitonic complexes

as the origin of the lines. Neutral, singly and multiply charged excitons and biexcitons (X, XX, X$^+$, X$^-$, XX$^+$, X^{++}) were identified and their spectral resonances were studied as a function of the structural properties. Positively charged complexes were dominant due to unintentional positive background doping of the samples.

Special attention was given to the electronic fine structure of the complexes induced by carrier-carrier exchange interaction. Intensive theoretical analysis of this interaction was conducted and model spectra were deduced by analyzing both initial and final states of the different decay paths. The spectra were then compared to the experimental results. This led to a deep understanding of the exchange interaction and its dependence on QD geometry and piezoelectric effects. A number of different exchange energies was measured [among them the technologically relevant exciton fine-structure splitting (FSS)] and compared to each other to uncover similar origins for fine structures of different complexes.

The extensive compilation of measured binding energies and fine structures of the excitonic complexes revealed an interrelation of the QD structure and the energetic spectrum of the excitonic complexes. This is a major prerequisite for targeted design of the electronic structure for applications. Depending on QD height, biexciton binding energies between -8.1 and 5.1 meV were measured and a binding to antibinding crossover was observed at 1.23 eV.

Of particular importance is the demonstration of manipulation of the excitonic FSS. Values between 520 and -80 μeV were measured depending on the height of the specific QD implying the existence of QDs with a FSS close to zero. The physical origin of this dependency was examined. The most promising candidate is piezoelectric fields which are stronger for large QDs and thus generate larger FSS values for large QDs.

As a first step of post-growth manipulation of the electronic structure the geometrical structure of the QDs was altered by a thermal annealing process. The electronic properties were monitored and thus a possibility to fine-tune binding energies and excitonic fine-structure splittings was demonstrated. The annealing process showed a significant reduction of the FSS. For a sample QD it could be reduced from 170 μeV to below the resolution of the experimental setup, i.e. below 20 μeV. The biexciton binding energy increased from -2.1 to 2.6 meV. Both effects indicate a symmetrization of electron and hole wave functions induced by the annealing procedure.

In order to further complete the picture of excitonic complexes, time-resolved cathodoluminescence spectroscopy was conducted in order to analyze the decay dynamics in the QDs.

The influence of characteristic transition times and electronic fine structure on the dynamics was analyzed. Surprisingly, the scatter of the exciton decay times from dot to dot is larger than the scatter of the other complexes' decay times indicating a greater

sensitivity of the exciton wave function to the QD's structural properties. No clear dependence on the transition energy was observed in the 1.26 to 1.35 eV range. The mean value for $\frac{\tau(\text{X})}{\tau(\text{XX})}$ was 1.7 ± 0.4 slightly deviating from the value of 2 dictated by the different number of decay channels alone. This implies shorter characteristic transition times for XX than for X. The measured value for $\frac{\tau(\text{X}^+)}{\tau(\text{XX}^+)}$ was 1.5 ± 0.2 thus matching the expected theoretical value. This indicates similar characteristic transition times for X$^+$ and XX$^+$. The additional positive charge carrier seems to stabilize the wave function overlap when an additional exciton is added to the complex, as indicated by the smaller standard deviation of $\frac{\tau(\text{X}^+)}{\tau(\text{XX}^+)}$ with respect to $\frac{\tau(\text{X})}{\tau(\text{XX})}$.

The new insight into the electronic structure of single InAs/GaAs QDs gained in this work is substantial and in its thoroughness unprecedented in the literature. This applies in the context of a single QD, its binding energies and electronic fine structure and to the generalization to an ensemble of QDs gained by the large amount of single-QD data gathered in this work. That, together with the demonstrated possibility of targeted engineering via thermal annealing comprises invaluable information for QD optimization for innovative applications of single QDs in single photon emitters, memory devices and qubit registers.

SUMMARY AND CONCLUSION

Chapter 6

Outlook

This concluding chapter gives a brief outlook and shows, where the knowledge gained in this work can be exploited for new or complementing experiments.

This work intensively examined the electronic structure and fine structure of the lowest excitonic complexes in quantum dots (QDs), the most complicated being the positively charged biexciton consisting of two electrons and three holes. Generally, the number of charge carriers simultaneously present in a QD is limited only by the number of bound energy states. Technically this implies that more complicated complexes can be formed, each with its own unique energy structure and transition lines to be studied. Indeed, even in this work some lines appeared at higher excitation densities, that are traces of higher yet unidentified excitonic complexes.

One way of generating such higher complexes in a more controlled way is to embed the QDs into a diode structure. By applying an external voltage the QDs can be precharged accordingly and, by (optically) generating an exciton or a biexciton arbitrarily complex few-particle states can be generated [124]. Of course both the diode and the QDs have to be fabricated with care, i.e. with correct composition, thickness, doping concentration, and QD density. M. Edinger and coworkers optimized such a structure and demonstrated differently charged particles in the same QD ranging from sixfold negatively to sixfold positively charged excitons depending on the externally applied voltage [19].

Another interesting subject of investigation are recently developed submonolayer QDs. Here, the amount of deposited InAs is below one monolayer, producing islands without a wetting layer. The development of such structures is currently still in its early phase. Little is known about both geometrical and electronic structure of such quantum objects and their differences and similarities to Stranski-Krastanow QDs. Nonetheless, integration of submonolayer insertions into laser structures resulted in very fast devices [125], showing their great potential for opto-electronics.

Recently, successful fabrication of two electronically coupled QDs, so-called QD molecules (QDM), has been demonstrated and optical spectroscopy of single QDMs has been conducted. The QDs were either vertically stacked [126, 127, 128] or laterally positioned [129, 130]. This presents a new class of semiconductor quantum structures with novel electronic properties. As of now, the optical investigations were limited to simple excitons and trions, both spatially direct (all charge carriers in one of the two constituting QDs) and indirect (charge carriers in both constituting QDs). The fine structure of these particles is very complex and has only been started to be examined in detail.

The application of magnetic fields makes the investigation of g-factors of different complexes possible. Spectroscopic experiments have shown, that exciton g-factors in self-assembled As-based QDs can range between -3.1 and -0.4 depending on the specific QD structure [21, 131, 132]. A thorough understanding of this interrelation between structure and g-factors and other spin related properties (e.g. spin-flip processes, spin dynamics) is needed in order to make QDs applicable for spintronics. Furthermore, magnetic fields grant access to forbidden states like the dark exciton states [22] and reveal additional exchange effects.

Experiments involving external magnetic fields, however, are not possible with the cathodoluminescence setup presented here since the fields would render a correct mapping of the electron beam by the system of magnetic lenses impossible. Such experiments would have to be performed in all-optical setups like micro-photoluminescence. Also, for experiments that require spin-sensitive and/or resonant excitation cathodoluminescence is not the correct choice since here the excitation mechanism is incoherent and always at energies high above the band-gap energy. An example of such experiments is micro-photoluminescence-excitation spectroscopy where the absorption spectra of single QDs are probed. This experiment has been set up at the Technical University of Berlin and promises to complement the work at hand on the emission spectra by providing the corresponding absorption spectra of excited excitonic complexes.

In order to exploit the specific strengths of the cathodoluminescence setup, i.e. large excitation densities and potentially high spatial resolution when carrier diffusion is quenched, the examination of nitride-based quantum structures is suggested. Such structures based on InN, GaN, AlN and their ternary and quaternary alloys have experienced a technological boost in the last decade with the successful development of ultra-bright light emitting diodes and lasers in the blue and ultra violet region [133]. Additionally, their band gaps (InN$\approx$0.7 meV [134], GaN=3.5 meV [135], AlN$\approx$6.1 meV [136]) cover a wide energy range including the whole visible spectrum. Also, their large excitonic binding energies combined with potentially large localization energies make

applications at elevated temperatures feasible. Indeed, a single photon emitter operating at 200 K based on GaN QDs in AlN matrix has already been demonstrated [137]. The electronic structure of such QDs is much less understood than their arsenide-based counterparts. First experiences on a single dot level have been made with InGaN/GaN [18, 56, 138, 139] and GaN/Al(Ga)N [140]. With increasing sample quality, more complex aspects of their electronic structure will be accessible for optical spectroscopy in the future.

In the end, besides gaining a deeper understanding of the underlying physics of nano-structures, the ultimate goal is to use this understanding to develop novel and innovative devices based on single QDs. Among them, single-photon emitters have reached a high level of development compared to, e.g., QD-based quantum computers. Still, some serious technological issues remain. One of the aims intensively pursued is to pre-determine the exact site prior to QD growth and build the device around this site, rather than cumbersomely having to locate a QD first. Several ideas exist to tackle this problem, for example site-selective growth via pre-patterned substrates using electron-beam lithography [45, 46], scanning-tunneling-probe-assisted lithography [47] atomic-force-microscope patterning [48] or induced by focused ion implantation [49]. Even 3-dimensional QD crystals can be created [141] along with good optical quality of the QDs [142]. For a recent review on lateral alignment of QDs see also [143]. It is completely unclear, however, in how far such techniques alter the QDs' electronic structure. This makes fundamental spectroscopic studies like the one at hand invaluable when it comes to optimization of device performance and functionality.

Appendix A

Derivation of Exchange Hamiltonian

In this chapter a step-by-step derivation of the matrix representation of the exchange Hamiltonian H^{ex} in the basis of the exciton and excited trion total-angular-momentum states is presented.

In order to simplify the discussion the concept of *pseudospin* will be introduced here. Pseudospin is a mathematical trick taking into account that a particle with two possible half-integer spin configurations from a wider spectrum physically behaves like a spin-$^1\!/_2$ particle. In our case the spin of the heavy holes is $\left|\pm\frac{3}{2}\right\rangle$. Since the light and split-off holes do not play a role when valence-band mixing is disregarded one simplifies the notation by assigning one configuration [here: (heavy) hole spin $\left|+\frac{3}{2}\right\rangle$] to the pseudospin state $\left|-\frac{1}{2}\right\rangle$ and the other [here: (heavy) hole spin $\left|-\frac{3}{2}\right\rangle$] to the pseudospin state $\left|+\frac{1}{2}\right\rangle$:

symbol	hole spin $\left|j_z\right\rangle$	pseudospin $\left|i_z\right\rangle$
$\left|\downarrow\right\rangle$	$\left|-\frac{3}{2}\right\rangle$	$\left|+\frac{1}{2}\right\rangle$
$\left|\uparrow\right\rangle$	$\left|+\frac{3}{2}\right\rangle$	$\left|-\frac{1}{2}\right\rangle$

Note, that the change in notation does not change the underlying physics of the problem.

The Hamiltonian as derived from the theory of invariants [62] then reads

$$H^{ex} = \underbrace{2\Delta_0 I_z S_z}_{H_0} + \underbrace{\Delta_1(I_x S_x - I_y S_y)}_{H_1} + \underbrace{\Delta_2(I_x S_x + I_y S_y)}_{H_2}, \qquad (A.1)$$

where $\mathbf{S}=(S_x, S_y, S_z)$ is the total electron spin, $\mathbf{I}=(I_x, I_y, I_z)$ is the total hole pseudospin and Δ_i are constants.

A.1 Exciton

In the case of an exciton the angular momentum operators from Eq. (A.1) are the spin operator for a single electron ($\mathbf{s}$) and the pseudospin operator for a single hole ($\mathbf{i}$). In order to find the matrix representation in the basis of the exciton total angular momentum $\mathbf{F}=\mathbf{s}+\mathbf{j}$ (or in the pseudospin picture $\mathbf{M}=\mathbf{s}+\mathbf{i}$) the occurring matrix elements have to be calculated. The following states need to be considered (left: in terms of exciton total-angular-momentum projection F_z, right: in terms of electron-spin projection s_z and hole-pseudospin projection i_z):

$$
\begin{aligned}
|F_z\rangle &= |s_z, i_z\rangle \\
|-2\rangle &= |-1/2, +1/2\rangle \\
|-1\rangle &= |+1/2, +1/2\rangle \\
|+1\rangle &= |-1/2, -1/2\rangle \\
|+2\rangle &= |+1/2, -1/2\rangle
\end{aligned}
\tag{A.2}
$$

In the basis of electron spins s_z (hole pseudospins i_z) the spin operators read [144]:

$$
\begin{aligned}
s_x/i_x &= \begin{pmatrix} 0 & 1/2 \\ 1/2 & 0 \end{pmatrix}, \\
s_y/i_y &= \begin{pmatrix} 0 & -i/2 \\ i/2 & 0 \end{pmatrix}, \\
s_z/i_z &= \begin{pmatrix} 1/2 & 0 \\ 0 & -1/2 \end{pmatrix}.
\end{aligned}
\tag{A.3}
$$

Now, the derivation of the matrix representation of H^{ex} is straightforward. In order to keep the calculation of the matrix elements $\langle F_z^i|H^{ex}|F_z^j\rangle$ simple, we will consider the three summands of Eq. (A.1) one after the other.

- H_0:

  We start by evaluating the matrix element $\langle \pm 1|H_0| \pm 1\rangle$:

  $$
  \begin{aligned}
  \langle \pm 1|H_0| \pm 1\rangle &= \langle \mp 1/2, \mp 1/2| \, 2\Delta_0 i_z s_z \, |\mp 1/2, \mp 1/2\rangle \\
  &= 2\Delta_0 \, \langle \mp 1/2| \, s_z \, |\mp 1/2\rangle \, \langle \mp 1/2| \, i_z \, |\mp 1/2\rangle \\
  &= 2\Delta_0 (\mp 1/2)(\mp 1/2) = \Delta_0/2.
  \end{aligned}
  $$

  Analogously we find

  $$
  \langle \pm 2|H_0| \pm 2\rangle = -\Delta_0/2.
  \tag{A.4}
  $$

  It is simple to verify, that all 12 off-diagonal elements (e.g. $\langle +1|H_0| + 2\rangle$) amount to zero because the off-diagonal terms of s_z and i_z are zero (Eq. A.3).

- H_1:

  The only two non-zero elements are

  $$
  \begin{aligned}
  \langle \mp 1 | H_0 | \pm 1 \rangle &= \Delta_1 \langle \pm 1/2, \pm 1/2 | \left(i_x s_x - i_y s_y \right) | \mp 1/2, \mp 1/2 \rangle \\
  &= \Delta_1 (1/2\ 1/2 - (\pm i/2)(\pm i/2)) = \Delta_1/2
  \end{aligned}
  $$

  Again it is simple to verify, that all other elements are 0.

- H_2:

  The only two non-zero elements are

  $$
  \begin{aligned}
  \langle \mp 2 | H_0 | \pm 2 \rangle &= \Delta_2 \langle \mp 1/2, \pm 1/2 | \left(i_x s_x + i_y s_y \right) | \mp 1/2, \pm 1/2 \rangle \\
  &= \Delta_2 (1/2\ 1/2 + (\mp i/2)(\pm i/2))) = \Delta_2/2.
  \end{aligned}
  $$

Adding up all three operators yields

$$
H^{ex} = \frac{1}{2}
\begin{pmatrix}
\Delta_0 & \Delta_1 & 0 & 0 \\
\Delta_1 & \Delta_0 & 0 & 0 \\
0 & 0 & -\Delta_0 & \Delta_2 \\
0 & 0 & \Delta_2 & -\Delta_0
\end{pmatrix}.
\tag{A.5}
$$

where rows and columns correspond to the (real) total-exciton-spin states $|+1\rangle$, $|-1\rangle$, $|+2\rangle$, and $|-2\rangle$.

A.2   Excited Trion

The case of the excited trion is quite analogous to the exciton case, albeit somewhat more complicated. Here three particles are involved, one electron and two holes. The procedure is equivalent to the case of two electrons and one hole (which is important to understand the XX^- resonances [74]) but we will stick to the former case, as it is the important one for this work.

Since the exchange interaction between two identical particles is stronger than between different particles the problem can be decomposed into different hierarchies: First the hole-hole interaction will be considered, then the interaction between the resulting two-hole complex and the electron.

The spin interaction between two spin-½ particles gives the singlet-triplet structure known from basic quantum mechanics. The corresponding spin states in terms of total pseudospin $\mathbf{I}$ and its projection I_z are $|0,0\rangle$ for the singlet and $|1,\pm1\rangle$ and $|1,0\rangle$ for the triplet. Together with the electron spin we receive the twofold degenerate states $\left|\frac{1}{2}, \pm\frac{1}{2}\right\rangle$ originating from the singlet and the sixfold degenerate states $\left|\frac{3}{2}, \pm\frac{3}{2}\right\rangle$, $\left|\frac{3}{2}, \pm\frac{1}{2}\right\rangle$, and $\left|\frac{1}{2}, \pm\frac{1}{2}\right\rangle$ originating from the triplet [Fig. 2.9 (b)].

symbol	single particle spin $\left|s_z, j_z^1, j_z^2\right\rangle$	total spin $\left|F_z\right\rangle$	single particle e-spin, h-pseudospin $\left|s, i_z^1, i_z^2\right\rangle$	total pseudospin $\left|M_z\right\rangle$
$\left|\uparrow, \Uparrow, \Uparrow\right\rangle$	$\left|\frac{1}{2}, \frac{3}{2}, \frac{3}{2}\right\rangle$	$\left|\frac{7}{2}\right\rangle_T$	$\left|\frac{1}{2}, -\frac{1}{2}, -\frac{1}{2}\right\rangle$	$\left|-\frac{1}{2}\right\rangle_T$
$\left|\downarrow, \Uparrow, \Uparrow\right\rangle$	$\left|-\frac{1}{2}, \frac{3}{2}, \frac{3}{2}\right\rangle$	$\left|\frac{5}{2}\right\rangle_T$	$\left|-\frac{1}{2}, -\frac{1}{2}, -\frac{1}{2}\right\rangle$	$\left|-\frac{3}{2}\right\rangle_T$
$\left|\uparrow, \Uparrow, \Downarrow\right\rangle + \left|\uparrow, \Downarrow, \Uparrow\right\rangle$	$\left|\frac{1}{2}, \frac{3}{2}, -\frac{3}{2}\right\rangle + \left|\frac{1}{2}, -\frac{3}{2}, \frac{3}{2}\right\rangle$	$\left|\frac{1}{2}\right\rangle_T$	$\left|\frac{1}{2}, -\frac{1}{2}, \frac{1}{2}\right\rangle + \left|\frac{1}{2}, \frac{1}{2}, -\frac{1}{2}\right\rangle$	$\left|\frac{1}{2}\right\rangle_T$
$\left|\uparrow, \Uparrow, \Downarrow\right\rangle - \left|\uparrow, \Downarrow, \Uparrow\right\rangle$	$\left|\frac{1}{2}, \frac{3}{2}, -\frac{3}{2}\right\rangle - \left|\frac{1}{2}, -\frac{3}{2}, \frac{3}{2}\right\rangle$	$\left|\frac{1}{2}\right\rangle_S$	$\left|\frac{1}{2}, -\frac{1}{2}, \frac{1}{2}\right\rangle - \left|\frac{1}{2}, \frac{1}{2}, -\frac{1}{2}\right\rangle$	$\left|\frac{1}{2}\right\rangle_S$

Table A.1: Four of the eight hot-trion spin states in different notations including pseudospin. The remaining four states are obtained by multiplying all spins of the shown states by -1.

For clarity all occurring energy states are summarized in Tab. A.1.

The operators from Eq. (A.1) now correspond to the spin operator for the single electron ($\mathbf{s}$) and the total pseudospin operator for the two holes ($\mathbf{I}$). For simplification we will focus on the hole triplet states only. Then the following states need to be considered (left: in terms of trion total angular momentum F_z, right: in terms of electron spin s_z and hole total pseudospin I_z):

$$
\begin{aligned}
\left|F_z\right\rangle &= \left|s_z, I_z\right\rangle \\
\left|\pm 1/2\right\rangle &= \left|\pm 1/2, 0\right\rangle \\
\left|\pm 5/2\right\rangle &= \left|\mp 1/2, \mp 1\right\rangle \\
\left|\pm 7/2\right\rangle &= \left|\pm 1/2, \mp 1\right\rangle
\end{aligned}
\tag{A.6}
$$

In the basis of the electron spin states s_z the operator $\mathbf{s}$ is identical to Eq. (A.3). $\mathbf{I}$, however, is a spin-1 operator. Its projection into the basis of i_z reads [144]:

$$
\begin{aligned}
I_x &= \begin{pmatrix} 0 & 1/\sqrt{2} & 0 \\ 1/\sqrt{2} & 0 & 1/\sqrt{2} \\ 0 & 1/\sqrt{2} & 0 \end{pmatrix}, \\
I_y &= \begin{pmatrix} 0 & -i/\sqrt{2} & 0 \\ i/\sqrt{2} & 0 & -i/\sqrt{2} \\ 0 & i/\sqrt{2} & 0 \end{pmatrix}, \\
I_z &= \begin{pmatrix} 1 & 0 & 0 \\ 0 & 0 & 0 \\ 0 & 0 & -1 \end{pmatrix}.
\end{aligned}
\tag{A.7}
$$

Again, we will evaluate the summands of H^{ex} [Eq. (A.1)] one after the other.

- H_0:

  Again we will restrain ourselves to evaluating the non-zero elements only:

  $$
  \begin{aligned}
  \langle \pm 5/2 | H_0 | \pm 5/2 \rangle &= 2\Delta_0 \langle \mp 1/2, \mp 1 | J_z s_z | \mp 1/2, \mp 1 \rangle \\
  &= 2\Delta_0 (\mp 1/2)(\mp 1) = \Delta_0
  \end{aligned}
  $$

  $$
  \begin{aligned}
  \langle \pm 7/2 | H_0 | \pm 7/2 \rangle &= 2\Delta_0 \langle \pm 1/2, \mp 1 | J_z s_z | \pm 1/2, \mp 1 \rangle \\
  &= 2\Delta_0 (\pm 1/2)(\mp 1) = -\Delta_0
  \end{aligned}
  $$

- H_1:

  $$
  \begin{aligned}
  \langle \pm 1/2 | H_1 | \pm 5/2 \rangle &= \Delta_1 \langle \pm 1/2, 0 | J_x s_x - J_y s_y | \mp 1/2, \mp 1 \rangle \\
  &= \Delta_1 (1/\sqrt{2})(1/2) - (\pm i/\sqrt{2})(\pm i/2) = \Delta_1/\sqrt{2}
  \end{aligned}
  $$

- H_2:

  $$
  \begin{aligned}
  \langle \pm 1/2 | H_2 | \mp 7/2 \rangle &= \Delta_2 \langle \pm 1/2, 0 | J_x s_x + J_y s_y | \mp 1/2, \pm 1 \rangle \\
  &= \Delta_2 (1/\sqrt{2})(1/2) + (\mp i/\sqrt{2})(\pm i/2) = \Delta_2/\sqrt{2}
  \end{aligned}
  $$

Adding up all three operators yields:

$$
H^{ex} = \begin{pmatrix}
0 & 0 & \Delta_1/\sqrt{2} & 0 & 0 & \Delta_2/\sqrt{2} \\
0 & 0 & 0 & \Delta_1/\sqrt{2} & \Delta_2/\sqrt{2} & 0 \\
\Delta_1/\sqrt{2} & 0 & \Delta_0 & 0 & 0 & 0 \\
0 & \Delta_1/\sqrt{2} & 0 & \Delta_0 & 0 & 0 \\
0 & \Delta_2/\sqrt{2} & 0 & 0 & -\Delta_0 & 0 \\
\Delta_2/\sqrt{2} & 0 & 0 & 0 & 0 & -\Delta_0
\end{pmatrix} \tag{A.8}
$$

where the rows and columns correspond to $F_z = \frac{1}{2}, -\frac{1}{2}, \frac{5}{2}, -\frac{5}{2}, \frac{7}{2}$ and $-\frac{7}{2}$ or, in a more concise way

$$
H^{ex} = \begin{pmatrix}
0 & \Delta_1/\sqrt{2} & \Delta_2/\sqrt{2} \\
\Delta_1/\sqrt{2} & \Delta_0 & 0 \\
\Delta_2/\sqrt{2} & 0 & -\Delta_0
\end{pmatrix} \tag{A.9}
$$

where the rows and columns correspond to $F_z = \pm\frac{1}{2}, \pm\frac{5}{2}$ and $\mp\frac{7}{2}$.

Appendix B

Proof of Kramers' Theorem

For convenience, the proof of Kramers' theorem as presented in the original (French) publication by H. A. Kramers [72] will be reproduced in this chapter.

We will start by proving a helpful Lemma:

Lemma If $\varphi(\mathbf{r})_{s_z^1,\ldots,s_z^k,\ldots,s_z^n}$, a function describing a system of n spin-$\frac{1}{2}$ particles with $s_z^k = \pm\frac{1}{2}$ the spin of the kth particle, is a solution to the Schrödinger equation, i.e.

$$\mathcal{H}\varphi(\mathbf{r})_{s_z^1,\ldots,s_z^k,\ldots,s_z^n} = E\varphi(\mathbf{r})_{s_z^1,\ldots,s_z^k,\ldots,s_z^n} \tag{B.1}$$

and no external magnetic fields are present, then a function

$$\varphi'(\mathbf{r})_{s_z^1,\ldots,s_z^k,\ldots,s_z^n} = (-1)^{\sum_k s_z^k - n/2}\varphi^*(\mathbf{r})_{-s_z^1,\ldots,-s_z^k,\ldots,-s_z^n} \tag{B.2}$$

exists that solves the Schrödinger equation for the same eigenvalue E.

Proof The spin operator $\mathbf{s}^k$ that acts on the spin of the kth particle can be written as $\mathbf{s}^k = \frac{\hbar}{2}\sigma^k$ where $\sigma_x^k, \sigma_y^k, \sigma_z^k$ are the Pauli matrices with

$$\sigma_x^k = \begin{pmatrix} 0 & 1 \\ 1 & 0 \end{pmatrix}, \sigma_y^k = \begin{pmatrix} 0 & -i \\ i & 0 \end{pmatrix}, \sigma_z^k = \begin{pmatrix} 1 & 0 \\ 0 & 1 \end{pmatrix}. \tag{B.3}$$

They act on the spins of the kth electron in the following way:

$$\begin{aligned}
\sigma_x^k \varphi_{s_z^1,\ldots,s_z^k,\ldots,s_z^n} &= \varphi_{s_z^1,\ldots,-s_z^k,\ldots,s_z^n} \\
\sigma_y^k \varphi_{s_z^1,\ldots,s_z^k,\ldots,s_z^n} &= -i(-1)^{s_k-\frac{1}{2}}\varphi_{s_z^1,\ldots,-s_z^k,\ldots,s_z^n} \\
\sigma_z^k \varphi_{s_z^1,\ldots,s_z^k,\ldots,s_z^n} &= (-1)^{s_k-\frac{1}{2}}\varphi_{s_z^1,\ldots,s_z^k,\ldots,s_z^n}
\end{aligned} \tag{B.4}$$

Let $\mathcal{H}(\mathbf{r}, \mathbf{p}, \sigma_x, \sigma_y, \sigma_z)$ be the Hamiltonian of the system and $\varphi_{s_z^k} \equiv \varphi(\mathbf{r})_{s_z^1,\ldots,s_z^k,\ldots,s_z^n}$ be and eigenfunction of $\mathcal{H}$, i.e.

$$\mathcal{H}(\mathbf{r}, \mathbf{p}, \sigma_x, \sigma_y, \sigma_z)\varphi_{s_z^k} = E\varphi_{s_z^k}. \tag{B.5}$$

If we take the complex conjugate of (B.5) we obtain

$$\mathcal{H}^*(\mathbf{r}, \mathbf{p}, \sigma_x, \sigma_y, \sigma_z)\varphi_{s_z^k}^* = E\varphi_{s_z^k}^*. \tag{B.6}$$

Since the momentum operator is $\mathbf{p} = -i\hbar\nabla$ the imaginary part of $\mathcal{H}$ is composed of $\mathbf{p}$ and σ_y. Therefore,

$$\mathcal{H}^*(\mathbf{r}, \mathbf{p}, \sigma_x, \sigma_y, \sigma_z) = \mathcal{H}(\mathbf{r}, -\mathbf{p}, \sigma_x, -\sigma_y, \sigma_z) \tag{B.7}$$

In the absence of external magnetic fields $\mathbf{p}$ enters the Hamiltonian in two parts: one is the kinetic energy $\frac{\mathbf{p}^2}{2m}$, the other is the spin-orbit interaction $\mathbf{L}\cdot\mathbf{s} = (\mathbf{r}\times\mathbf{p})\cdot\mathbf{s}$. Consequently,

$$\mathcal{H}^*(\mathbf{r}, \mathbf{p}, \sigma_x, \sigma_y, \sigma_z) = \mathcal{H}(\mathbf{r}, \mathbf{p}, -\sigma_x, \sigma_y, -\sigma_z) \tag{B.8}$$

and, together with (B.6)

$$\mathcal{H}(\mathbf{r}, \mathbf{p}, -\sigma_x, \sigma_y, -\sigma_z)\varphi_{s_z^k}^* = E\varphi_{s_z^k}^*. \tag{B.9}$$

We now introduce the function φ'' with

$$\varphi_{s_z^k}'' = \varphi_{-s_z^k}^*. \tag{B.10}$$

(B.9) now reads[1]

$$\mathcal{H}(\mathbf{r}, \mathbf{p}, -\sigma_x, -\sigma_y, \sigma_z)\varphi_{s_z^k}'' = E\varphi_{s_z^k}''. \tag{B.11}$$

We now introduce the function φ' with

$$\varphi_{s_z^k}' = (-1)^{\sum_k s_z^k - \frac{n}{2}}\varphi_{s_z^k}''. \tag{B.12}$$

Together with (B.4) one can easily verify that σ_x, σ_y, σ_z act on φ'' the same way as $-\sigma_x$, $-\sigma_y$, σ_z act on φ'. Consequently, from (B.11) we obtain

$$\mathcal{H}(\mathbf{r}, \mathbf{p}, \sigma_x, \sigma_y, \sigma_z)\varphi_{s_z^k}' = E\varphi_{s_z^k}' \tag{B.13}$$

which proves the Lemma.

The Lemma shows that we will always find a second eigenfunction of the Hamiltonian when no magnetic fields are present. This does not necessarily imply degeneracy since the two wave functions may well be linearly dependent, i.e. they merely vary by a constant factor. We will now check under which circumstances such a factor a can be found:

$$\varphi_{s_z^k}' = (-1)^{\sum_k s_z^k - \frac{n}{2}}\varphi_{-s_z^k}^* = a\varphi_{s_z^k} \tag{B.14}$$

---

[1]This can easily be verified when introducing the spinor notation where $|s_z\rangle$ is written as a two-dimensional vector with $|+1/2\rangle = \begin{pmatrix} 1 \\ 0 \end{pmatrix}$ and $|-1/2\rangle = \begin{pmatrix} 0 \\ 1 \end{pmatrix}$ and multiplying with the Pauli matrices.

By taking the complex conjugate and replacing s_z^k with $-s_z^k$ we obtain:

$$(-1)^{-\sum_k s_z^k - \frac{n}{2}} \varphi_{s_z^k} = a^* \varphi_{-s_z^k}^* = a^* a (-1)^{-\sum_k s_z^k + \frac{n}{2}} \varphi_{s_z^k}. \tag{B.15}$$

Consequently

$$a^* a = (-1)^n. \tag{B.16}$$

Obviously, this condition can only be fulfilled if n is even. If n is uneven no constant factor a exists that would render φ and φ' linearly dependent. The energy states of a system of an uneven number of spin-$\frac{1}{2}$ particles are therefore degenerate under the absence of magnetic fields, q.e.d.

For a more elaborate discussion of Kramers' theorem and a discussion of the consequences for magnetic fields see the original publication by Kramers [72] or a nice publication by M. J. Klein [73] which also includes an alternative proof for the theorem.

Proof of Kramers' Theorem

Appendix C

Experimental Determination of Decay Times

The limited intensity of the transition lines of excitonic complexes in single quantum dots (QDs) combined with the general lack of efficient *and* fast detectors in the near infra-red make a compromise in the detector choice necessary. Here, a Perkin Ellmer SPCM-AQR-13 avalanche photo diode was employed that has the highest photon detection efficiency at 900 nm available (34 %) but a broad instrument response function (IRF) of 350 ps [89]. Additionally, the IRF is not constant when the detection wavelength is changed. The dependency is weak on the order of 50 meV and was therefore neglected when comparing different excitonic complexes and different QDs. However, it raises a problem when measuring the IRF of the complete setup. Other than in time-resolved photoluminescence setups where the exciting laser pulse can be used to measure the system's IRF in cathodoluminescence a sample is needed that converts the primary electron pulse into an optical pulse on a time scale well below the expected IRF of the system. No sample was available that showed a fast enough decay (≤ 100 ps) and luminescence near 900 nm at the same time.

The influence of the IRF was accounted for in the following way: Numerical calculations showed, that an idealized decay consisting of a mono-exponential transient with a decay time τ and a preceding plateau convoluted with a Gaussian with a full-width at half maximum σ regains its original mono-exponential shape after a time that depends on both τ and σ. For realistic values of τ and σ the decay is always mono-exponential after the signal has dropped to 50 % of its original value (see Fig. C.1).

The actual transients have been analyzed in the following way: First the offset originating from the dark counts of the APD was determined by averaging over data points immediately before the onset of the pulse where the system is fully relaxed. This offset was subtracted from the transient and the decay times were determined
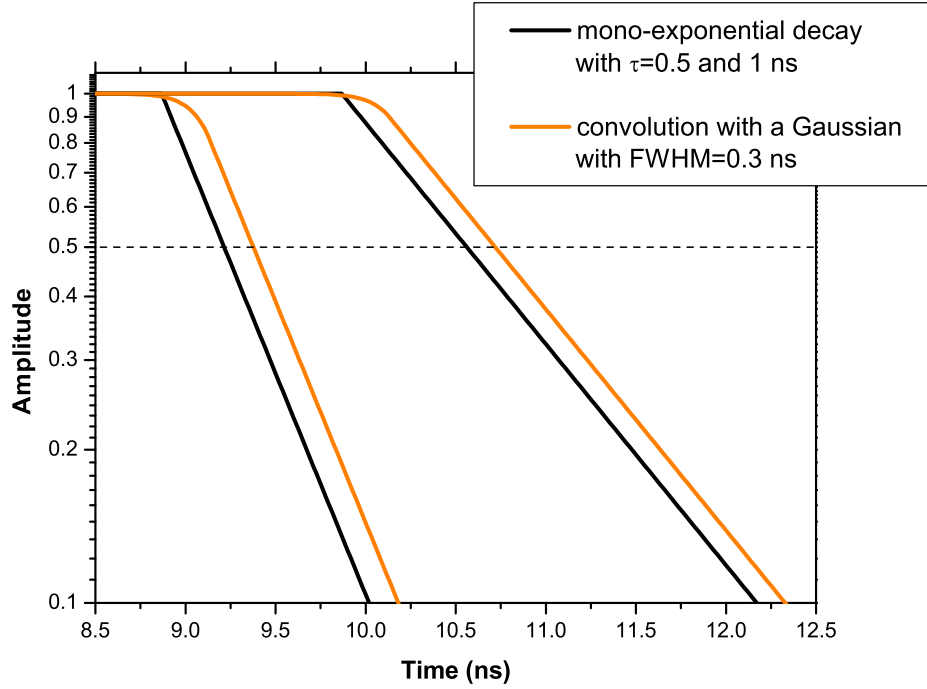
Figure C.1: Theoretical curves of a monoexponential decay with preceding plateau for $\tau = 0.5$ and 1 ns and convolution of the curves with a Gaussian with a FWHM of 0.3 ns. After the intensity has dropped to 50 % or more, the influence of the Gaussian is negligible original shape is recovered.

by fitting the corrected transient starting at the time where the signal has dropped to 50 % where the influence of the IRF and the plateau is weak (see Fig. C.2). Then the fitting range was altered in small steps until the obtained decay times did not systematically change with the chosen fitting range any more. The error made this way is estimated to ±100 ps. Transients with low signal-to-noise ratio or transients consisting of two exponential decays have been assigned a larger error of ±200 ps.
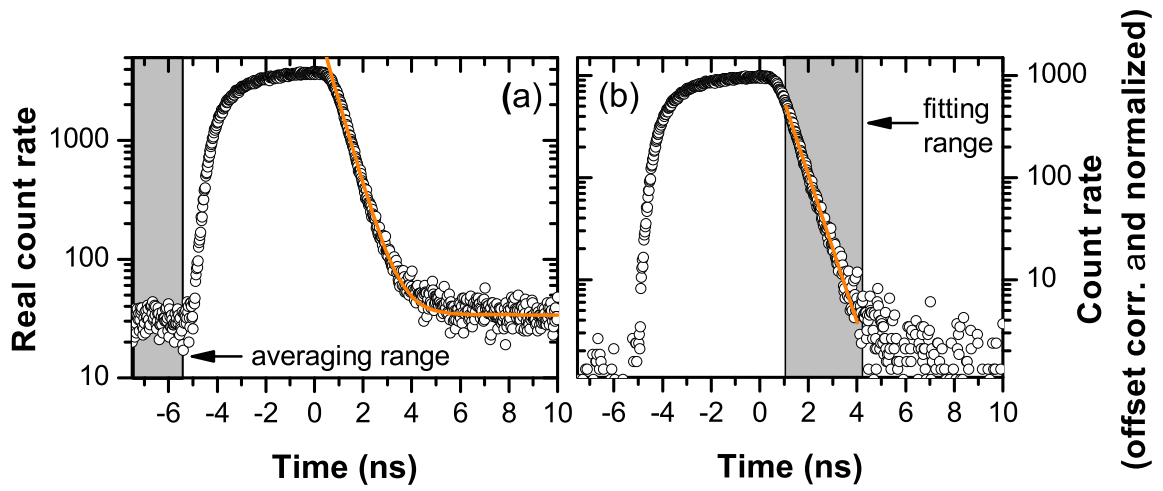
Figure C.2: Sample transient to illustrate the determination of the decay times. (a) Original transient. (b) Transient after the offset was subtracted. The grey shaded areas indicate the region where (a) the offset from the dark counts was deduced and (b) the monoexponential fit was carried out. The orange lines give the obtained fits.

Bibliography

[1] D. Bimberg, M. Grundmann, and N. N. Ledentsov, *Quantum Dot Hetrostructures* (John Wiley & Sons, Chichester, 1999).

[2] M. Grundmann, *Nano- Optoelectronics*, NanoScience and Technology (Springer-Verlag, Berlin Heidelberg, 2002).

[3] D. J. Mowbray and M. S. Skolnick, *Journal of Physics D: Applied Physics* **38**, 2059 (2005).

[4] R. Dingle and C. Henry, *Quantum effects in heterostructure lasers* (U.S. Patent No. 3982207, 1976).

[5] N. Kirstaedter, N. N. Ledentsov, M. Grundmann, D. Bimberg, V. M. Ustinov, S. S. Ruvimov, M. V. Maximov, P. S. Kop'ev, Z. I. Alferov, U. Richter, P. Werner, U. Gösele, and J. Heydenreich, *Electronics Letters* **30**, 1416 (1994).

[6] G. T. Liu, A. Stintz, H. Li, K. J. Malloy, and L. F. Lester, *Electronics Letters* **35**, 1163 (1999).

[7] M. Lämmlin, G. Fiol, C. Meuer, M. Kuntz, F. Hopfer, A. R. Kovsh, N. N. Ledentsov, and D. Bimberg, *Electronics Letters* **42**, 41 (2006).

[8] A. Marent, M. Geller, D. Bimberg, A. P. Vasi'ev, E. S. Semenova, A. E. Zhukov, and V. M. Ustinov, *Applied Physics Letters* **89**, 072103 (2006).

[9] P. Michler, A. Kiraz, C. Becher, W. V. Schoenfeld, P. M. Petroff, L. Zhang, E. Hu, and A. Imamoglu, *Science* **290**, 2282 (2000).

[10] C. Santori, M. Pelton, G. Solomon, Y. Dale, and Y. Yamamoto, *Physical Review Letters* **86**, 1502 (2001).

[11] A. Lochmann, E. Stock, O. Schulz, F. Hopfer, D. Bimberg, V. Haisler, A. Toropov, A. Bakarov, and A. Kalagin, *Electronics Letters* **42**, 774 (2006).

[12] E. Knill, R. Laflamme, and G. J. Milburn, *Nature* **409**, 46 (2001).

[13] J. Y. Marzin, J.-M. Gérard, A. Izraël, D. Barrier, and G. Bastard, *Physical Review Letters* **73**, 716 (1994).

[14] M. Grundmann, J. Christen, N. N. Ledentsov, J. Böhrer, D. Bimberg, S. S. Ruvimov, P. Werner, U. Richter, U. Gösele, J. Heydenreich, V. M. Ustinov, A. Y. Egorov, A. E. Zhukov, P. S. Kop'ev, and Z. I. Alferov, *Physical Review Letters* **74**, 4043 (1995).

[15] D. Hessman, P. Castrillo, M.-E. Pistol, C. Pryor, and L. Samuelson, *Applied Physics Letters* **69**, 749 (1996).

[16] S. Rodt, A. Schliwa, K. Pötschke, F. Guffarth, and D. Bimberg, *Physical Review B* **71**, 155325 (2005).

[17] V. Türck, S. Rodt, O. Stier, R. Heitz, R. Engelhardt, U. W. Pohl, D. Bimberg, and R. Steingrüber, *Physical Review B* **61**, 9944 (2000).

[18] R. Seguin, S. Rodt, A. Strittmatter, L. Reißmann, T. Bartel, A. Hoffmann, D. Bimberg, E. Hahn, and D. Gerthsen, *Applied Physics Letters* **84**, 4023 (2004).

[19] M. Ediger, G. Bester, A. Badolato, P. M. Petroff, K. Karrai, A. Zunger, and R. J. Warburton, *Nature Physics* **3**, 774 (2007).

[20] D. Gammon, E. S. Snow, B. V. Shanabrook, D. S. Katzer, and D. Park, *Physical Review Letters* **76**, 3005 (1996).

[21] M. Bayer, A. Kuther, A. Forchel, A. A. Gorbunov, V. B. Timofeev, F. Schäfer, and J. P. Reithmaier, *Physical Review Letters* **82**, 1748 (1999).

[22] M. Bayer, G. Ortner, O. Stern, A. Kuther, A. A. Gorbunov, A. Forchel, P. Hawrylak, S. Fafard, K. Hinzer, T. L. Reinecke, S. N. Walck, J. P. Reithmaier, F. Klopf, and F. Schäfer, *Physical Review B* **65**, 195315 (2002).

[23] O. Benson, C. Santori, M. Pelton, and Y. Yamamoto, *Physical Review Letters* **84**, 2513 (2000).

[24] N. Gisin, R. Grégoire, G. Tittel, and H. Zbinden, *Reviews of Modern Physics* **74**, 145 (2002).

[25] C. Gobby, Z. L. Yuan, and A. J. Shields, *Electronics Letters* **40**, 1603 (2004).

[26] A. S. Lenihan, M. V. Gurudev Dutt, D. G. Steel, S. Ghosh, and P. K. Bhattacharya, *Physical Review Letters* **88**, 223601 (2002).

[27] J. J. Finley, D. J. Mowbray, M. S. Skolnick, A. D. Ashmore, C. Baker, A. F. G. Monte, and M. Hopkinson, *Physical Review B* **66**, 153316 (2002).

[28] A. I. Tartakovskii, M. N. Makhonin, I. R. Sellers, J. Cahill, A. D. Andreev, D. M. Whittaker, J.-P. R. Wells, A. M. Fox, D. J. Mowbray, M. S. Skolnick, K. M. Groom, M. J. Steer, H. Y. Liu, and M. Hopkinson, *Physical Review B* **70**, 193303 (2004).

[29] K. Kowalik, O. Krebs, A. Lemaître, S. Laurent, P. Senellart, P. Voisin, and J. A. Gaj, *Applied Physics Letters* **86**, 041907 (2005).

[30] A. J. Shields, *Nature Photonics* **1**, 215 (2007).

[31] G. Wang, S. Fafard, D. Leonard, J. E. Bowers, J. L. Merz, and P. M. Petroff, *Applied Physics Letters* **64**, 2815 (1994).

[32] U. Bockelmann, W. Heller, A. Filoramo, and P. Roussignol, *Physical Review B* **55**, 4456 (1996).

[33] G. Bacher, R. Weigand, J. Seufert, V. D. Kulakovskii, N. A. Gippius, A. Forchel, K. Leonardi, and D. Hommel, *Physical Review Letters* **83**, 4417 (1999).

[34] V. Zwiller, M.-E. Pistol, D. Hessman, R. Cederstrom, W. Seifert, and L. Samuelson, *Physical Review B* **59**, 5021 (1999).

[35] E. Dekel, D. V. Regelman, D. Gershoni, E. Ehrenfreund, W. V. Schoenfeld, and P. M. Petroff, *Physical Review B* **62**, 11038 (2000).

[36] C. Santori, D. Fattal, M. Pelton, G. S. Solomon, and Y. Yamamoto, *Physical Review B* **66**, 045308 (2002).

[37] R. M. Thompson, R. M. Stevenson, A. J. Shields, I. Farrer, C. J. Lobo, D. A. Ritchie, M. L. Leadbeater, and M. Pepper, *Physical Review B* **64**, 201302 (2001).

[38] S. Kono, A. Kirihara, A. Tomita, K. Nakamura, J. Fujikata, K. Ohashi, H. Saito, and K. Nishi, *Physical Review B* **72**, 155307 (2005).

[39] M. H. Baier, A. Malko, E. Pelucchi, D. Y. Oberli, and E. Kapon, *Physical Review B* **73**, 205321 (2006).

[40] P. A. Dalgarno, J. McFarlane, B. D. Gerardot, R. J. Warburton, K. Karrai, A. Badolato, and P. M. Petroff, *Applied Physics Letters* **89**, 043107 (2006).

[41] J. Márquez, L. Geelhaar, and K. Jacobi, *Applied Physics Letters* **78**, 2309 (2007).

[42] B. Alloing, C. Zinoni, V. Zwiller, L. H. Li, C. Monat, M. Gobet, G. Buchs, A. Fiore, E. Pelucchi, and E. Kapon, *Applied Physics Letters* **86**, 101908 (2005).

[43] M. B. Ward, O. Z. Karimov, D. C. Unitt, Z. L. Yuan, P. See, D. G. Gevaux, A. J. Shields, P. Atkinson, and D. A. Ritchie, *Applied Physics Letters* **86**, 201111 (2005).

[44] B. Alloing, C. Zinoni, L. H. Li, A. Fiore, and G. Patriarche, *Journal of Applied Physics* **101**, 024918 (2007).

[45] T. Ishikawa, S. Kohmoto, and K. Asakawa, *Applied Physics Letters* **73**, 1712 (1998).

[46] P. Atkinson, M. B. Ward, S. P. Bremner, D. Anderson, T. Farrow, G. A. C. Jones, A. J. Shields, and D. A. Ritchie, *Physica E* **32**, 21 (2006).

[47] S. Kohmoto, H. Nakamura, T. Ishikawa, and K. Asakawa, *Applied Physics Letters* **75**, 3488 (1999).

[48] C. K. Hyon, S. C. Choi, S.-H. Song, S. W. Hwang, M. H. Son, D. Ahn, Y. J. Park, and E. K. Kim, *Applied Physics Letters* **77**, 2607 (2000).

[49] M. Mehta, D. Reuter, A. Melnikov, A. Wieck, and A. Remhof, *Applied Physics Letters* **91**, 123108 (2007).

[50] A. R. Kovsh, N. A. Maleev, A. E. Zhukov, S. S. Mikhrin, A. R. Vasil'ev, Y. M. Shemyakov, M. V. Maximov, D. A. Livshits, V. M. Ustinov, Z. I. Alferov, N. N. Ledentsov, and D. Bimberg, *Electronics Letters* **38**, 1104 (2002).

[51] M. Grundmann, O. Stier, and D. Bimberg, *Physical Review B* **52**, 11969 (1995).

[52] C. F. Klingshirn, *Semiconductor Optics* (Springer Verlag, Berlin, 1997).

[53] *Landolt-Börnstein* (Springer Verlag, Berlin, 1982).

[54] O. Stier, M. Grundmann, and D. Bimberg, *Physical Review B* **59**, 5688 (1999).

[55] T. Bretagnon, S. Kalliakos, P. Lefebvre, P. Valvin, B. Gil, N. Grandjean, A. Dussaigne, B. Damilano, and J. Massies, *Physical Review B* **68**, 205301 (2003).

[56] M. Winkelnkemper, R. Seguin, S. Rodt, A. Schliwa, L. Reissmann, A. Strittmatter, A. Hoffmann, and D. Bimberg, *Journal of Applied Physics* **101**, 113708 (2007).

[57] O. Stier, *Electronic and Optical Properties of Quantum Dots and Wires*, Ph.D. thesis, Technische Universität Berlin (2000).

[58] A. Schliwa, *Electronic Properties of Self-Organized Quantum Dots*, Ph.D. thesis, Technische Universität Berlin (2007).

[59] A. Schliwa, M. Winkelnkemper, and D. Bimberg, *Physical Review B* **76**, 205324 (2007).

[60] G. Bester, X. Wu, D. Vanderbilt, and A. Zunger, *Physical Review Letters* **96**, 187602 (2006).

[61] G. Bester, A. Zunger, X. Wu, and D. Vanderbilt, *Physical Review B* **74**, 081305 (2006).

[62] E. L. Ivchenko and G. Pikus, *Superlattices and Other Heterostructures* (Springer Verlag, Berlin, 1995).

[63] G. Bester, S. Nair, and A. Zunger, *Physical Review B* **67**, 161306 (2003).

[64] G. Bester and A. Zunger, *Physical Review B* **71**, 045318 (2005).

[65] W. Langbein, P. Borri, U. Woggon, V. Stavarache, D. Reuter, and A. Wieck, *Physical Review B* **69**, 161301 (2004).

[66] A. Högele, S. Seidl, M. Kroner, K. Karrai, R. J. Warburton, B. D. Gerardot, and P. M. Petroff, *Physical Review Letters* **93**, 217401 (2004).

[67] C. H. Bennett and G. Brassard, *Proceedings of the IEEE International Conference on Computers, Systems and Signal Processing, Bangalore, India, (IEEE, New York)* 175 (1984).

[68] D. Bouwmeester, A. Ekert, and A. Zeilinger, *The Physics of Quantum Information* (Springer Verlag, Berlin, 2000).

[69] N. Akopian, N. H. Lindner, E. Poem, Y. Berlatzky, J. Avron, D. Gershoni, B. D. Gerardot, and P. M. Petroff, *Physical Review Letters* **96**, 130501 (2006).

[70] R. M. Stevenson, R. J. Young, P. Atkinson, K. Cooper, D. A. Ritchie, and A. J. Shields, *Nature* **439**, 179 (2006).

[71] L. D. Landau and E. M. Lifschitz, *Lehrbuch der theoretischen Physik*, volume 3: Quantenmechanik (Akademie Verlag, Berlin, 1988).

[72] H. Kramers, *Proc. Amst. Acad.* **33**, 959 (1930).

[73] M. J. Klein, *American Journal of Physics* **20**, 65 (1952).

[74] I. A. Akimov, K. V. Kavokin, A. Hundt, and F. Henneberger, *Physical Review B* **71**, 075326 (2005).

[75] K. V. Kavokin, *physica status solidi (a)* **195**, 592 (2003).

[76] J. Puls, M. Rabe, H.-J. Wünsche, and F. Henneberger, *Physical Review B* **60**, 16303 (1999).

[77] M. Ediger, G. Bester, B. D. Gerardot, A. Badolato, P. M. Petroff, K. Karrai, A. Zunger, and R. J. Warburton, *Physical Review Letters* **98**, 036808 (2007).

[78] D. A. B. Miller, D. S. Chemla, T. C. Damen, A. C. Gossard, W. Wiegmann, T. H. Wood, and C. A. Burrus, *Physical Review Letters* **53**, 2173 (1985).

[79] M. Bayer and A. Forchel, *Physical Review B* **65**, 041308 (2002).

[80] P. Borri, W. Langbein, U. Woggon, V. Stavarache, D. Reuter, and A. D. Wieck, *Physical Review B* **71**, 115328 (2005).

[81] M. Krahl, *Vom GaAs Quantum Well zum GaAs Übergitter: Einfluss der Kopplung von Quantentöpfen auf spontane Emissionsprofile, Verstärkungsprofile und spontane Rekombinationskoeffizienten*, Ph.D. thesis, Technische Universität Berlin (1990).

[82] G. W. 't Hooft, W. A. J. A. van der Poel, L. W. Molenkamp, and C. T. Foxon, *Physical Review B* **35**, 8281 (1987).

[83] G. A. Narvaez, G. Bester, and A. Zunger, *Physical Review B* **72**, 245318 (2005).

[84] D. W. Pohl, W. Denk, and M. Lanz, *Applied Physics Letters* **44**, 651 (1984).

[85] J. Christen, M. Grundmann, and D. Bimberg, *Journal of Vacuum Science and Technology* **9**, 2358 (1991).

[86] B. G. Yacobi and D. B. Holt, *Journal of Applied Physics* **59**, R1 (1986).

[87] V. Türck, *Elektronische Eigenschaften einzelner Halbleiterquantenpunkte*, Ph.D. thesis, Technische Universität Berlin (2001).

[88] J. Christen, *Bestimmung der atomaren Morphologie von GaAs/AlGaAs-Heterogrenzflächen mittels Lumineszenzuntersuchungen*, Ph.D. thesis, Technische Universität Berlin (1988).

[89] W. Becker and A. Bergmann, *Detectors for High-Speed Photon Counting* (Application Notes from Becker & Hickl GmbH, Berlin).

[90] U. W. Pohl, K. Pötschke, A. Schliwa, F. Guffarth, D. Bimberg, N. D. Zakharov, P. Werner, M. B. Lifshits, V. A. Shchukin, and D. E. Jesson, *Physical Review B* **72**, 245332 (2005).

[91] M. B. Lifshits, V. A. Shchukin, D. Bimberg, and D. E. Jesson, *Proceedings of the 13th Int. Symp. "Nanostructures: Physics and Technology", St. Petersburg, Russia* 308 (June 20-25, 2005).

[92] H. Yu, H. Htoon, A. deLozanne, C. K. Shih, P. A. Grudowski, R. D. Dupuis, K. Zeng, R. Mair, J. Y. Lin, and H. X. Jiang, *Journal of Vacuum Science and Technology B* **16**, 2215 (1998).

[93] R. D. Grober, D. Rutherford, and T. D. Harris, *Applied Optics* **35**, 3488 (1996).

[94] S. A. Empedocles, D. J. Norris, and M. G. Bawendi, *Physical Review Letters* **77**, 3873 (1996).

[95] M.-E. Pistol, P. Castrillo, D. Hessman, J. A. Prieto, and L. Samuelson, *Physical Review B* **59**, 10725 (1999).

[96] H. D. Robinson and B. B. Goldberg, *Physical Review B* **61**, R5086 (2000).

[97] E. Stock, T. Warming, R. Seguin, S. Rodt, K. Pötschke, and D. Bimberg, in *Spring Meeting of the German Physical Society* (Dresden, 2006).

[98] T. Müller, F. F. Schrey, G. Strasser, and K. Unterrainer, *Applied Physics Letters* **83**, 3572 (2003).

[99] M. Geller, A. Marent, E. Stock, D. Bimberg, V. I. Zubkov, I. S. Shulgunova, and A. V. Solomonov, *Applied Physics Letters* **89**, 232105 (2006).

[100] B. Urbaszek, R. J. Warburton, K. Karrai, B. D. Gerardot, P. M. Petroff, and J. M. Garcia, *Physical Review Letters* **90**, 247403 (2003).

[101] N. I. Cade, H. Gotoh, H. Kamada, H. Nakano, and H. Okamoto, *Physical Review B* **73**, 115322 (2006).

[102] K. Nishi, H. Saito, S. Sugou, and J.-S. Lee, *Applied Physics Letters* **74**, 1111 (1999).

[103] J. Tatebayashi, M. Nishioka, and Y. Arakawa, *Applied Physics Letters* **78**, 3469 (2001).

[104] R. Heitz, F. Guffarth, K. Pötschke, A. Schliwa, D. Bimberg, N. D. Zakharov, and P. Werner, *Physical Review B* **71**, 045325 (2005).

[105] A. Schliwa, private communication.

[106] A. K. Ekert, *Physical Review Letters* **67**, 661 (1991).

[107] A. K. Ekert, J. G. Rarity, P. R. Tapster, and G. Massimo Palma, *Physical Review Letters* **69**, 1293 (1992).

[108] R. J. Young, R. M. Stevenson, A. J. Shields, P. Atkinson, K. Cooper, D. A. Ritchie, K. M. Groom, A. I. Tartakovskii, and M. S. Skolnick, *Physical Review B* **72**, 113305 (2005).

[109] S. Adachi, *Physical properties of III-V semiconductor compounds* (John Wiley & Sons, New York, 1990).

[110] R. A. Hogg, T. A. Fisher, A. R. K. Willcox, D. M. Whittaker, M. S. Skolnick, D. J. Mowbray, J. P. R. David, A. S. Pabla, G. J. Rees, R. Grey, J. Woodhead, J. L. Sánchez-Rojas, G. Hill, M. A. Pate, and P. N. Robson, *Physical Review B* **48**, 8491 (1993).

[111] J. L. Sánchez-Rojas, A. Sacedón, F. González-Sanz, E. Cajella, and E. Munoz, *Applied Physics Letters* **65**, 2042 (1994).

[112] C. H. Chan, M. C. Chen, H. H. Lin, Y. F. Chen, G. J. Jan, and Y. H. Chen, *Applied Physics Letters* **72**, 1208 (1998).

[113] S. Cho, J. Kim, A. Sanz-Hervás, A. Majerfield, G. Patriarche, and B. W. Kim, *physica status solidi (a)* **195**, 260 (2003).

[114] R. M. Stevenson, R. M. Thompson, A. J. Shields, I. Farrer, B. E. Kardynal, D. A. Ritchie, and M. Pepper, *Physical Review B* **66**, 081302 (2002).

[115] M. M. Vogel, S. M. Ulrich, R. Hafenbrak, P. Michler, L. Wang, A. Rastelli, and O. G. Schmidt, *Applied Physics Letters* **91**, 051904 (2007).

[116] R. M. Stevenson, R. J. Young, P. See, D. G. Gevaux, K. Cooper, P. Atkinson, I. Farrer, D. A. Ritchie, and A. J. Shields, *Physical Review B* **73**, 033306 (2006).

[117] S. Seidl, M. Kroner, A. Hogele, K. Karrai, R. J. Warburton, A. Badolato, and P. M. Petroff, *Applied Physics Letters* **88**, 203113 (2006).

[118] K.-H. Goetz, D. Bimberg, H. Jurgensen, J. Selders, A. V. Solomonov, G. F. Glinskii, and M. Razeghi, *Journal of Applied Physics* **54**, 4543 (1983).

[119] D. J. P. Ellis, R. M. Stevenson, R. J. Young, A. J. Shields, P. Atkinson, and D. A. Ritchie, *Applied Physics Letters* **90**, 011907 (2007).

[120] A. Rastelli, A. Ulhaq, S. Kiravittaya, L. Wang, A. Zrenner, and O. G. Schmidt, *Applied Physics Letters* **90**, 073120 (2007).

[121] J. M. Smith, P. A. Dalgarno, R. J. Warburton, A. O. Govorov, K. Karrai, B. D. Gerardot, and P. M. Petroff, *Physical Review Letters* **94**, 197402 (2005).

[122] S. Rodt, V. Turck, R. Heitz, F. Guffarth, R. Engelhardt, U. W. Pohl, M. Strassburg, M. Dworzak, A. Hoffmann, and D. Bimberg, *Physical Review B* **67**, 235327 (2003).

[123] A. S. Shkolnik, L. Y. Karachinsky, N. Y. Gordeev, G. G. Zegrya, V. P. Evtikhiev, S. Pellegrini, and G. S. Buller, *Applied Physics Letters* **86**, 211112 (2005).

[124] R. J. Warburton, C. Schäflein, D. Haft, F. Bickel, A. Lorke, K. Karrai, J. M. Garcia, W. Schoenfeld, and P. M. Petroff, *Nature* **405**, 926 (2000).

[125] F. Hopfer, A. Mutig, M. Kuntz, G. Fiol, D. Bimberg, N. N. Ledentsov, V. A. Shchukin, S. S. Mikhrin, D. L. Livshits, I. L. Krestnikov, A. R. Kovsh, N. D. Zakharov, and P. Werner, *Applied Physics Letters* **89**, 141106 (2006).

[126] H. J. Krenner, M. Sabathil, E. C. Clark, A. Kress, D. Schuh, M. Bichler, G. Abstreiter, and J. J. Finley, *Physical Review Letters* **94**, 057402 (2005).

[127] H. J. Krenner, E. C. Clark, T. Nakaoka, M. Bichler, C. Scheurer, G. Abstreiter, and J. J. Finley, *Physical Review Letters* **97**, 076403 (2006).

[128] E. A. Stinaff, M. Scheibner, A. S. Bracker, I. V. Ponomarev, V. L. Korenev, M. E. Ware, M. F. Doty, T. L. Reinecke, and D. Gammon, *Science* **311**, 636 (2006).

[129] R. Songmuang, S. Kiravittaya, and O. G. Schmidt, *Applied Physics Letters* **82**, 2892 (2003).

[130] L. Wang, A. Rastelli, S. Kiravittaya, R. Songmuang, O. G. Schmidt, B. Krause, and T. H. Metzger, *Nanoscale Research Letters* **1**, 74 (2006).

[131] H. Born, A. R. Goñi, R. Heitz, A. Hoffmann, C. Thomsen, F. Heinrichsdorff, and D. Bimberg, *physica status solidi (b)* **215**, 313 (1999).

[132] T. Nakaoka, T. Saito, J. Tatebayashi, and Y. Arakawa, *Physical Review B* **70**, 235337 (2004).

[133] S. Nakamura and G. Fasol, *The Blue Laser Diode* (Springer Verlag, Berlin, 2000).

[134] J. Wu, W. Walukiewicz, K. M. Yu, J. W. Ager III, E. E. Haller, H. Lu, W. J. Schaff, Y. Saito, and Y. Nanishi, *Applied Physics Letters* **80**, 3967 (2002).

[135] R. Dingle, D. D. Sell, S. E. Stokowski, and M. Ilegems, *Physical Review B* **4**, 4 (1971).

[136] L. Chen, B. J. Skromme, R. F. Dalmau, R. Schlesser, Z. Sitar, C. Chen, W. Sun, J. Yang, M. A. Khan, M. L. Nakarmi, J. Y. Lin, and H.-X. Jiang, *Applied Physics Letters* **85**, 4334 (2004).

[137] S. Kako, C. Santori, K. Hoshino, S. Gotzinger, Y. Yamamoto, and Y. Arakawa, *Nature Materials* **5**, 887 (2006).

[138] H. Schomig, S. Halm, A. Forchel, G. Bacher, J. Off, and F. Scholz, *Physical Review Letters* **92**, 106802 (2004).

[139] A. F. Jarjour, R. A. Oliver, A. Tahraoui, M. J. Kappers, C. J. Humphreys, and R. A. Taylor, *Physical Review Letters* **99**, 197403 (2007).

[140] R. Bardoux, T. Guillet, P. Lefebvre, T. Taliercio, T. Bretagnon, S. Rousset, B. Gil, and F. Semond, *Physical Review B* **74**, 195319 (2006).

[141] S. Kiravittaya, H. Heidemeyer, and O. G. Schmidt, *Physica E* **23**, 253 (2004).

[142] S. Kiravittaya, A. Rastelli, and O. G. Schmidt, *Applied Physics Letters* **88**, 043112 (2006).

[143] O. G. Schmidt, *Lateral Alignement of Epitaxial Quantum Dots* (Springer Verlag, Berlin, 2007).

[144] E. Fick, *Einführung in die Grundlagen der Quantentheorie* (AULA-Verlag, Wiesbaden, 1988), 6th edition.

Index

Acknowledgements

First of all, I would like to thank Prof. Dieter Bimberg for the opportunity to work in his group and on this exciting subject as well as for his steady support of my research.

I am grateful to Dr. Axel Hoffmann for numerous stimulating discussions and tips throughout the last years and for the willingness to always lend me an ear and sacrifice some of his time, no matter how many papers, reports, letters, and other important things were waiting on his desk. I would also like to thank him for preparing the second expert opinion on my thesis.

Dr. Sven Rodt I thank for the years of guidance and discussions about our common research first as Diploma student and advising PhD candidate and later as PhD candidate and advising post-doc and for the permission of asking questions for the hundredth time. Furthermore, his support concerning all kinds of computer problems is gratefully acknowledged. Max Feucker I would like to thank for his enthusiasm throughout his time as a diploma student and for the contributions he has made for my work.

Special thanks goes to the masters of QD modelling Dr. Andrei Schliwa and Momme Winkelnkemper for countless hours of discussing my experimental and their modelling results and what they actually had to do with each other. They both were my never ending source for all kinds of answers concerning theory and modelling. I always found working on our common papers and discussing a paragraph for the tenth time both, enjoyable and instructive.

I thank Dr. Udo Pohl for his expertise on growth and TEM questions and many valuable ideas. Konstantin Pötschke I gratefully acknowledge for preparing the samples and Anatol Lochmann for processing the shadow masks and the mesas.

Prof. Herbert Kunert and Prof. Udo Scherz are gratefully acknowledged for help with the group theoretical concepts relevant for this work.

Andreas, Elli, Erik, Momme, Paul, and Till I thank for discussions, both on and off subject, for countless coffees and teas, and the ability to always find something to laugh about.

I thank all the (former and current) members of the Bimberg group I had the pleasure working with for the collegiate and enjoyable atmosphere.

I thank Ariane, my parents, and my friends outside of the university for their support and the possibility to empty my head of thoughts about QDs and cathodoluminecence whenever necessary.